Thermophoresis and Cooperative Binding of Nucleotides

Mario Herzog

München 2012

Thermophoresis and Cooperative Binding of Nucleotides

Mario Herzog

Dissertation
an der Physik
der Ludwig–Maximilians–Universität
München

vorgelegt von
Mario Herzog
aus Starnberg

München, den 4. September 2012

Erstgutachter: Prof. Dieter Braun
Zweitgutachter: Prof. Tim Liedl
Tag der mündlichen Prüfung: 19. Oktober 2012

Contents

List of Figures

List of Tables

Zusammenfassung

Thermophorese beschreibt die von Temperaturegradienten angetriebene, gerichtete Bewegung von Partikeln. Obwohl dieser Effekt seit 1856 bekannt ist, werden die zugrundeliegenden Prinzipien immer noch aktiv diskutiert. Im ersten Teil dieser Arbeit wurde ein lange vorhergesagter größenabhängiger Übergang der Thermophorese zum ersten Mal experimentell verifiziert. Die Experimente untersuchen ein sphärisches Kondensator Modell für Thermophorese. Um Vorhersagen über ionisches Abschirmen geladener Partikel zu testen, sind Nanopartikel erforderlich, deren Größe im Bereich der Debye Länge liegt: DNA und RNA Oligonucleotide. Der theoretisch prognostizierte Übergang vom Plattenkondensator- über das sphärische Kondensator- bis hin zum isolierte Sphäre-Modell wurde über einen weiten Bereich von Verhältnissen zwischen Partikelgröße und Debye Länge erfolgreich beobachtet. Die Kombination dieser ionischen Thermophorese mit einer etablierten Beschreibung der Temperaturabhängigkeit von Thermophorese von ungeladenen Partikeln reicht aus, um Thermophorese von einzel- und doppelsträngiger DNA und RNA von 5 °C bis 75 °C und unter Salzkonzentrationen von 0.5mM bis 500mM abzudecken. Dies umfasst einen Großteil biologisch relevanten Bedingungen. Damit lassen sich nicht triviale Abhängigkeiten der Thermophorese in sehr breiten Bereichen von Salzkonzentration und Temperaturen für hoch relevante DNA und RNA Längen mit dem bestätigten Modell vorausberechnen. Diese Experimente geben neue Impulse in der Diskussion über die Rolle von sekundären elektrischen Feldern bei der Thermophorese. Zudem kann dieses neu gewonnene theoretische Verständnis die Quantifizierung von Biomolekülaffinitäten verbessern.

Kooperatives Binden, das im zweiten Teil untersucht wird, ist entscheidend für das Verständnis vieler intrazellulärer Prozesse wie z.B. der Transkription. Mithilfe von Thermophoresemessungen wird das komplette Bindungsverhalten von mehr als zwei Partnern inklusive der kooperativen Effekte untersucht, die komplexe Molekül-Interaktionen formen. Die hier präsentierte, neu entwickelte Prozedur ist sehr flexibel und setzt nur einen fluoreszierzmarkierten Bindungspartner voraus. Im Gegensatz zu Methoden, die auf der Sättigung einer Bindung bei gleichzeitiger Untersuchung einer anderen beruhen, macht dieser neue Ansatz viele zusätzliche kooperative Molekülsysteme zugänglich. Kooperatives Binden eines sternförmigen, dreiteiligen DNA-Komplexes wird mit einer einzigen Messung aufgedeckt. Bindungskonstanten und thermophoretische Eigenschaften der Komplexe werde mit Messungen von Titrationsreihen innerhalb des Konzentrationswürfels untersucht. Diese Methode kann zu einer bisher fehlenden, flexiblen Messtechnik für kooperative Effekte bei geringer Veränderungen der untersuchten Systeme werden.

Abstract

Thermophoresis describes the directed motion of particles induced by a temperature gradient. Although the effect is known since 1856, the fundamental principles giving rise to it are still under active debate. In the first part of this thesis, a long predicted size dependent transition in thermophoresis is experimentally verified for the first time. Experiments probe a spherical capacity model of thermophoresis. To test predictions modelled on ionic shielding of charged particles, nano-scale particles are required that are comparable to the Debye length in size. DNA and RNA oligonucleotides fulfil this requirement and are thus used. The theoretically predicted transition from a planar, over a spherical capacitor towards an isolated sphere model was successfully observed in measurements covering a wide range of particle size to Debye length ratios. Combining the ionic thermophoresis contribution with an established description of the temperature dependence of thermophoresis for uncharged particles is sufficient to account for the thermophoresis of single and double-stranded DNA and RNA samples from 5 °C up to 75 °C and salt strengths from 0.5mM up to 500mM. This covers a broad range of biologically relevant conditions. As a result, non-trivial dependencies of thermophoresis for a very large range of salt concentrations and temperatures for critical DNA and RNA lengths can be predicted with the confirmed model. The experiments give new impulses to the discussion regarding the role of secondary electrical fields in thermophoresis. These results allow for a better quantitative understanding of thermophoresis on a microscopic level. Moreover, this added theoretical understanding is further optimizing the quantification of biomolecule affinity.

Cooperative binding, investigated in the second part, is crucial to the understanding of many cellular processes, e.g. transcription. Thermophoretic measurements are used to probe the complete binding behaviour of more than two partners and derive the strengths of the cooperative effects defining the complex molecule interactions. The newly developed procedure, which is presented here, is very flexible and only requires one fluorescently labeled binding partner. In contrast to other methods, this novel approach does not rely on the possibility to saturate one of the interactions, while being free to probe another, and thus gives access to a much wider range of cooperative molecule systems. The cooperative binding of a star-shaped three-molecule DNA-complex is revealed in a single measurement. Binding constants and thermophoretic properties of bound complexes are reconciled with measurements along titration series throughout the concentration cube. This measurement has the potential to fill the need for a flexible tool to quantify cooperative effects with only minute alterations of the investigated system.

Chapter 1

Thermophoresis

1.1 Introduction

Particles in a temperature gradient tend to settle into a steady state distribution that is not spatially homogeneous and thus not consistent with classical diffusion. The remarkable fact is the persistence with which this phenomenon called thermophoresis resists a conclusive, predictive description.

A lot of different systems exhibit behaviour consistent with the phenomenon of thermophoresis. Obviously many factors have to be considered to compose a comprehensive description [14, 23, 26, 58]. For colloids in aqueous solutions, the size, charge, heat conductivity, several surface properties and more have been implicated to influence thermophoresis and research is ongoing [12, 23, 29, 52, 55, 74, 64]. During my PhD project I investigated the influence of particle charge on thermophoresis by measuring oligonucleotides (here short DNA and RNA strands) in buffer solutions with a number of different salt concentrations. Ions in a solution rearrange and change the distance of influence of a charged colloid. Jan K.G. Dhont has proposed that the interaction between the shielding ion distribution around a charged colloid can be modelled as a spherical capacitor with a distance between the two spheres corresponding to the Debye length λ_{DH}, given by the ion concentration [13]. Furthermore he surmised that the temperature dependence of the energy stored in the spherical capacitor is responsible for the ionic part of thermophoresis.

DNA and RNA samples were used in this context because they are strongly charged and easily modified in base repeats. The behaviour of these biomolecules in physiological solutions is of value to a number of analytical applications in the field of life sciences, such as measurement of the binding affinity of proteins [72], including the relevant cases of antibody binding in serum [38], sensing with GPCR receptors [67] [10], aptamer binding [4] and small-molecule binding for pharmaceutical applications [72] [62] [48].

Moreover, the understanding of thermophoresis is also essential for molecular evolution where thermophoresis is envisaged to accumulate biomolecules in thermal traps [3, 7, 69]. Together with the thermal cycling provided by the convection in vertically elongated cham-

bers, accumulation and replication can be combined [45], possibly implementing Darwinian evolution by thermal gradients.

1.2 Theory

1.2.1 Fundamentals

Thermophoresis was first described by Ludwig in 1856 [39]. He noticed that the salinity at different points in a volume of water was changed if a temperature gradient was applied to it.

Thermophoresis induces a directed particle motion, which suggests a linear response between the temperature gradient and the particle drift velocity.

$$v = -D_T \nabla T$$

The resulting thermophoretic flux $j_{TP} = c \cdot v = -c \cdot D_T \cdot \nabla T$ is counteracted by the diffusive flux $j_D = -D\nabla c$. Here D is the diffusion coefficient and D_T is the thermal diffusion coefficient. In steady-state the two fluxes balance each other:

$$j = j_{TP} + j_{TP} = -cD_T \nabla T - D\nabla c = 0$$

which can be rewritten as

$$\frac{\nabla c}{c} = -\frac{D_T}{D} \cdot \nabla T$$

Integrating both sides leads to:

$$\frac{c}{c_0} = exp(-S_T \Delta T)$$

S_T is called the Soret coefficient [57] and given by $\frac{D_T}{D}$. It determines the ratio between the concentration of particles locally separated with a temperature difference of ΔT. Alternatively $\frac{D_T}{D}$ can be interpreted as the change of steady-state concentration at any given location if the temperature is changed by ΔT.

S_T is thus a steady-state property. If the particles are not too strongly depleted, such that thermodynamic fluctuations are not sufficient for diffusion into the depletion zone, the argument can be made for local thermodynamic equilibrium [12, 13, 16, 15]. By comparing the thermophoretic depletion in steady state $\frac{c}{c_0} = exp(-S_T \Delta T)$ with a Boltzmann distribution [13, 16], the Soret coefficient is given as:

$$S_T = \frac{1}{k_B T} \cdot \frac{dW}{dT}.$$

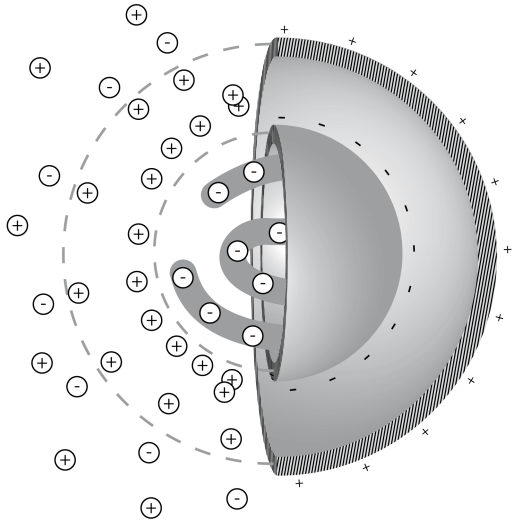

Figure 1.1: A spherical capacitor model of the ionic shielding of charged particles in solutions is investigated as parametrisation for the ionic part to thermophoresis.

1.2.2 Size transition in thermophoresis of charged colloids

In the paper "Thermodiffusion of Charged Colloids: Single-Particle Diffusion" by Jan K. G. Dhont, S. Wiegand, S. Duhr, and D. Braun [13] a theoretical modelling of the interaction between charged colloids and the ions in the solvent was proposed for the ionic part of thermoporesis. The shielding of the charged colloid by the accumulation of ions around it was shown to have the same properties as a spherical capacitor. The temperature dependence of the energy stored in the capacitor then would give raise to thermophoretic behaviour. One of the predictions of this model is a transition between two domains of different thermophoretic behaviour as salt concentration is changed. This prediction was tested using DNA and RNA samples in a wide range salt concentrations.

The Debye length plays a central role in this theory. It is defined as:

$$\lambda_{DH} = \sqrt{\frac{\epsilon_r \epsilon_0 k_B T}{N_A \cdot e^2 \cdot \sum_i c_i \cdot z_i^2}}$$

Here N_A denotes the Avogadro constant, e the elementary charge, c_i the concentration and z_i the changes of the i-th ion type, k_B the Boltzmann constant, T the temperature in Kelvin, ϵ_r the relative permittivity of the solvent, ϵ_0 the vacuum permittivity.

As response to a charged particle, the charge carrying components in the vicinity will rearrange and be attracted or repelled by it. There will be an accumulation of ions of

opposite sign crowded around the particle. With growing distance from the particle the apparent charge of the colloid is increasingly reduced by the influence of the surrounding ion cloud. The colloid charge is shielded by the ions. Because of this, a Coulomb field of a charged particle immersed in an electrolyte solution does not exhibit the $\frac{1}{r}$ falloff expected without mobile charges present in the solution. Rather, the potential shows a decay proportional to $\frac{1}{r} \cdot exp\left(-\frac{r}{\lambda_{DH}}\right)$. The distance over which the charge is shielded depends strongly on the ease with which ions can be recruited. A higher salt concentration means that more ions are in the vicinity of the colloid and the colloid charge is shielded over a shorter distance.

The Soret coefficient S_T can be described as a thermodynamic effect [16].

$$S_T = \frac{1}{k_B T} \frac{dW}{dT}$$

This accounts for the complete thermophoretic effect. At first the focus will be on the ionic part S_T^{ionic} and the corresponding work. The work involved in arranging the shielding ions sphere around the colloid is analogous to that of charging a spherical capacitor with the inner sphere of the size of the colloid and the outer sphere bigger by the shielding distance λ_{DH}. The capacity of a spherical capacitor with inner radius R and distance between spheres λ_{DH} is

$$C = \frac{4\pi\epsilon_r\epsilon_0}{\frac{1}{R} - \frac{1}{R+\lambda_{DH}}}.$$

The work necessary to charge a capacitor is

$$W_{cap} = \frac{Q^2}{2 \cdot C}.$$

With this the ionic contribution to thermophoresis can be written as:

$$S_T^{ionic} = \frac{1}{k_B T} \frac{dW_{cap}}{dT} = \tag{1.1}$$

$$\frac{1}{T} + \frac{Q^2}{16\pi k_B T^2 \epsilon_r \epsilon_0 \lambda_{DH}} \cdot \frac{1}{\left(1 + \frac{R}{\lambda_{DH}}\right)^2} \cdot \left(1 - \frac{\partial ln\rho(T)}{\partial lnT} - \frac{\partial ln\epsilon_r(T)}{\partial lnT} \cdot \left(1 + 2 \cdot \frac{\lambda_{DH}}{R}\right)\right)$$

The density ρ and the relative permittivity ϵ_r of water including their temperature dependence are well known [46, 37]. The expansion of water with increasing temperature represented by ρ changes the concentration of the ions and thus has to be considered for its effect on λ_{DH}. As discussed, the Debye length can be controlled by changing the salinity of the buffer. The only parameters of S_T^{ionic} not known are the radius of the inner sphere and the charge the capacitor is holding.

Prior to this work, this model has only been tested using particles larger than the Debye length λ_{DH} [13, 16, 54]. S_T^{ionic} predicts that thermophoresis under conditions where $R \gg \lambda_{DH}$ should scale differently with changing salt concentration than when $R \ll \lambda_{DH}$.

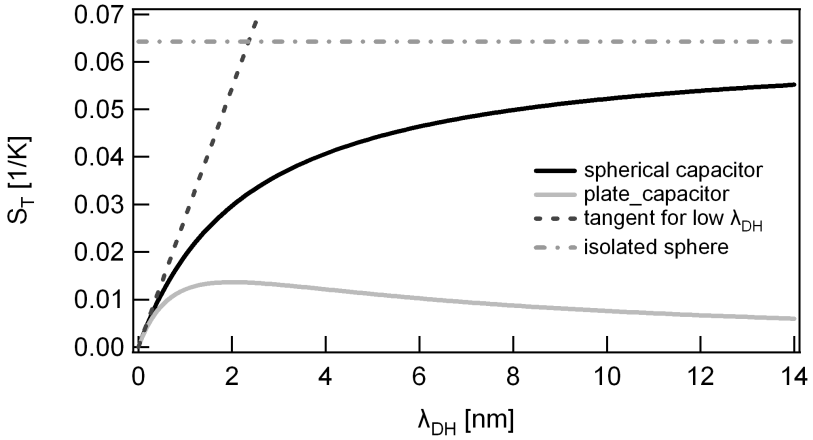

Figure 1.2: Plot of S_T versus λ_{DH} of S_T^{ionic} and its two tangents for $R \gg \lambda_{DH}$ (step line through the origin) and $R \ll \lambda_{DH}$ (constant value of 0.064 $1/K$). These are expected for the limits at which the spherical capacitor behaves like a plate capacitor (green plot) and an isolated sphere respectively. The plotted values are based on a particle with $8.8e^-$ charges and a radius of 2nm.

The behaviour of both limiting cases can be investigated a little bit further. For very low Debye lengths the capacitor behaves like a parallel plane capacitor and the Soret coefficient increases linearly with the Debye λ_{DH} [16] according to:

$$\lim_{\lambda_{DH}\to 0} S_T = \frac{1}{T} + \frac{Q^2}{16 \cdot \pi \cdot k_B \cdot T^2 \cdot \epsilon_r \cdot \epsilon_0 \cdot R^2} \cdot \left(1 - \frac{\partial ln\rho(T)}{\partial lnT} - \frac{\partial ln\epsilon_r(T)}{\partial lnT}\right) \cdot \lambda_{DH}$$

In the limit where λ_{DH} increases far beyond the radius of the colloid, we obtain an isolated charged sphere and find a constant Soret coefficient given as:

$$\lim_{\lambda_{DH}\to \infty} S_T = \frac{1}{T} + \frac{Q^2}{16 \cdot \pi \cdot k_B \cdot T^2 \cdot \epsilon_r \cdot \epsilon_0 \cdot R} \cdot \frac{-2 \cdot \partial ln\epsilon_r(T)}{\partial lnT}$$

These two extreme cases (see figure 1.2) showing the behaviour for infinite and vanishing charge shielding intersect at $\lambda_{DH}^{intersect}$, which scales linearly with the size of the particle radius. The size transition is expected to shift to higher λ_{DH} for larger particles. Ignoring thermal expansion of water for the moment, this leads to:

$$\lambda_{DH}^{intersect} = 2 \cdot \frac{\partial ln\epsilon_r(T)/\partial lnT}{(\partial ln\epsilon_r(T)/\partial lnT) - 1} \cdot R$$

As a side note it might be of interest that the spherical capacitor model [13] does not discern between otherwise identical systems with particles with electrical charges of opposite sign. This is a clear difference to electrophoresis.

The charge will certainly not be the colloid's only property relevant for thermophoresis, so additional contributions—called non-ionic in this work—have to be considered:

$$S_T = S_T^{ionic} + S_T^{NI} = \tag{1.2}$$

$$= \frac{1}{T} + \frac{Q^2}{16 \cdot \pi \cdot k_B \cdot T^2 \cdot \epsilon_r \cdot \epsilon_0 \cdot \lambda_{DH}} \cdot \frac{1}{\left(1 + \frac{R}{\lambda_{DH}}\right)^2} \cdot$$

$$\cdot \left(1 - \frac{\partial ln\rho(T)}{\partial lnT} - \frac{\partial ln\epsilon_r(T)}{\partial lnT} \cdot \left(1 + 2 \cdot \frac{\lambda_{DH}}{R}\right)\right) + S_T^{NI}$$

While empirical in nature, there is a description of the temperature dependence of thermodiffusion that agrees with the thermophoresis in a number of tested systems [30, 52, 68]. Piazza showed [28] that the thermophoresis he found for his measurement systems followed the temperature dependence expressed by:

$$S_T^{Piazza} = S_T^{\infty} \cdot \left[1 - exp\left(\frac{T^* - T}{T_0}\right)\right]$$

S_T^{∞} is the limit reached for arbitrarily high temperatures, T^* the temperature at which S_T^{NI} changes sign and T_0 determines how fast S_T^{∞} is approached with growing temperature. In evaluating the thermophoretic data of oligonucleotides we compared the thermophoresis extrapolated from S_T^{ionic} for perfectly shielded particles and found that it agreed very well with S_T^{Piazza}. This resulted from a fit of S_T^{ionic} to the measured S_T values for different salt concentrations independently for different temperatures with S_T^{NI} as a free fitting parameter. Which means that the evaluation procedure had no bias to show the behaviour.

While the ionic contribution S_T^{ionic} decreases in strength for increasing temperature, S_T^{Piazza} increases monotonously with increasing temperature approaching the upper bound S_T^{∞}. This predicts a non-trivial temperature dependence of the combined S_T. For charged particles of a couple of nano-meters in size at moderate ionic shielding and Piazza parameters S_T^{∞}, T^* and T_0 motivated by earlier measurements [28], we expect increasing S_T values along the temperature axis for low temperatures but decreasing S_T values for higher temperatures. As we will show, this is one more characteristic of the model that is evident for the measurements of short DNA and RNA (see figure 1.20).

The above results prompted us to use S_T^{Piazza} as S_T^{NI} in a more comprehensive analysis that covered the measurements for all measured temperatures and salt concentrations.

While this does not mean that our parametrisation of S_T^{ionic} and S_T^{Piazza} are the only contributions to the thermophoresis of nucleotides in aqueous solutions, for the samples used for this work and within its experimental parameters the combination of the two was sufficient to account for all measured properties.

1.3 Materials and Methods

1.3.1 Measurement setup

All thermophoresis measurements were done with a standard fluorescence microscope modified to add the ability to heat the sample region imaged by the microscope using an infrared laser (see figure 1.3) [54]. The complete setup was placed on a passively suspended optical table to reduce vibrations. A curtain of opaque, black fabric surrounding the complete setup during measurements kept stray light from adding to the signal background. At its core, the upright fluorescence microscope is a type Scope A1 by Zeiss. Detection can be switched between a photomultiplier and a CCD camera. Though a photomultiplier is more sensitive and has a much lower noise level, spatial information is not present, which is indispensable when investigating the complicated interplay between diffusion and thermodiffusion in the presence of bleaching and temperature dependence of the fluorescence dye.

All measurements were done using an air objective by Partec with a magnification of $40\times$ at a NA of 0.80.

An Andor Luca DL-658M-TIL was used for imaging. This electron multiplying CCD camera has 658×496 pixels at $10\mu m \times 10\mu m$ per pixel. The final resolution was determined to be $1.13\mu m/pixel$. For the time sensitive temperature measurements 2×2 binned images where recorded at a frame rate of 20 Hz. Additionally a $0.5\times$ adapter lens widened the field of view to cover a bigger part of the temperature increase distribution. This improved the results of the temperature evaluation.

The frames of the fluorescence signal were saved as 16bit grey-scale .tiff files. These are capable of storing the complete 14bit information provided by the monochrome CCD.

For the nucleotide measurements the frame rate was reduced to 5 Hz and 8×8 pixels were binned in camera to reduce the contribution of read-out noise at the cost of spatial resolution that is, however, not needed in this application. To account for the noise background of the camera signal, a dark count is subtracted from the count values.

To illuminate the samples high-powered LEDs where used. A green LED for HEX labeled samples and a cyan LED for BCECF measurements were used. Both were produced by Luxeon (Calgary, Canada). They were individually mounted in standard halogen lamp housings. The LEDs were driven by a Thorlabs LDC210C constant current source via a BNC connector For HEX and BCECF measurements standard filter sets were used (AHF-Analysentechnik, F36-542 and F11-001).

The laser (Fibotec, λ=1480nm, typical emission power 28 mW) was controlled with a 0 - 5V analogue output of a NI-6229DAQmx measurement automation card (National Instruments, Austin, Texas). Laser power was adjusted until the achieved temperature increase matched experimental requirements. If the laser spot size needs to be altered, the collimator on the side of the optical cube can be replaced.

The laser beam is coupled into the microscope's optical axis (see figure 1.6 and for overview figure 1.3) with optics transparent to the excitation and emission wavelengths.

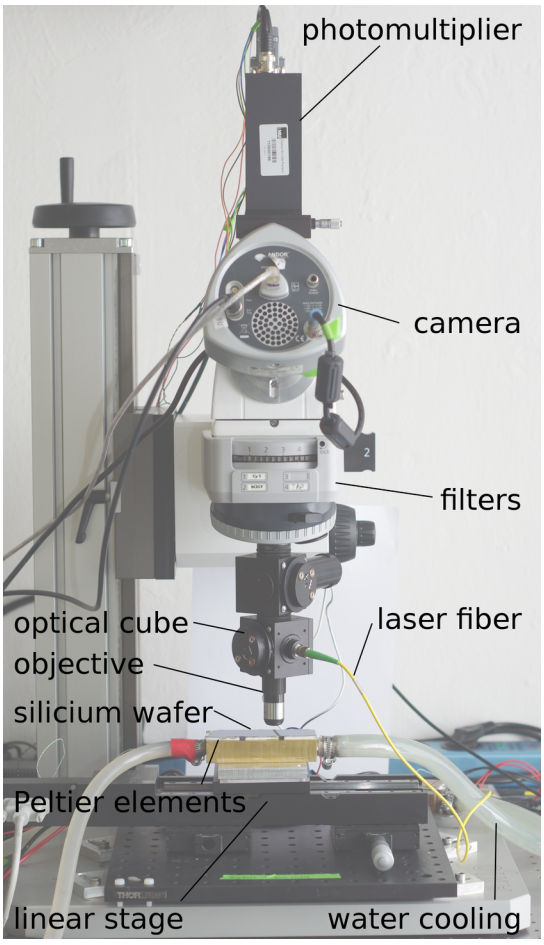

Figure 1.3: Schematic view of the experimental setup. In the first chapter of this work a camera was used, while in the second a photomultiplier recorded the fluorescence signal of the samples. These were lined up on the silicium waver. The waver could be be heated and cooled with Peltier elements. The infra-red fiber laser was coupled into the optical beam (see figure 1.6) and created temperature gradients in the capillaries through the same objective as the fluorescence detection.

No infra-red blocking filter was used to increase the signals by keeping the number of interfaces they had to pass through low.

Instead of screwing the objective directly into the so-called *nosepiece* (a rotating table used to switch between several objectives), an optical cube by Thorlabs was places between the two (see figure 1.3). A dichroic mirror (NT46-386, Edmund Optics, Barrington, USA) in the cube reflected the beam from the laser fiber fastened to the collimator (ThorLabs, F220FC-C) screwed into the side of the cube into the optical path of the microscope. The dichroic mirror was mounted on a platform that allows tilting the mirror using three screws. This way the laser beam could be adjusted to hit the sample in the area being imaged. Since the laser and the fluorescence emission were both collimated above the objective, focussing the sample optically with a infinity-corrected objective also meant focussing the laser spot. The different wavelengths resulted in slightly different focal planes for the fluorescence and the laser due to achromatic aberration, but the resulting defocussing of the laser spot was minute and very reproducible. The exact laser beam properties were secondary to the temperature distribution information in this context.

Combining an air immersion objective with moderate depletion values not exceeding 50% ensures that temperature as well as concentration profiles are linearly averaged over the height of the measurement chamber.

Sample solutions were measured in borosilicate capillaries with a rectangular inner cross-section of $50\mu m \times 500\mu m$ and a length of $50mm$ (produced by Vitrotubes, Vitrocom, Mountain Lakes, USA). At $1.25\mu l$, they use very little sample per capillary. Although the capillary wall is uniformly $50\mu m$ thick, breakage is rather low if handled carefully. For long measurements covering temperatures up to 75 °C, it is necessary to seal the capillaries with wax (Tight Sealing Wax, NanoTemper, Munich, Germany). Otherwise evaporation will increase the concentration of the non-volatile components of the solution until no liquid remains in the imaged region of the capillary.

For each measurement, a number of capillaries were placed next to each other on a rectangular piece of silicon waver with a thickness of $525\mu m$.

The base temperature of the sample capillaries could be controlled with a Peltier element (max $\Delta T = 68\,°C$, Telemeter Electronic GmbH, PC-128-10-05) right below the silicon waver. The current of the EA-PS 3032-10B power supply (Elektro Automatik GmbH, Viersen, Germany) was controlled by a NI-6229DAQmx measurement automation card (National Instruments, Austin, Texas). The lower side of the Peltier element was connected to a copper block that temperated water was pumped through. An Ecoline RE207 (Lauda Dr. R Wobser GmbH, Germany) water bath was used. Low pumping speeds kept vibrations at a minimum.

The copper block resided on an automatic single axis translation stage by Misumi Translation used to automatically switch between sample capillaries. It provided high positioning accuracy of 20 μm and positioning repeatability of 3 μm.

All these components and the software that controlled them where assembled and thoroughly tested by Christoph Wienken.

1.3.2 Samples

The measurements in this work were conducted with short DNA and RNA oligonucleotides. For each, DNA and RNA, polymeres of 5, 10, 22 and 50 bases in length were synthesised (Biomers, Ulm, Germany). The samples were labeled with the fluorescent dye HEX (6-carboxy-2',4,4',5',7,7'-hexachlorofluorescein) as a 5' modification. The oligonucleotides were purified with a HPLC column. Free fluorophores are thus not compromising our measurements. Aliquots of $11\mu l$ were taken at a concentration of $100\mu M$. The stock solution was kept frozen at $-20\,^{\circ}\mathrm{C}$ and only defrosted when new aliquots were needed. For single stranded DNA of length 5, 10, 22 and 50 bases the particle size was measured to be 1.5 ± 0.9, 1.7 ± 0.4, 2.1 ± 0.6 and $4.6 \pm 0.8nm$ (s.d.), respectively. In addition to the labeled samples, unlabeled complements to the 22 and 50 bases DNA samples and 22 bases RNA samples were used. With these, the measurement could be extended to cover double stranded oligonucleotides.

The oligonucleotides were covalently labeled with a fluorescent dye. Accordingly, the thermophoresis of these might diverge from oligonucleotides without the dye. To use absorption to measure concentration would need much longer light paths through the chamber (Beer-Labert law) and would not be compatible with the low convection chambers used here. Including the auto-fluorescent 2-aminopurine—an analog of guanine and adenine—in the synthesised oligonucleotides would be an option, but the quantum efficiency is lower than for the dye employed here.

Therefore the measurement of fluorescently labeled oligonucleotides presents itself as the best available approach.

Oligonucleotide samples were prepared to total volumes of $50\mu l$. This kept the smallest parts to add at a manageable 0.5μl. The Debye length λ_{DH} was moderated by altering the ionic strength of the buffer solution with KCl. Buffering was accomplished with Tris adjusted to pH 7.8 at room temperature and a concentration of 100mM. Tris has a temperature dependent pH value as described earlier (page 12). It helps keeping the pH of the solution contained above the highest pKa value for DNA or RNA below the neutral range of about pKa 4.26 and below the lowest pKa value of 8.74 above it [9]. The charge of the samples is not expected to change across all the measurements.

For temperature measurements the fluorescent dye BCECF (2',7'-bis-(2-carboxyethyl)-5-(and-6)-carboxyfluorescein, Invitrogen B-1151) at a concentration of $50\mu M$ in a 10mM TRIS solution was used.

To determine the temperature from the change in fluorescence, a calibration curve is necessary. To record such a curve, a BCECF sample is placed on a Peltier element under the microscope. The fluorescence values for the temperature range the measurement has to cover are recorded. A temperature probe (PT1000) on the Peltier element next to the measurement chamber (i.e. capillary) holding the BCECF can be used to determine the sample temperature for reference.

The BCECF is thermally coupled to the Peltier element and will have the same temperature throughout the sample. The fluorescence change is therefore homogeneous as well. The measurement can be conducted with a fluorometer, but it is preferable to record the

Sample	Sequence
DNA 5-mer	5'- Hex-TA GTT - 3'
DNA 10-mer	5' - Hex-TA GTT CTA AT - 3'
DNA 22-mer	5' - Hex-AT TGA GAT ACA CAT TAG AAC TA - 3'
DNA 50-mer	5' - Hex-ATA ATC TGT AGT ACT GCA GAA AAC TTG TGG GTT ACT GTT TAC TAT GGG GT - 3'
RNA 5-mer	5' - Hex-UA GUU - 3'
RNA 10-mer	5' - Hex-UA GUU CUA AU - 3'
RNA 22-mer	5' - Hex-AU UGA GAU ACA CAU UAG AAC UA - 3'
RNA 50-mer	5' - Hex-AUA AUC UGU AGU ACU GCA GAA AAC UUG UGG GUU ACU GUU UAC UAU GGG GU - 3'
DNA 22-mer complement	5' - TAG TTC TAA TGT GTA TCT CAA T - 3'
DNA 50-mer complement	5' - ACC CCA TAG TAA ACA GTA ACC CAC AAG TTT TCT GCA GTA CTA CAG ATT AT - 3'
RNA 50-mer complement	5' - AC CCC AUA GUA AAC AGU AAC CCA CAA GUU UUC UGC AGU ACU ACA GAU UAU - 3'

Table 1.1: Sequences of the DNA and RNA samples.

Sample	λ_{DH} [nm]	KCl conc. [mM]	Tris conc. [mM]
A	0.43	500	1
B	0.79	150	1
C	2.1	20	1
D	3.7	6	1
E	5.6	2	1
F	8.2	0.4	1
G	9.7	0	1
H	13.8	0	0.5

Table 1.2: Sample composition. All samples additionally contained 1μM nucleotides.

calibration curve on the same setup used to determine the laser driven temperature distribution. This way the change in fluorescence and the correlating temperature of the sample is known. Having this conversion function at hand, a temperature increase can be deduced from the fluorescence comparison of fluorescence images, as long as the concentration is homogeneous [6].

BCECF is very well suited for use as a temperature probe. The measured signal uses a secondary effect of BECEF changing quantum efficiency for different pH values.The TRIS buffer is known to have a pH decrease of about 2.68% per Kelvin temperature increase if adjusted to have a pH of 7.8 at 25 °C [18, 63].

$$pH(T) = 8.49 - 0.0268 \cdot T[^{\circ}\mathrm{C}]$$

1.4 Measurements

1.4.1 Experimental quantification of of laser induced thermal fields

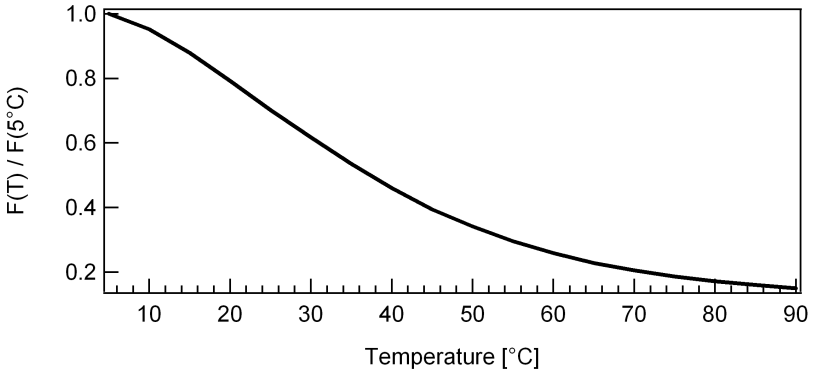

Figure 1.4: Calibration curve used to calculate the temperature increase due to laser heating. Relative fluorescence change $F(T)/F(5\,^{\circ}\mathrm{C})$ of BCECF from 5 to 90 °C. With a curve like this temperature measurements in liquids are possible. Data measured together with Christof Mast

Since it is the temperature gradient that gives rise to thermophoresis, the determination of the temperature distribution is of obvious importance. The aqueous samples are heated in volume by absorption of a laser beam with a diameter of between 20 and 100μm. Therefore the measurement chamber can be much smaller than in other measurement setups, resulting in very low sample consumption of few micro-liters of sample per measurement. Micro-scale geometry also leads to equilibration of the temperature as well as concentration within less than a second and within a couple of minutes respectively. While some measurement setups have a linear temperature gradient between a hot and a cold wall of the measurement chamber [31], determining the temperature distribution in our setup is

not as simple. An infra-red laser is used to optically heat the aqueous sample solution. At wavelength of $1480nm$ it is absorbed by water with an absorption length (penetration depth at which the beam intensity is reduce by a factor of e) of $355\mu m$ [32]. Based on the Lambert-Beer law $I(x)/I(0) = e^{-x/x_{att}}$ [5, 35], where x_{att} is the attenuation length, the deposited energy can be calculated.

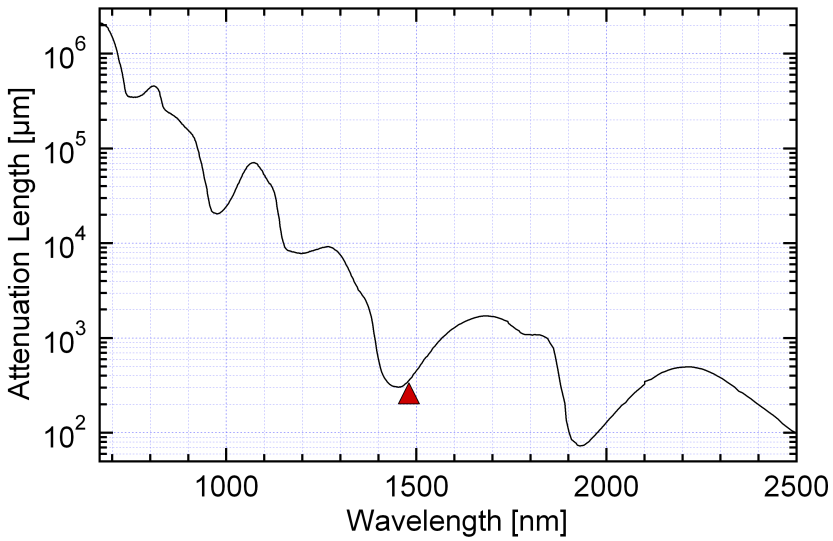

Figure 1.5: Attenuation length x_{att} at which beam intensity is reduced by a factor of e. $I(x)/I(0) = e^{-x/x_{att}}$. The infra-red laser used in this experiment has an attenuation length of $355\mu m$.

Spatially resolved temperature measurements were done by CCD imaging using fluorescent dyes, exhibiting a temperature dependent fluorescence efficiency. As discussed in 1.3.2, to determine the temperature from the change in fluorescence, a calibration was recorded (see figure 1.4). With the knowledge of the temperature dependence of the dye's fluorescence it is possible to calculate the temperature, as long as the change in local fluorescence is exclusively brought about by the change in quantum efficiency.

However the dye concentration is altered due to thermophoresis if the temperature distribution is no longer homogeneous. As a result the change of fluorescence in a given region stems not only from the dye molecules fluorescing less efficiently, but also from the fact that the local dye concentration has changed as a response to the temperature distribution. The separation of timescales at which the different effects equilibrate facilitate the discrimination of the two contributions. After the laser is switched on, the temperature distribution (see figure 1.7) equilibrates within $150ms$ in the standard $50 \times 500\mu m$ capillary (see page 9 in the materials section) used in this work. The fluorescence of the dye reflects the changes in buffer conditions at an even shorter timescale. Thermophoretic depletion of fluorescent dye takes longer than the change of fluorescence efficiency to set in. By waiting $150ms$ after the change of laser intensity, when the temperature distribution has

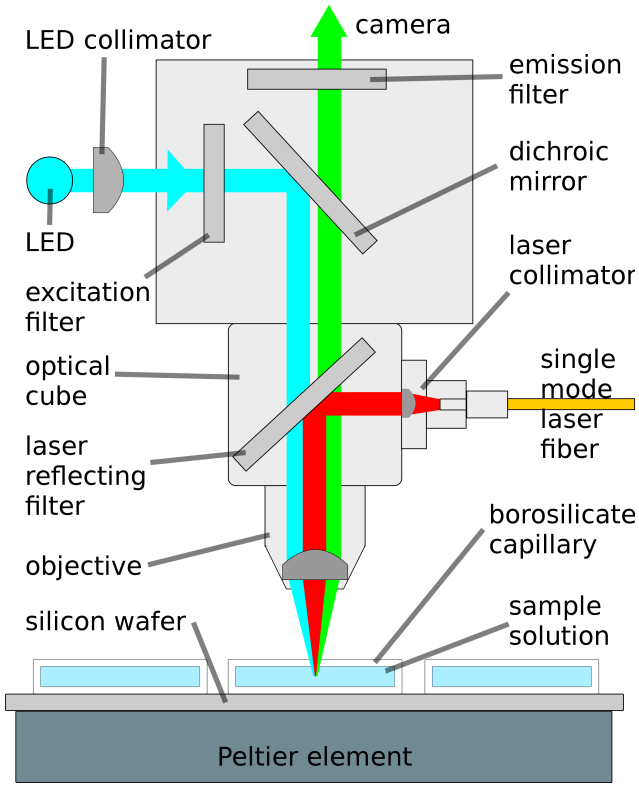

Figure 1.6: Schematic view of the experimental setup. The light from a LED is collimated an then filtered for the excitation band of the fluorophore. A dichroic mirror reflects it into the primary beam path. Focussed by the objective it excites the samples in the solution inside the borosilicate capillary. The fluorescence of the sample is picked up by the objective. Its wavelenght can pass the upper dichroic mirror, is filtered by the emission filter and continues on to the camera or photodetector. In the optical cube above the objective a second dichroic mirror reflects the infra-red laser that creates temperature gradients in the sample solution. The capillaries are placed on a silicon waver. They can be heated or cooled with a Peltier element.

reached its steady state and the thermophoretic depletion has not yet changed the dye distribution, the change in sample brightness actually reflects a property from which the temperature change can be derived using the calibration measurement discussed earlier. The temperature measurements were corrected for photo bleaching. In principle all it takes is the reference signal at a known homogeneous temperature, the signal after the temperature change and control of the time delay between the temperature change and the moment the second signal is acquired. This procedure is referred to as taking a *temperature jump snapshot*. It works very well to derive the temperature distribution in the object plane of the microscope from two frames recorded with a CCD camera (as seen in figure 1.6).

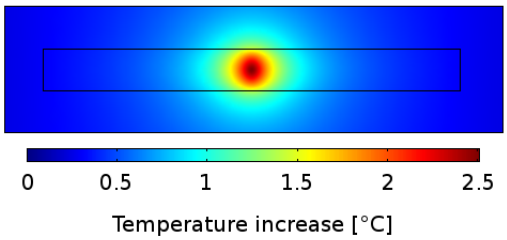

Figure 1.7: Femlab simulation of the temperature increase distribution distribution inside the capillary. The dimensions of the inside of the capillary are $50 \times 500 \mu m$ with a uniform wall strenght of $50 \mu m$.

The observed spatial temperature distributions follow a radially symmetric Lorentz distribution so well that it suggests an underlying principle. An argument could be made that the laser beam with a Gaussian intensity distribution results in a Lorentzian temperature increase shape because of maximisation of entropy [8].

The temperature at any point in the object plane with distance r from the spot center in our sample is sufficiently defined by the sample's base temperature T_{base} measured away from the laser spot, the peak temperature increase ΔT_{max} and the width of the Lorentzian temperature shape w (also described as 'half width at half the maximum amplitude' or short HWHM):

$$T(r) = T_{base} + \Delta T_{max} \cdot \frac{w^2}{r^2 + w^2}.$$

1.4.2 DNA and RNA measurements

While measurements had been compared to the predictions of the spherical capacitor model [13, 16, 54], the particles were always too big to resolve the size transition between the two limits described earlier. Including pipetting errors and camera noise, the errors from the measurement are on average 10%. The standard deviation of the fit is provided given as error bars in figures 1.17 and 1.18 for example.

For every DNA or RNA sample, eight salt concentrations were measured in capillaries next to each other on the sample stage and for all temperatures in one long measurement.

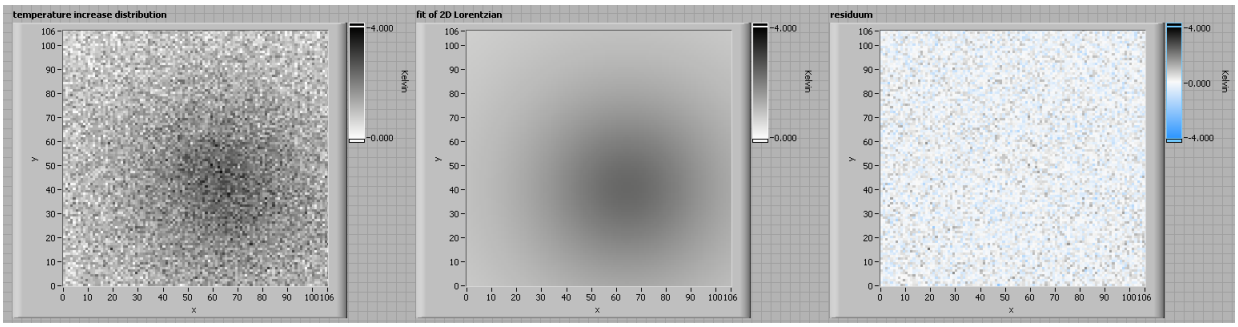

Figure 1.8: Temperature increase distributions in the sample solution are measured with a BCECF snapshot. The fit (center) of the measurement data (left side) describes the temperature distribution well enough that the residuum (right side) appears to be the remaining detection noise. Here x- and y-positions are pixel values. Fit values: $T_{base} = 25.4\,°\mathrm{C}, \Delta T_{max} = 1.9\,°\mathrm{C}$, Lorentzian HWHM $w = 68.8\mu m$

Before the oligonucleotide measurement the temperature distribution of the laser heating was ascertained with BCECF in a capillary from the same batch as used for the DNA or RNA measurements. The setup was used for other measurements during the time these data sets were recorded. One of which needed a UV illumination. Analogously to the infra-red laser an additional optical cube was introduced below the objective holding table. Detaching the laser deflecting cube several times between the measurements made it necessary to record separate temperature distributions for different measurement blocks.

A single thermophoresis measurement was timed as follows: Five seconds after the camera started collecting frames the infra-red laser was switched on. After 180s of collecting fluorescence data in an inhomogeneous temperature distribution, the laser was switched off and another 180s of the samples diffusing back towards the unperturbed concentration distribution was recorded. The depletion and diffusive recovery of the fluorescence signal close to the center of the spot can be seen in figure 1.9

This measurement procedure was repeated for every sample. The linear translation staged would move one sample after the other in front of the objective. When all samples were measured, the temperature was increased. For this experiment we used a linear temperature ramp from 5 °C to 75 °C in increments of 10 °C. After the Peltier control voltage was altered to heat the sample stage to the next temperature, a five minute delay made sure that the samples had equilibrated before the first measurement at the new temperature was started.

After all the oligonucleotide data was collected, another temperature distribution measurement was done. If the focus or the change in fluorescence upon laser activation was not like before the oligonucleotide measurements, the measurement setup must have been disturbed in some way in between. Then it was not possible to tell under which conditions a given thermophoresis measurement was done and the measurement had to be repeated.

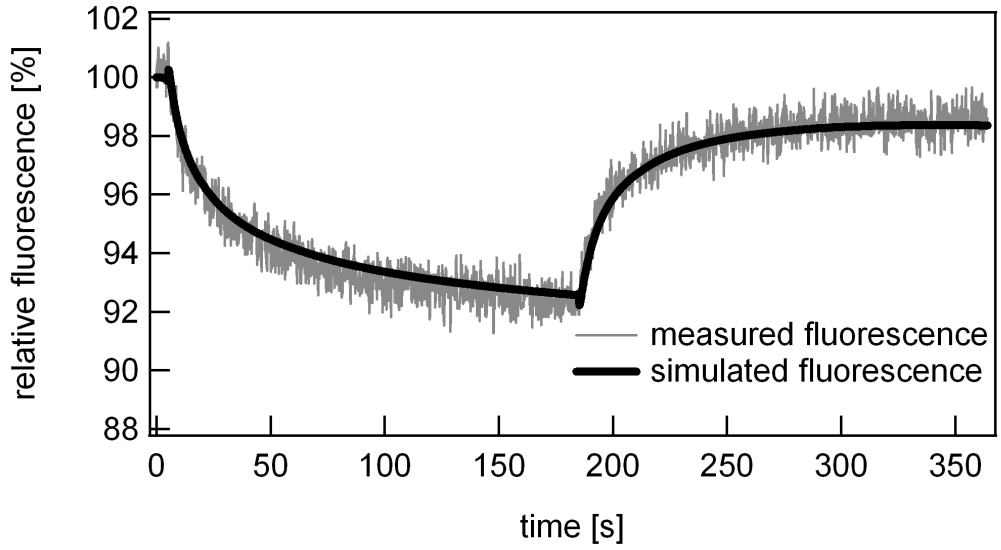

Figure 1.9: Fluorescence change over the course of a standard experiment at the center of depletion. Five seconds after measurement begin the laser is activate and triggers the thermophoretic depletion of the sample molecules. 180 seconds later the laser is turned of to record another three minutes of back-diffusion. The strength of the depletion is determined by the thermophoresis properties of the molecules. The speed with which the thermophoretic steady state depletion is approached and the behaviour after the temperature gradients have ceased indicate the diffusion coefficient of the molecules.

1.5 Data analysis

The series of fluorescence images of the thermophoretic depletion and diffusive signal recovery was interpreted with a NI Labview program (*Binding Evaluator*, screen-shot seen in figure 1.10). The functionality can be summed up as follows: It loads the frame series, assists in setting the depletion center position, extracts a time versus radius map of normalised depletion values and remote-controls FEMlab through a Matlab interface to simulate the thermophoretic depletion so the relevant parameters can be adjusted until agreement between measurement and simulation would be reached. The program has additional functionality, though that is beyond the scope of this work. It was written by Prof. Dieter Braun. Beyond minute modifications by me, the biggest other contribution was the work of Philipp Serr, who improved the Java code so the simulation results would be returned much faster to the LabView interface.

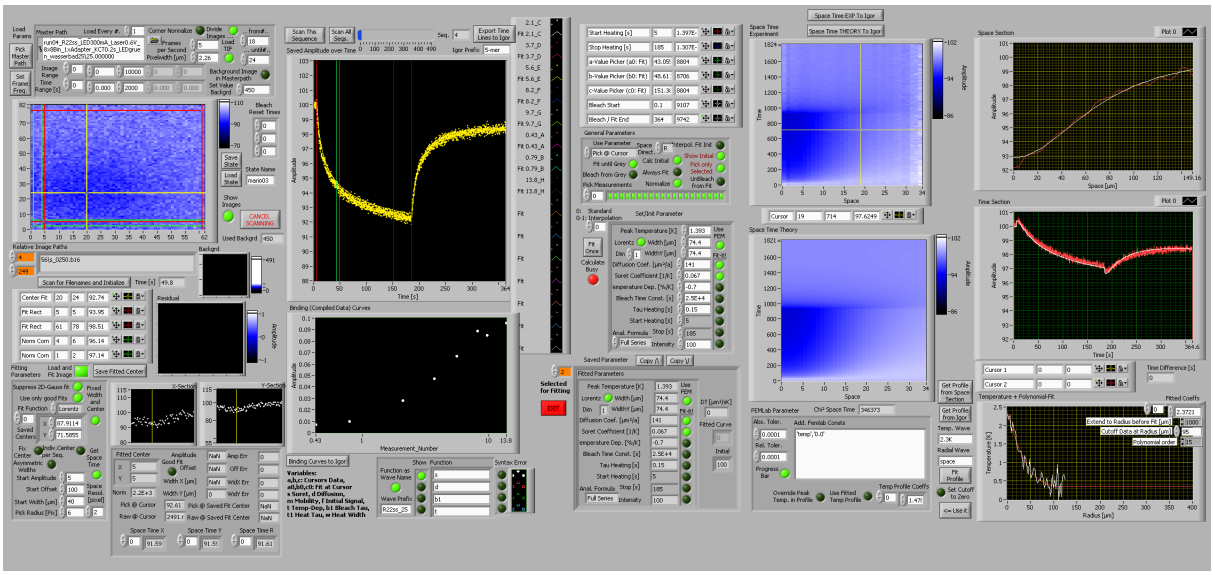

Figure 1.10: Overview of the interface of the LabView program Binding Evaluator used to analyse the series fluorescence images. It loads the frame series, assists in setting the depletion center position, extracts a time versus radius map of normalised depletion values and remote-controls FEMlab through a Matlab interface to simulate the thermophoretic depletion so the relevant parameters can be adjusted until agreement between measurement and simulation would be reached.

In the Labview program a range of frames with unperturbed sample distribution was selected. For analysis all frames were divided by the image averaged from the images in this range on a per pixel level. This discarded the influence of inhomogeneous illumination and reduced the influence of distortions like local imperfections of the sample capillaries. Additionally the camera count background was corrected for by subtracting the dark count of the CCD. The frame rate and the pixel width (assuming symmetrical scaling in x and

y direction) was set to convert frame number and pixel position values in seconds and meters.

Next the center of depletion was determined. From a frame with strong depletion — between 150 and 180 seconds into the measurement in this case — a fit routine helped determine the center of the depletion.

Using these settings the raw data was loaded into the program. The *Binding Evaluator* processes the frames one after the other, normalises them to the homogeneous fluorescence signal and radially averages all counts with equal distance to the center of depletion. A trade-off between radial resolution and noise suppression by averaging is called for when setting the width of the radius bins (6μm was used). The implied radial symmetry would not be guaranteed if the borders of the measurement chamber were too close to the depletion region. For this measurement the capillary wall of the 500μm wide capillary is well outside the main depletion zone fitting well inside the imaged area of 140μm $\times$ 185μm centred in it.

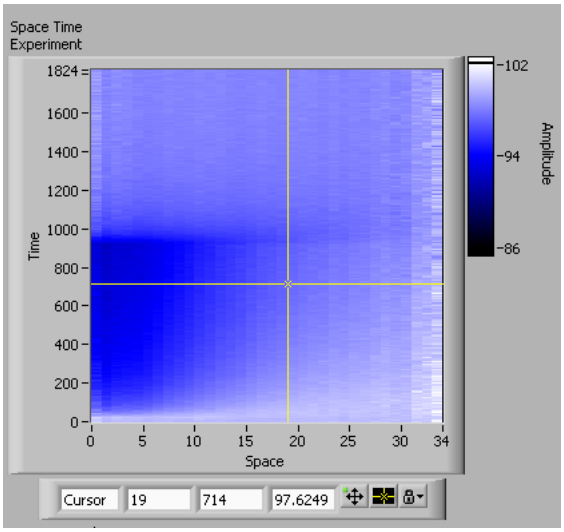

Figure 1.11: Map of the depletion values. The x position gives the distance from the depletion center in 6μm wide bins. The y position is the frame number (frame rate 5Hz). The depletion is given in percent of the unperturbed fluorescence level. Amplitude is given in percent of fluorescence intensity compared to the unperturbed sample condition.

The radial averaging procedure returns a map of depletion values of every frame and radial bin of the measurement. In this map (figure 1.11) the innermost (r=0μm) and outer most bins (here r=$28 \cdot 6\mu m$=168μm) show much more noise. They are calculated from a very small number of pixels.

The moment the laser is turned on and off, the fluorescence changes almost instantly (although not equally strong) for all radii. This change is faster than the thermophoresis response and reaches further than the depletion. The fluorescent dye shows minor temperature dependence. Although it is a small effect, it is independent of the diffusion or the thermodiffusion coefficient and gives feedback about the quality of the temperature

measurement. For a fixed laser power it nevertheless has to be adjusted for different base temperatures. The depletion map contains the complete information about the sample's response to the temperature distribution used to interpret the thermophoretic and diffusive behaviour of the colloids.

To extract the Soret coefficient S_T and the diffusion coefficient D from the raw fluorescence data, a FEMlab simulation is used. Given the low temperature increase ($\Delta T < 2.4K$) and the low height of the measurement chamber, convection is not strong enough to significantly influence the thermophoretic depletion. This was tested with a full 3D FEMlab simulation (figure 1.12), which showed that for $\Delta T = 2.4K$ the convective velocity in the plane of observation was below 0.6μm/s with the peak velocity of below 2.4μm/s and dropping below 1μm/s within 10μm from the beam center. Even for the biggest samples used here, these speeds are easily overcome by diffusion and are not changing the concentration distribution significantly.

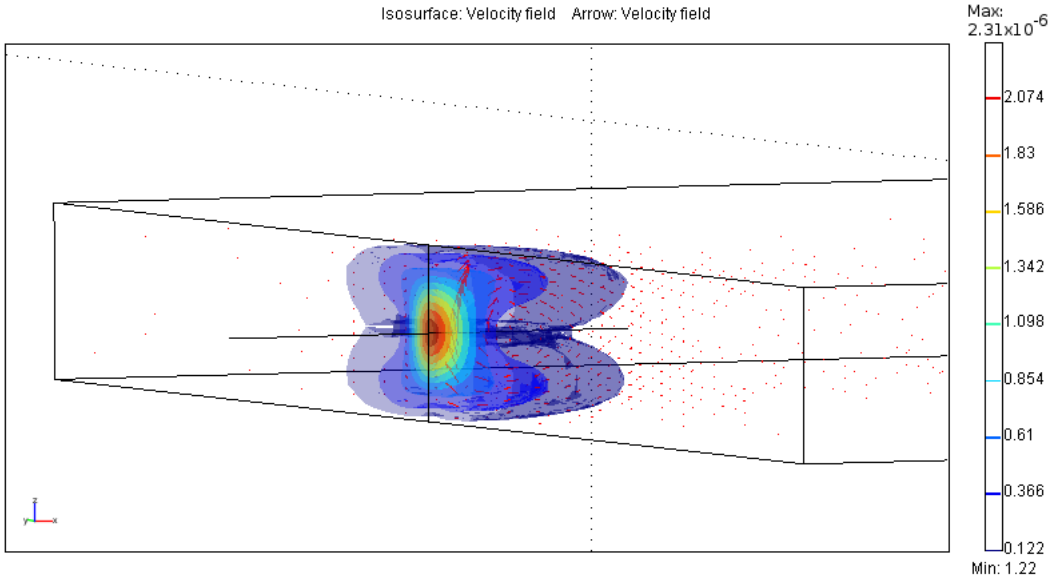

Figure 1.12: A FEMlab simulation of the convection in the capillary shows that the convection pattern is limited to the center of the capillary and loses in strength within a few microns from the beam focus. The velocity components in the observation plane were not strong enough to influence the concentration distribution significantly and were ignored in the analysis.

Therefore a 1D radially symmetrical FEMlab simulation was used. Since many executions of the simulation were needed to find the right set of parameters, the reduced computation time helped the analysis. Thermoporesis was implemented by modifying the diffusive mass current density used by FEMlab to include the thermophoretic mass current density:

$$j = -c \cdot D_T \cdot \frac{dT}{dr} - D \cdot \frac{dc}{dr}$$

In this parametrisation the temperature distribution T is homogeneous and the derivative thus zero when the laser is off and follows a Lorentzian distribution with peak temperature increase ΔT and a HWHM width w when the laser is on. As detailed above (section 1.4.1) the temperature distribution in the capillary was determined using a BCECF temperature jump experiment.

The time evolution of the simulated concentration distribution is displayed in a radius-time-map analogous to figure 1.11. With the temperature distribution given, the diffusion coefficient D and the Soret coefficient $S_T = D_T/D$ can be adjusted until the simulation and the measurement predict the same depletion values.

Additional simulation parameters are the bleaching time constant (on the order of 10^5 s), the temperature dependence of the dyes quantum efficiency (between 0 and 1%/K on average) and the thermal equilibration time (150 ms for the used capillaries).

These values needed to be tweaked to adjust for the high differences in base temperature and salt concentration the measurements cover. Most measurement made it clear which combination of parameters were producing the correct prediction (although it can be a time consuming process). As mentioned, the slight change in overall brightness at the moment the temperature is changed determines the dye temperature dependence. At the end of the measurement the fluorescence signal is homogeneous throughout the field of view. This means that the diffusion has washed out the thermophoretic depletion on the scale of the camera view. But the imaged region likely still has a slightly lower concentration than the bulk solution. So this fluorescence has to be reconciled mostly with the bleaching time constant and the diffusion constant. At a radius beyond the main depletion region the fluorescence can temporarily go above the level of the unperturbed sample. This is the case if the thermophoretic depletion of the particles from the region with a strong temperature gradient is such that the diffusion is not sufficient to distribute the arriving particles efficiently and a shock front is formed. In some measurements this behaviour is present and of course accounted for by the simulation.

Evaluation is difficult if the difference in concentration between the unperturbed and the equilibrated thermophoretically depleted distribution was so small due to a low S_T value that even a slowly diffusing sample would reach that state in very little time. In this particular situation the fluorescence response to the changed temperature distribution and the thermophoretic depletion are basically occurring simultaneously. Even without temperature dependent quantum efficiency, the diffusion coefficient is very hard to determine. The uncertainty for these values is considerably higher then for the rest of the measurements. For the investigated samples, this only was the case in several measurement of temperatures below 25 °C and at high salt concentrations.

Using this process the diffusion coefficient D and the Soret coefficient S_T for all individual thermophoresis measurements were interpreted. These covered the ten different oligonucleotide samples at eight different base temperatures and salt concentrations each.

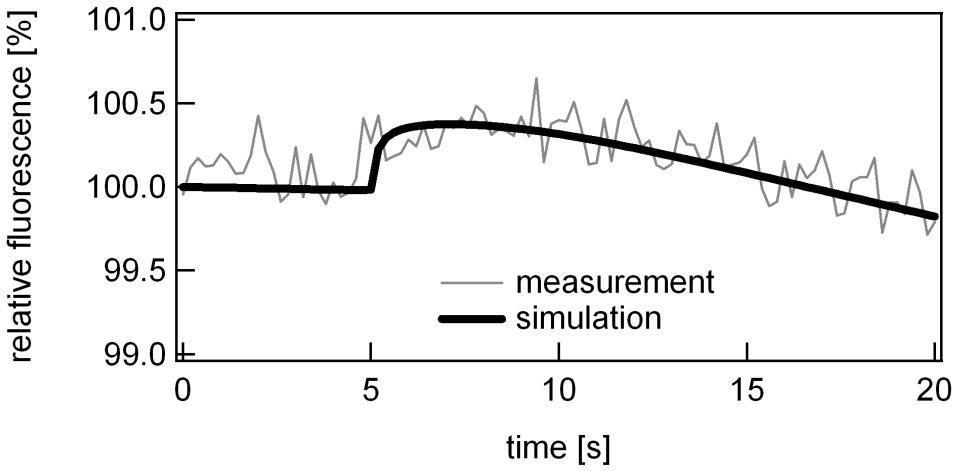

Figure 1.13: As thermophoresis depletes molecules from the heat center, the concentration can increase temporarily at some radii even for positive Soret coefficient. Distance from the beam center is about $84\mu m$. Some of the instantaneous increase in fluorescence at 5 seconds is due to the dyes temperature dependence.

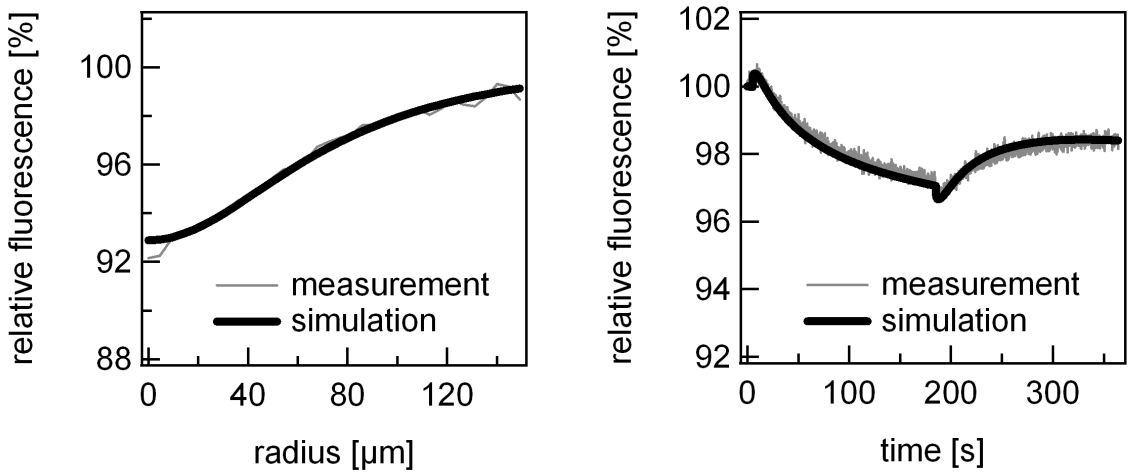

Figure 1.14: Comparison between measurement (gray) and simulation (black) for a horizontal (depletion vs radius) and a vertical cut (depletion versus time) through the distribution map. The selection is based on the yellow cursor in figure 1.11.

Both sets of values were transferred into the data analysis software IGOR pro (Version 5.03, by WaveMetrics) for further processing.

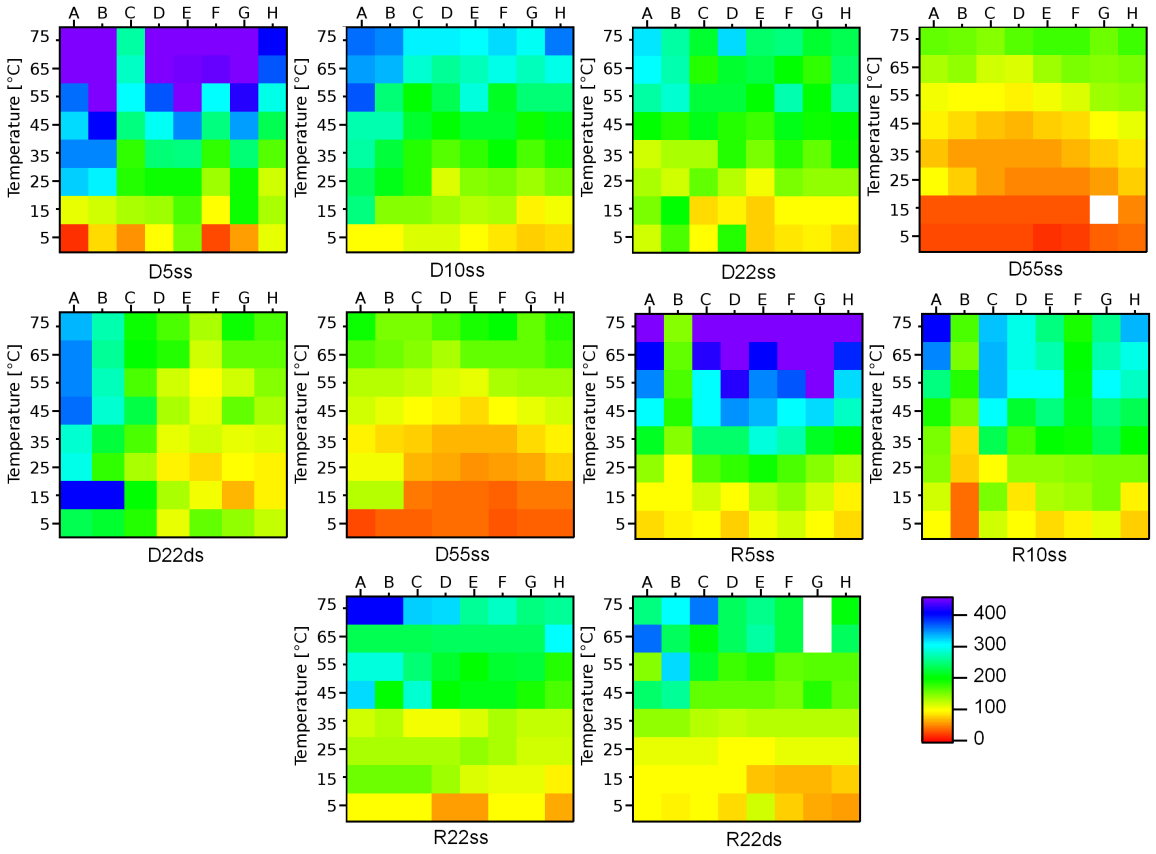

Figure 1.15: Diffusion values in $\mu m^2/s$ deduced from the thermophoresis measurements. For each oligonucleotide the columns are the salt conditions A - H (see table 1.2). The rows are the different temperatures from 5 °C (on the bottom) up to 75 °C in 10 °C increments. While the temperature dependence of the diffusion coefficient is evident, no clear trend for the salt dependence is apparent. The extraction of the diffusion coefficient lead to larger error for samples with low thermophoretic depletion. Low temperatures combined with high salt concentrations (on the left) were affected. So were the shortest samples D5ss and R5ss.

Temperature obviously has a strong effect on diffusion as seen in figure 1.15. Even short nucleotides have relatively slow diffusion at 5 °C. These samples also exhibit stronger overall noise than the bigger samples despite having the highest absolute values. The thermophoretic depletion they were derived from was not strong, leading to less certainty in the determination of the diffusion coefficient. The change of the diffusion coefficient across the different salt concentrations shows no clear global trend in these measurements as seen in figure 1.16.

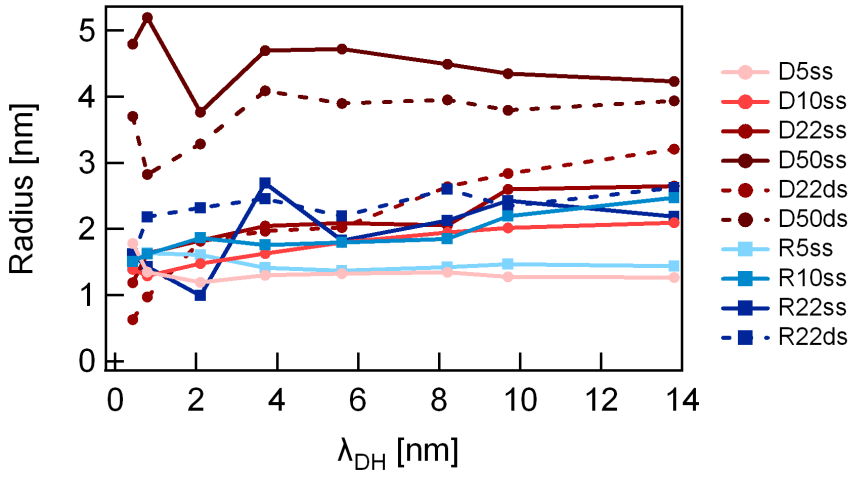

Figure 1.16: Radius of the DNA and RNA samples. Values were derived from the measured diffusion coefficients averaged over the measured temperatures.

To reduce the noise of the diffusion and the derived radius values, the diffusion values were averaged over λ_{DH} before the radius values were calculated. The initial analysis of the S_T values was done based on these radius values. The difference in temperature dependence of the radius between the different samples could be a topic for future investigations. An approach that can determine the diffusion values more accurately should be considered though.

From the diffusion coefficient values, radii were calculated using the Stokes-Einstein equation [17, 65].

$$r = \frac{k_B T}{6\pi\eta D}$$

The viscosity of water is temperature is temperature dependent [37]. The Stokes-Einstein equation is intended for spherical particles. Especially the double stranded samples deviate from this idealisation. The geometry of the double stranded helix is usually described as rod-like. While the calculated value of r does not reflect the accurate dimensions of the sample, the interpretation of the particle as spherical is consistent with the goal of investigating the applicability of the spherical capacitor model.

1.6 Results

The Soret coefficient S_T values were initially analysed focusing on their change over the ionic screening length λ_{DH} for the different temperatures independently. The expected size transition was found across all samples. Figure 1.17 shows the single stranded DNA samples and figure 1.18 the single stranded RNA samples. Please note that the values shown here are unmodified, measured Soret coefficients S_T. Equation 1.2 was fitted to these values with S_T^{NI} as a free parameter. The temperatures for these two figures were chosen, because the S_T^{NI} contribution is close to zero for all samples. S_T for the different samples can be compared and makes it easier to draw conclusions regarding S_T^{ionic} from them. Since the parameter changing along the horizontal axis is the ionic shielding length and the hypothesis is that the influence of charge on the thermophoresis can be explained based on the spherical capacitor model [13], the agreement between measurement and theory is encouraging.

As expected, we see stronger thermophoresis for larger particles constituting longer chains of nucleotides with a charged backbone. Furthermore the transition shifts to larger λ_{DH} values for longer polymers. Both of these observations are exactly what we expect from the spherical capacitor model.

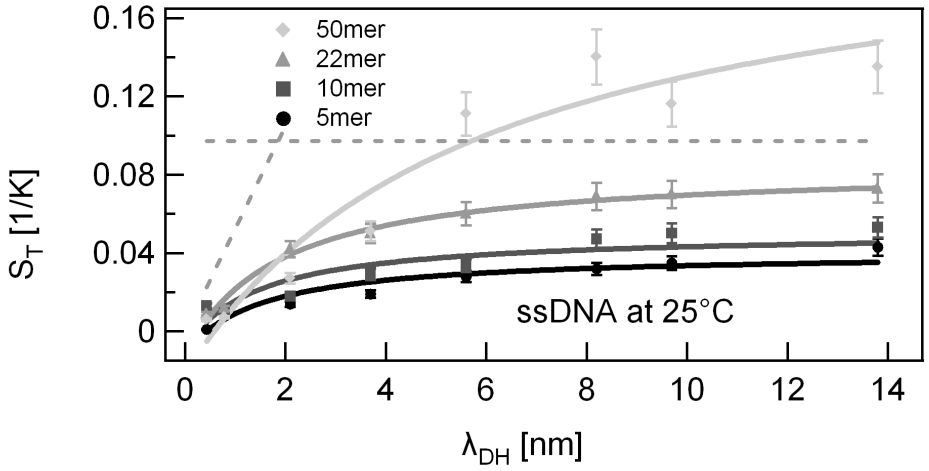

Figure 1.17: S_T of the single stranded DNA samples clearly show the expected transition from the initial steep increase with λ_{DH} to a slow approximation of a upper bound. Larger samples show stronger thermophoresis. Values given are for 25 °C.

Fits like in figure 1.17 yield S_T^{NI} as a fit parameter. The S_T^{NI} values—fitted for the different temperatures independently of each other—were plotted against temperature, as seen in figure 1.19. Given that these values had been through not one, but two fitting procedures, the agreement with S_T^{Piazza} is better than expected. This motivated the assumption that the temperature dependence of S_T^{NI} could be sufficiently described by S_T^{Piazza}.

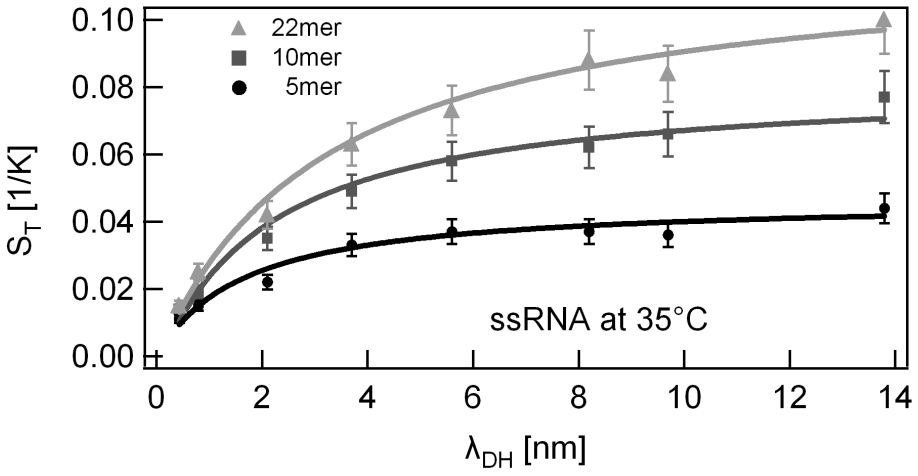

Figure 1.18: S_T of the single stranded RNA samples clearly show the expected transition from the initial steep increase with λ_{DH} to a slow approximation of a upper bound. Values given are for 35 °C.

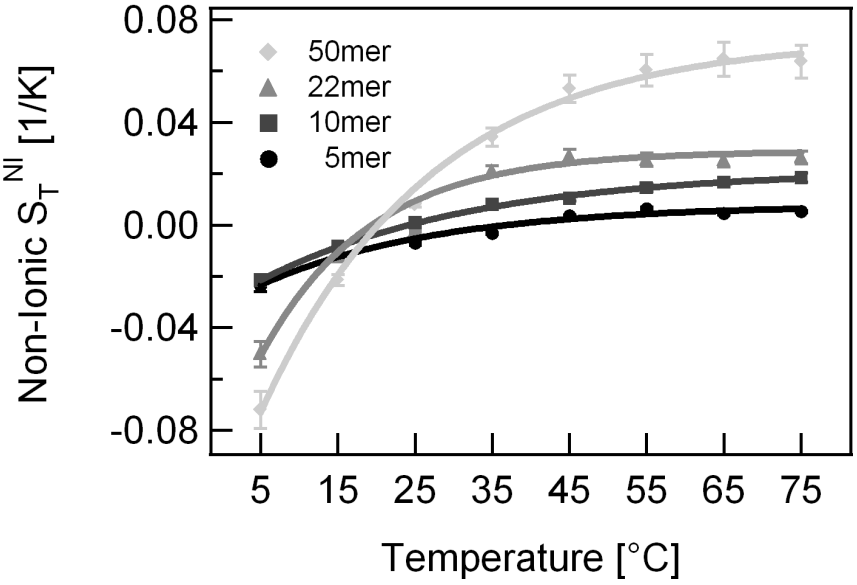

Figure 1.19: S_T^{NI} values for the single stranded DNA samples. These are the offsets of the S_T^{ionic} curves fitted to the S_T versus λ_{DH} curves like the ones shown in figures 1.17 or 1.17. The fit is based on S_T^{Piazza}.

A prediction from the interplay between S_T^{Piazza} and S_T^{ionic} is that for low salt concentrations the change of S_T with growing temperature would be towards higher values for low temperatures and then towards lower values for higher temperatures. In figure 1.20 this behaviour can be observed to varying degree as the ionic screening strength is altered. The extrapolated plot of S_T^{Piazza} for $\lambda_{DH} = 0$ is added to show the case of the perfectly shielded particle.

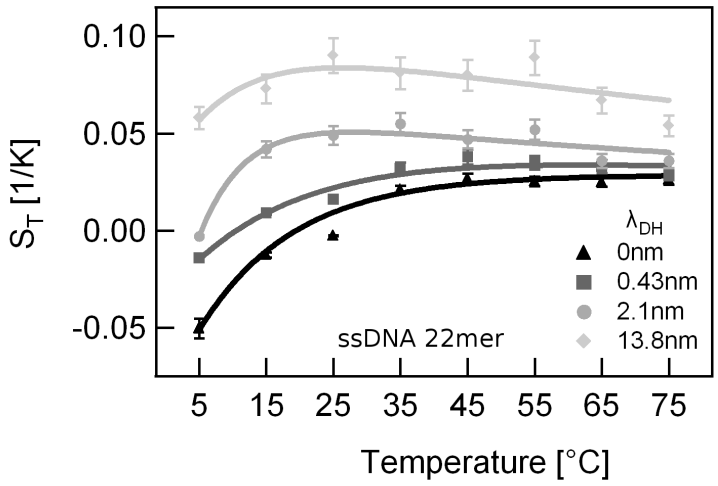

Figure 1.20: The oligonucleotide samples show the predicted interplay between S_T^{Piazza} and S_T^{ionic}. As salt concentration increases, this effect vanishes. The solid lines are based on the combined S_T

Combining S_T^{ionic} with S_T^{Piazza} allowed for a more comprehensive fit covering the temperature as well as the salt concentration dependencies in one evaluation. The results are shown in figure 1.25. Apart from the double stranded RNA sample the data could be fitted with good results. One reason for the different properties of the R22ds sample is that double stranded oligonucleotides are expected to denature for higher temperatures and lower salt concentrations. Why the DNA samples do not show the same behaviour can not inferred from the presented data. The fits shown in this figure assumed a particle size fixed to the value derived from the diffusion coefficients averaged over temperature as well as salt concentration. In part this was due to the fact that the interpolated fit values based on very noisy diffusion coefficient data set meant that the interpolation between the values calculated for the fit procedure would look as noisy as the measurement and the plots would be even harder to interpret than the presented values. Though the fits would converge, they were predictably erratic and overfitted in order to account for the radius data to the point where no coherence was to be found in the fit parameters. The presented fits are a trade-off. They restrain the radius to the range of values that the data can provide, while keeping the fit of the parameters to be determined by the fit unrestrained.

The initial rise of S_T for λ_{DH} values smaller than the size of the particle shown in figure 1.17 and flattening for values bigger than that size can be seen in horizontal cuts throughout the 2D maps of figure 1.25.

Vertical cuts through the data sets exhibit the interplay between S_T^{ionic} and S_T^{Piazza} already indicated by figure 1.20. The effect vanishes towards shorter Debye lengths as the increased shielding of the charges reduces the relevance of S_T^{ionic} for S_T.

From the 2D fit the following parameters are gained: The charge of the particle, as well as the three Piazza parameters S_T^{∞}, T^* and T_0. The particle charge was divided by the length of the oligonucleotide l in bases and normalised by the elementary charge:

$$Q_{perbase} = \frac{Q_{particle}}{l \cdot e}$$

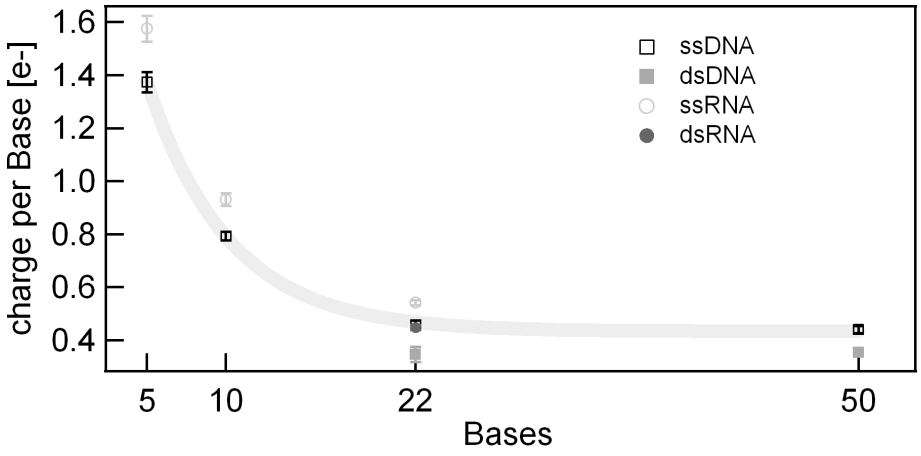

Figure 1.21: Charge of the particles normalised by the number of subunits. For short particles the charge of the dye has more impact. Double stranded samples show more effective shielding of the backbone charges.

The resulting $Q_{perbase}$ values (see table 1.3) are shown in figure 1.21. For small nucleotides we see a much higher charge than the value approached by longer samples. To a certain extent this can be attributed to the charge carried by the dye. For longer polymers these become less influential in the average charge per subunit. An additional factor is the limited ability to attract bound shielding charges for smaller polymers. Both effects are known from independent measurements of DNA's effective charge using electrophoresis [43, 42, 49, 56].

To fit the measurements, no dependence of charge on temperature was required (figure 1.25), confirming the universality of equation 1.1. No difference is found for RNA and DNA, reflecting the identical charge of their phosphate backbone and negligible contributions from the different sugar moieties. Double stranded DNA and RNA show nearly identical $Q_{perbase}$ values, despite the fact that one base-pair is counted as a single base, indicating an

Samples	$Q_{perbase}$ [e^-]	$Q_{perbase}$ sigma	S_T^∞ [1/K]	S_T^∞ sigma
D5ss	1.37	0.037	0.0008	0.0024
D10ss	0.79	0.016	0.0143	0.0019
D22ss	0.46	0.016	0.0144	0.0035
D50ss	0.44	0.013	0.0457	0.0056
R5ss	1.58	0.049	0.0029	0.0016
R10ss	0.93	0.024	0.0045	0.0026
R22ss	0.54	0.010	0.0128	0.0041
D22ds	0.35	0.028	0.0397	0.0048
D50ds	0.35	0.012	0.0433	0.0054
R22ds	0.45	0.010	0.0138	0.0019

Table 1.3: Normalised particle charge and Piazza value S_T^∞ derived from the 2D fit.

effective local shielding of the backbones or effects of the significantly enhanced persistent length. The charge per base pair drops to 0.35 e^- for double stranded DNA, converging well to the previously published value of 0.12 e^- for long DNA in the range of 50-50000 base pairs [16].

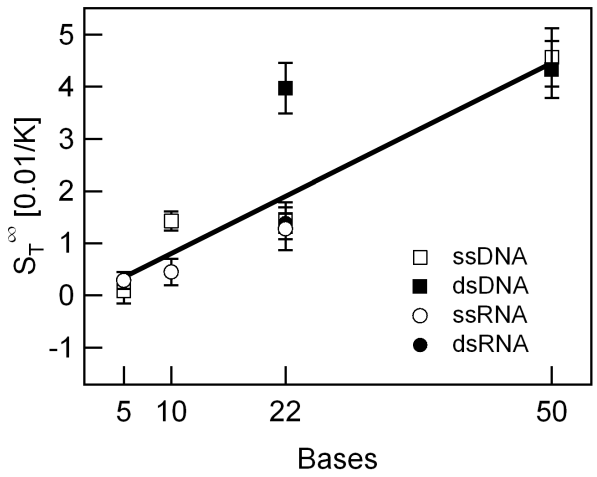

Figure 1.22: S_T^∞ plotted against the hydrodynamic radius R.

As seen in figure 1.22, the amplitude of non-ionic thermophoresis S_T^∞ (see table 1.3) increases linearly with the length of the oligonucleotide. Such linear trend would be expected for short range hydrophobic interactions with oriented water along the length of the polymer. An offset of the linearity is almost negligible, suggesting a minor contribution from the polymer ends (including the dye) as expected.

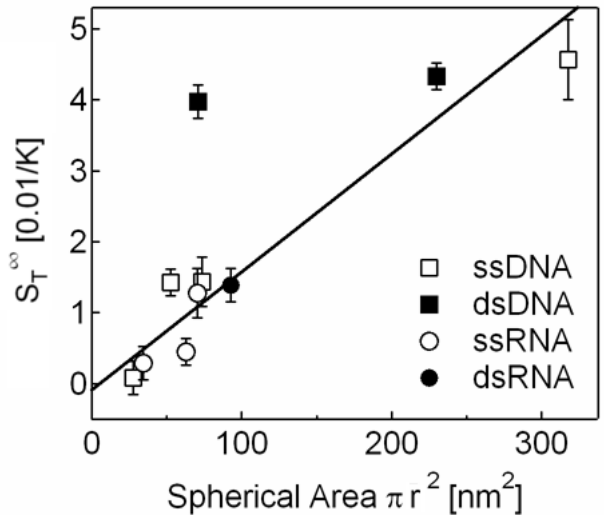

Figure 1.23: S_T^∞ plotted against the surface of a spherical particle with size r.

In figure 1.23 non-ionic amplitud S_T^∞ is plotted against the surface of a spherical particle calculated from the experimentally determined hydrodynamic radius R. Compared to figure 1.22, a similar linear relationship is found. With the data at hand, it is therefore not possible to distinguish between short ranged hydrophobic effects or other ion-independent contributions which scale with the spherical long ranged area of the molecule.

In contrast to the amplitude value S_T^∞, which scales roughly linearly with the size of the particle, no clear interpretation could be found for the parameters T^* and T_0 which is documented in table 1.4.

As seen in figure 1.24, thermophoresis of single and double stranded DNA and RNA with a length of 22 bases is very similar at physiological salt concentrations (λ_{DH}=0.8nm). Single stranded molecules have a higher Soret coefficient than their double stranded versions at lower salt concentration: For double stranded samples we expect the separation of the two strands at high temperatures. Furthermore at lower salt concentrations and thus higher λ_{DH} the compromised charge shielding of the oligonucleotide backbones lowers the melting temperature. As a result, for temperatures higher than the shown 25 °C oligonucleotides samples with complementary binding partners approach the single stranded values, an effect which was already used to determine DNA melting transitions with thermophoresis [71].

Sample	T_0 [°C]	T_0 sigma	T^* [°C]	T^* sigma
D5ss	17.9	4.3	43.3	12.6
D10ss	18.7	2.7	21.2	2.4
D22ss	7.5	2.0	13.3	2.6
D50ss	14.1	2.7	15.0	1.9
R5ss	8.1	4.0	15.7	6.3
R10ss	12.5	3.1	28.2	7.5
R22ss	23.3	3.7	43.7	5.2
D22ds	11.6	2.8	9.1	1.7
D50ds	11.8	2.4	13.0	1.9
R22ds	15.1	1.8	23.0	2.2

Table 1.4: Piazza values T_0 and T^* derived from the 2D fit.

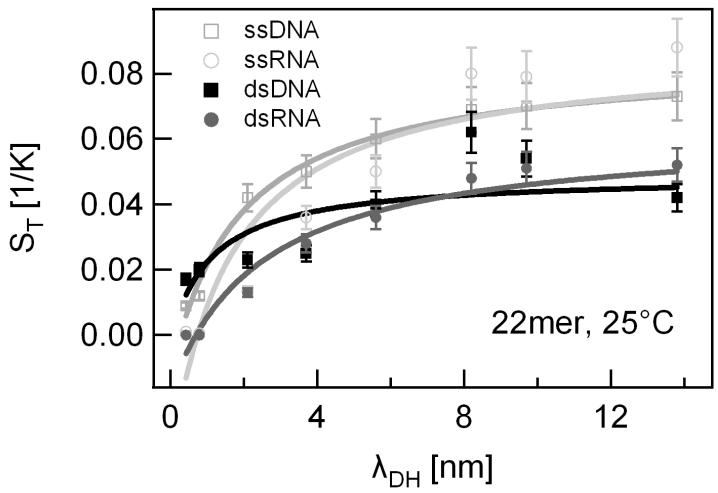

Figure 1.24: Comparison between S_T of single and double stranded oligonucleotides. For low salt conditions single stranded samples show stronger thermophoresis. At high salt conditions the differences between the samples are diminished.

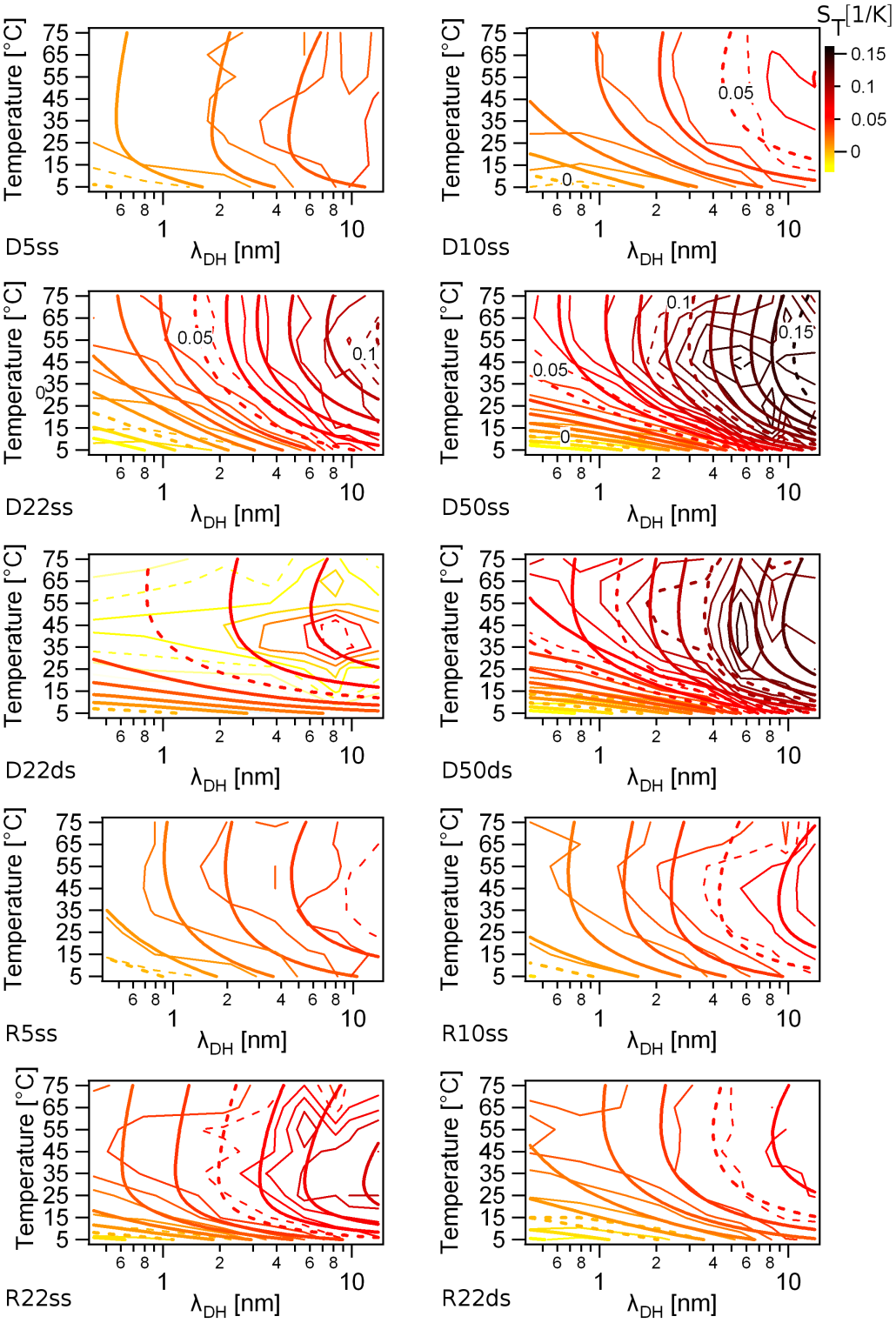

Figure 1.25: Soret coefficent S_T value of all samples. Thick lines are the fits of $S_T^{ionic} + S_T^{Piazza}$. With the exception of D22ds the fitting procedure could reproduce the change of thermophoresis over a wide range of temperatures and salt concentrations. The spherical capacitor model can fully account for the salt dependent sample behaviour measured.

1.7 Conclusion

The thermophoresis of short DNA and RNA strands in aquous solutions was measured. The setting allowed probing ionic thermophoresis across a previously untested transition where the hydrodynamic radius R drops below the Debye length λ_{DH}. Beyond the previously explored linear raise of the Soret coefficient S_T for $\lambda_{DH} < R$, a saturating Soret coefficient for $\lambda_{DH} > R$ was found. The position of the transition depends on the hydrodynamic radius. This behaviour in detail confirms the prediction for thermophoresis by Dhont et.al [13] using a capacitor model of thermophoresis. The experiments corroborate that the ionic contribution of aqueous thermophoresis is adequately described by a microscopic theory over a wide range of parameters.

Non-trivial dependencies of thermophoresis for a very large range of salt concentrations and temperatures in a critical DNA and RNA length range can be predicted with the confirmed model.

The experiments give new impulses to the discussion regarding the role of secondary electrical fields in thermophoresis.

These results allow for a better quantitative understanding of thermophoresis on a microscopic level. This added theoretical understanding is further optimizing the quantification of biomolecule affinity.

Chapter 2

Cooperativity

2.1 Introduction

Binding between molecules is considered cooperative if the presence of an additional partner changes the affinity between a set of molecules. In this chapter, thermophoretic measurements are presented as a tool to measure the complex binding behaviour of more than two partners. The procedure is very flexible and only requires for one binding partner to be labeled.

2.1.1 Importance of cooperativity

Many systems in the field of biophysics are highly complex and noisy [33]. Even the most simplified cell models are still densely populated with functional units to the point, where diffusion in such a crowded milieu shows significantly different properties than free diffusion. Biomolecules in cells are perpetually in close contact with many different potential binding partners [75]. The highly functional processes inside each cell rely on specific binding, retention, triggered joining and dissolving of temporary complexes and many other mechanisms, which involve positive as well as negative cooperativity [11, 25, 1, 2, 70, 51, 27, 36, 50]

Many of the known mechanisms employed in e.g. gene expression rely on interaction of more than two partners [19, 53, 66, 20]. Transcription from genomic DNA into mRNA involves binding of the enzyme RNA polymerase to the DNA, which is moderated by activators or repressors. After successful docking, supply of ATP and mono-nucleotides is necessary for the transcription to proceed. This oversimplified view of one of the essential processes in cellular life shows the importance of understanding the complex interaction of more than merely two partners to grasp the intricacies involved. Separation of time scales and a stepwise approach for binding events interpreted as being hierarchical grant access to a lot of systems. However, a more flexible view on cooperativity would allow analysis of more complex systems. One such approach will be presented here.

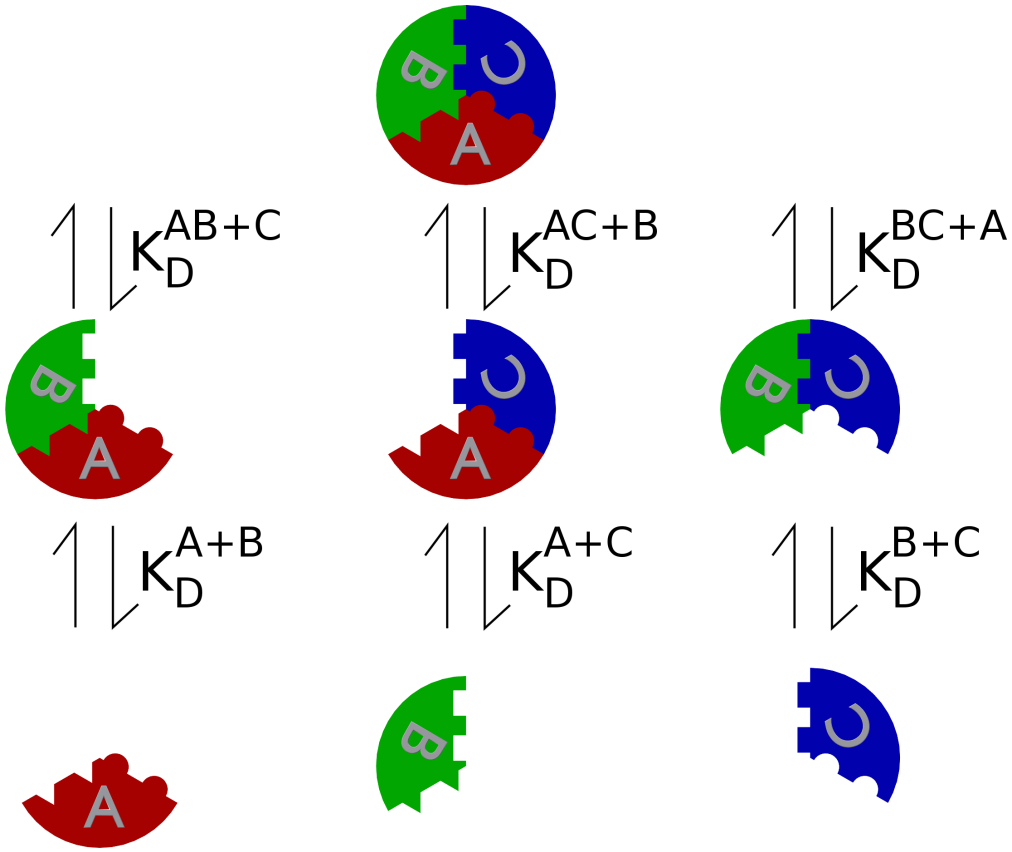

Figure 2.1: Binding scheme of a trimer. Each of the three parts are able to bind to each other. Six binding constant define the binding behaviour of the structures.

2.1.2 Investigating cooperativity by means of thermophoresis

As discussed in the first chapter, thermophoresis is influenced by a lot of particle properties. Given a particle, it is very likely that different binding configurations of that particle will differ in their respective thermophoresis amplitude. Let's assume that the local concentration of that particle can be ascertained experimentally (i.e. by fluorescence). A solution of binding partners will equilibrate to a distribution of binding partners in different bound and unbound states. The concentrations of these different states will of course depend on the amount of partners present, as well as on the probability of the partners in question to be bound in a given constellation, i.e. the different binding affinities. Obviously, temperature and buffer composition have a large impact on the binding as well. For the presented approach to be versatile, these parameters are not used to probe the binding events. In many cases they are predetermined by the system under investigation. For example, many interesting protein complexes are fine tuned to show their properties at around 37 °C and in physiological solution only. Thus, this discussion is focussed on deriving the information about the interaction from measurements under comparable conditions with constant temperature and buffer composition.

Recently a number of measurements using thermoporesis to investigate molecule interactions in the field of life sciences were conducted, such as measurement of the binding affinity of proteins [72], including the relevant cases of antibody binding in serum [38], sensing with GPCR receptors [67] [10], aptamer binding [4] and small-molecule binding for pharmaceutical applications [72] [62] [48]. A lot of these works could be expanded by using the proposed cooperativity measurement.

The cooperativity measurement proposed in this work uses the thermophoretic depletion signals discussed in chapter 1 for a broad range of binding partner concentrations to infer the binding strengths. To do so, the simulated steady state concentrations of the possible binding aggregates resulting in the mean depletion signal are adjusted to fit the actual depletions using a sophisticated fitting procedure. The fitting parameters yield the binding constants from which the cooperativity of the system is derived.

2.2 Theory

Before we can move on to systems exhibiting cooperativity, we first have to define how to describe the interaction that will be affected by cooperativity.

2.2.1 Introduction to molecular binding

Imagine different types of molecules, each present at a certain concentration in a solution. These concentrations determine the frequency of pairs of molecules getting into close proximity within the solution. A number of other properties are influencing binding, and most are not as easily controlled as the concentration: the molecules' orientation, the accessibility of the binding pocket at the moment of contact and other factors, which all influence whether binding takes place. The details of the interaction need not necessarily be known to determine the affinity though. These factors are summed up into the enthalpic and entropic changes upon binding and unbinding. As long as the different aggregates of the binding partners can be distinguished based on a measurement signal, one can try to infer the relevant affinities of the system.

To start, consider the simplest situation to describe binding in: The binding between two partners. (One might argue that internal refolding and binding in a hairpin-like structure is simpler, but it is not suited for the discussion of concentration dependent properties.) In general, the two binding partners will bind reversibly:

$$A + B \leftrightarrows AB.$$

The dynamic equilibrium of a solution of molecules A and B is described by the law of mass action [22]. At any given moment a certain fraction of AB complexes falls apart into unbound A and B. At the same time some A and B will bind, adding to the concentration of AB. The higher the amount of A and B available for binding, the higher the likelihood for binding to take place.

$$\frac{d}{dt}AB = k_{on} \cdot A \cdot B - k_{off} \cdot AB$$

$$\frac{d}{dt}A = -k_{on} \cdot A \cdot B + k_{off} \cdot AB$$

$$\frac{d}{dt}B = -k_{on} \cdot A \cdot B + k_{off} \cdot AB$$

If the system is allowed to go into steady state, creation and decay of complexes cancel each other and the concentrations of complexes and unbound partners are no longer changing. In this case, all the time derivatives vanish.

$$\frac{d}{dt}AB = \frac{d}{dt}A = \frac{d}{dt}B \overset{steady-state}{=} 0$$

With this we can express the ratio of the kinetic rates with the steady state amounts.

$$\frac{k_{off}}{k_{on}} = \left(\frac{A \cdot B}{AB}\right)_{steady-state} =: K_D$$

The dissociation constant K_D describes the affinity between the two partners A and B. The association constant $K_a = 1/K_D$ is also used, as well as the equilibration constant K_{eq}, which is usually equal to K_a. All of these have been abbreviated as K one time or another in literature [27, 11]. To not make things unnecessarily complicated, I will use K_D and write it as such.

Depending on the stoichiometry of the binding process, the unit of K_D usually is a concentration of the product of concentrations measured in Mole/liter or Molar (symbol M).

$$A + B \rightleftharpoons AB : [K_D] = M = \frac{mol}{l}$$

$$A + B + C \rightleftharpoons ABC : [K_D] = M^2$$

Please note that the way it was introduced here, the binding $A + B + C \rightleftharpoons ABC$ means that A, B and C bind directly into the trimer. The intermediate creation of a dimer is ignored, even though it is on the order of a million times more probable than the spontaneous joining of three freely diffusion binding partners. In this work the creation of a trimer from three monomers is interpreted as two successive two-partner binding processes. Only elementary reactions adding or removing one molecule at a time from an aggregate are considered. The different paths these reactions can take will be discussed later on in section 2.2.3. However, the model this work is based on limits the possible aggregates to monomers, dimers and trimers. No bigger aggregates are considered. As long as the "on" direction of the reaction is pointing towards a configuration of the binding partners, in which fewer concentrations are tallied, the exponent of the concentration should remain positive. Constrained to elementary reactions, all K_D values discussed in this work have the unit of a concentration.

If only information about the steady state is accessible, k_{on} and k_{off} are not known, only their ratio K_D. To measure kinetic rates, time traces of the system reacting to a change need to be recorded [2]. An observable connected to the concentration distribution needs to be measured upon a change in the system (temperature jump or sudden change of the ratio of binding partner concentration for example [34]). Since cooperativity is defined by steady state properties, the kinetic rates k_{on} and k_{off} are not relevant for measuring it, only their ratio K_D. The kinetic rates and their measurement will therefore not be discussed in detail in this work.

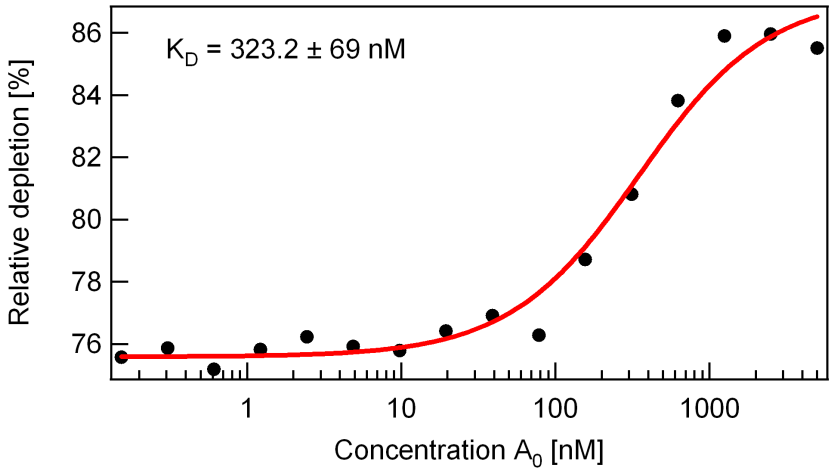

Figure 2.2: A standard K_D measurement with two binding partners can be performed with a simple titration series. Fluorescence depletion curve for a titration curve with the labeled binding partner at a fixed concentration. The fitted K_D is $323.2 \pm 69 nM$. For two partners the measurement is well established.

To measure the interaction of two binding partners A and B, one concentration can be kept fixed (the labeled binding partner) and the other binding partner is titrated. Let A be the labeled partner in this example. In a thermophoresis experiment [12, 23, 29, 52, 55, 74, 64] the fluorescence change upon a change in the local temperature distribution (see the discussion in chapter 1.4.1) is representative of the combination of unbound A and bound AB in the sample at hand, depending on the concentration of B in that sample. From the known A_0 and B_0 for each of the samples one can derive K_D based on the measured change in thermophoretic depletion using:

$$\frac{AB}{A_0} = \frac{K_D + A_0 + B_0 - \sqrt{(K_D + A_0 + B_0)^2 - 4A_0B_0}}{2A_0}$$

Which can be derived the following way:

$$K_D = \frac{A \cdot B}{AB}$$

with $A = A_0 - AB$ and $B = B_0 - AB$, this can be rewritten as

$$K_D = \frac{(A_0 - AB) \cdot (B_0 - AB)}{AB} = \frac{A_0 \cdot B_0 - A_0 \cdot AB - B_0 \cdot AB + AB^2}{AB}$$

$$AB^2 - AB \cdot (K_D + A_0 + B_0) + A_0 \cdot B_0 = 0$$

Solving this quadratic equation give:

$$AB = \frac{K_D + A_0 + B_0 \mp \sqrt{(K_D + A_0 + B_0)^2 - 4 \cdot A_0 \cdot B_0}}{2}$$

To discern, which solution (+ or −) is relevant, consider the situation of a solution without B_0. Certainly, the concentration of AB has to be 0, discarding the + as a viable option.

Therefore we can define θ as the fraction of all A molecules bound in an AB complex and call it the fraction bound:

$$\theta = \frac{AB}{A_0} = \frac{K_D + A_0 + B_0 - \sqrt{(K_D + A_0 + B_0)^2 - 4 \cdot A_0 \cdot B_0}}{2 \cdot A_0}$$

This equation is used to derive the K_D value for two partner binding from thermophoresis measurements, as outlined in 2.3.3.

2.2.2 The cooperative effect

The ratio of the dissociation constant with and without the cooperative partner being present is called the cooperative effect *Ce*. Here, the binding of A to B is altered by C being bound to A:

$$Ce^{A(C)+B} = \frac{K_D^{A+B}}{K_D^{AC+B}} = \frac{e^{-\frac{\Delta G^{A+B}}{k_B T}}}{e^{-\frac{\Delta G^{AC+B}}{k_B T}}} = e^{\frac{\Delta G^{AC+B} - \Delta G^{A+B}}{k_B T}}$$

The change in binding energy brought about by the presence of C being attached to A can be calculated from this.

$$\Delta(\Delta G^{AC+B \leftrightarrow A+B}) = k_B T \cdot ln(Ce^{A(C)+B})$$

The value of the cooperative effect *Ce* can be above or below unity. If it is bigger than one, the binding gets stronger in the presence of the cooperative partner. A *Ce* smaller than one corresponds to a reduction of the affinity of the primary binding partners in the presence of the cooperative partner. At unity, the cooperative partner has no apparent influence on the interaction. Since K_D is a concentration independent property, so is *Ce*.

There are six different K_D values that define the steady-state concentrations of the possible aggregates made up of three binding partners. Three for the creation of a dimer:

$$\begin{array}{ccc} A + B & A + C & B + C \\ \Updownarrow \quad K_D^{A+B} & \Updownarrow \quad K_D^{A+C} & \Updownarrow \quad K_D^{B+C} \\ AB & AC & BC \end{array}$$

and three for the creation of a trimer:

$$\begin{array}{ccc} AB+C & AC+B & BC+A \\ \Updownarrow \quad K_D^{AB+C} & \Updownarrow \quad K_D^{AC+B} & \Updownarrow \quad K_D^{BC+A} \\ ABC & ABC & ABC \end{array}$$

They can be combined into six different Ce values:

$$Ce^{A(C)+B}, Ce^{A(B)+C}, Ce^{B(C)+A}, Ce^{B(A)+C}, Ce^{C(A)+B}, Ce^{C(B)+A}$$

But are there actually six different cooperativity parameters necessary to define the cooperative nature of a three partner binding complex?

2.2.3 Closed loops in binding diagrams

Consider the binding of A to AB, then the binding of AB to ABC, then the decay of ABC into AC and further into A shown in figure 2.3. This constitutes a closed loop of binding and unbinding events, all of which are reversible processes. Going through the loop leaves the system in exactly the same state as at the beginning. Any closed circular process like this has a net energy change of zero, because otherwise energy would be created without any work being done to create it. Since $K_D = e^{-\frac{\Delta G}{k_B T}}$, the product of the K_D values, with decay steps factoring in as $1/K_D$, has to be one. This requirement is a direct result of the conservation of energy and as such applies to binding systems in general.

This of course holds for the loops starting with A and C as well. Thus it follows that:

$$K_D^{AB+C} \cdot K_D^{A+B} = K_D^{AC+B} \cdot K_D^{A+C} = K_D^{BC+A} \cdot K_D^{B+C}$$

which corresponds to:

$$\Delta G^{AB+C} + \Delta G^{A+B} = \Delta G^{AC+B} + \Delta G^{A+C} = \Delta G^{BC+A} + \Delta G^{B+C}$$

An analogy to Kirchhoff's second law (the loop rule) can be drawn. For the measurement, this means that by deriving an opportune set of four K_D values, for example the dimer affinities and one of the trimer affinities, all affinities are known.

This leads to an interesting implication for cooperative binding:

$$\frac{K_D^{AC+B}}{K_D^{A+B}} = \frac{K_D^{AB+C}}{K_D^{A+C}}$$

Thus:

$$Ce^{A(C)+B} = Ce^{A(B)+C} =: Ce^{A}$$

And by the same token:

$$Ce^{B(C)+A} = Ce^{B(A)+C} =: Ce^{B}$$
$$Ce^{C(A)+B} = Ce^{C(B)+A} =: Ce^{C}$$

The cooperativity does not discern which binding partner binds newly to a monomer or dimer. In light of K_D and Ce being steady-state properties, it seems consistent that chronology of binding is not relevant.

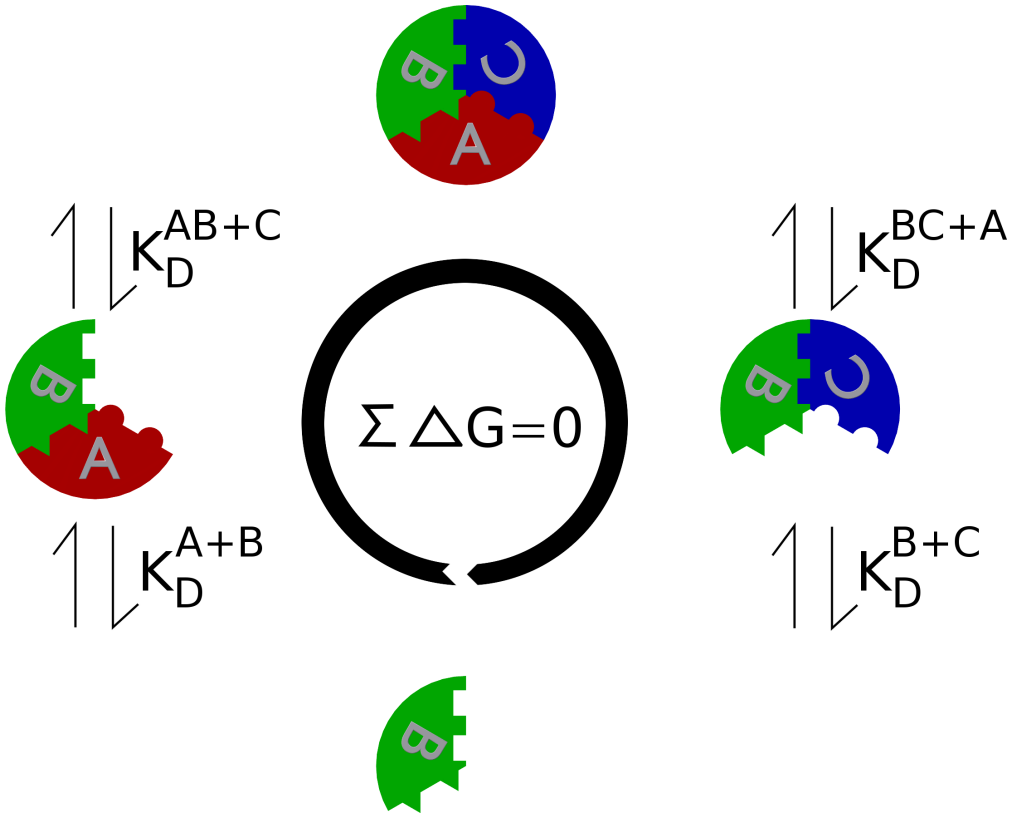

Figure 2.3: A closed loop composed of reversible binding and unbinding processes has to have a net change in Gibbs free energy of zero, otherwise energy conservation is violated. As a direct result of this for the shown loop it follows that $K_D^{AB+C} \cdot K_D^{A+B} = K_D^{BC+A} \cdot K_D^{B+C}$.

2.2.4 Simple concept, hidden complexities

While binding constants can be readily acquired with a measurement of fraction bound, this scheme is restricted to two partners. The following discussion will illustrate why a more complex measurement approach (presented in this work) is necessary.

Can the scheme presented in section 2.2.1 on page 39 be extended to measure the difference between binding with and without a cooperative binding partner present? It can, but only if for example C only binds to A and the fraction of A bound as AC can be pushed to unity [11]. Adding the cooperative C at a very high concentration will result in virtually the whole population of A being bound to C. Using this C saturated concentration as the stock for the titration of B will determine $K_D^{AC+B} = \frac{AC \cdot B}{ABC}$.

Although this approach is simple and sufficient to investigate that particular change in binding affinity, it is only correct if all assumptions apply. In this example, the premise included that C will only bind to A and through its presence exclusively change the affinity A has for B, thus only affecting B indirectly. This can only be correct if B does not bind to C. As soon as it does, the over-abundance of C in the solution (to keep $\frac{AC}{A_0}$ close to 1) will result in at least part of B being bound to C. This species is not accounted for by

this simple approach at all. Thus, a more complete approach to measuring cooperativity is called for.

It is easy to consider the measurement method outlined above as sufficient, if one thinks about cooperativity assigning clear roles to the involved binding partners. Though this is instructive and a common approach [2], it is not sufficient to probe cooperative effects in general as seen above. To show this, let the involved actors be called substrate S, ligand L and affinity modifier M. In absence of M, there will be a certain amount of complexes SL and a certain amount of unbound S and L.

$$\frac{S \cdot L}{SL} = K_D^{M=0}$$

Now the question is: How is the binding affinity associated with $K_D^{M=0}$ altered by adding the helper M? The question asks only what fraction of S is bound to L, which can be implemented experimentally using e.g. FRET [21]. For the calculation of K_D the signal will not discern between S and SM, L and LM, or SL and SLM.

$$K_D^M = \frac{(S + SM) \cdot (L + LM)}{SL + SLM} \overset{ignoring M}{=} \left.\frac{S \cdot L}{SL}\right|_M$$

But there is no way to recover K_D^{SM+L} from this, which would tell us about the cooperative effect.

$$K_D^M = \frac{(S + SM) \cdot (L + LM)}{SL + SLM} \neq \frac{SM \cdot L}{SLM} = K_D^{SM+L} = \frac{K_D^{S+L}}{Ce^S}$$

While K_D^M may carry relevant information about the binding, it does not lead to the cooperative effect Ce let alone the complete characterisation of the three binding partner interactions. Therefore, a new approach to measuring cooperativity is needed.

2.3 Materials and Methods

This part covers the oligonucleotide samples, the measurement setup and the procedures used for the analysis of the measurements.

2.3.1 DNA trimer

To investigate the measurement of cooperativity, a customisable experimental model system is required. We chose DNA, since the interaction between two single strands can be easily modified by changing the length of their binding motives, alter the average binding strength by tweaking the CG content or even introducing mismatches in the hybridising regions. Estimates of the binding energy of hybridised oligonucleotides are easily predicted using implementations of tools like mfold [76]. Furthermore, DNA is routinely labeled with fluorophores.

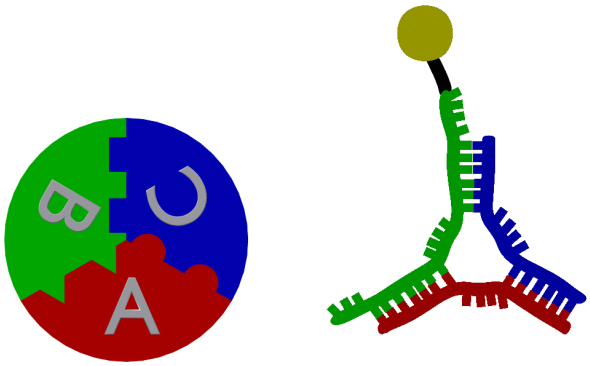

Figure 2.4: To investigate the cooperativity measurement DNA strands were designed to bind in a star pattern. The central region has a non-binding 5 T motive. Binding regions could be modified in length by changing strand A and C to change binding properties without altering the labeled partner. B was used in labeled and unlabeled version. The fluorophore Cy5 was covalently linked to the 5'-end of the B^* strand.

Figure 2.4 shows schematic views of the DNA trimer design. The 5' end of the A strand binds to the 3' end of the B strand. The 5' end of the B strand (synthesised with the covalently linked fluorescent dye Cy5 in case of B^*) and the 5' end of C binds to the 3' end of A. Between the two binding regions on each of the oligonucleotides (A,B and C) a motive of five thymine bases was inserted (that would remain unbound in all dimer and trimer aggregates) to increase the flexibility of the construct and separate the binding regions from each other, which should lead to a reduction in unwanted interactions. Unlabeled strands were ordered with the binding regions at different length. This way there was more flexibility in the combination of binding partners. The DNA for all experiments presented here were ordered from IBA GmbH (Göttingen, Germany).

For the label we chose the fluorophor Cy5 as a 5'-end modification (absorbance maximum at 649 nm, emission maximum at 670 nm). Though temperature dependence and bleaching properties could be better, a lot of analysis tools at our disposal are compatible with this dye. The oligonucleotide B was the longest sample used. This and the linker connecting the dye to the backbone provided some distance between the binding region and the dye. While it is possible that the fluorescence is influenced by the presence of one or two binding partners, for this application that factor can be absorbed into the thermophoretical depletion value and is not problematic.

B was ordered in a labeled and n unlabeled version. While it was used with maximum binding motives of two times 20 bases, the symmetric binding structure was selected by comparing the binding of B to A and C oligonucleotides truncated to different lengths. Altering the unlabeled samples A and C allows for lots of combinations for three partner binding at low cost.

All samples were measured in standard PBS buffer with the salt concentration adjusted to 300mM NaCl.

Part	Sample	Sequence
A	A16-17	5'- CTC AAT TCC TAA TCG CTT TTT TTC TAC TGG ACA AAG TG - 3'
B	B20-20	5' - AGA GCA GCT TAA ACT CGA AGT TTT TGC GAT TAG GAA TTG AGA TGG - 3'
B*	B+20-20	5' - Cy5 - AGA GCA GCT TAA ACT CGA AGT TTT TGC GAT TAG GAA TTG AGA TGG - 3'
C	C17-16	5' - CAC TTT GTC CAG TAG AAT TTT TCT TCG AGT TTA AGC TG - 3'

Table 2.1: Sequences of the DNA components of the three partner binding complex.

2.3.2 Measurement setup

In many regards the measurement setup is a replica of the one used for the measurements in chapter 1. Objective, microscope body, LEDs and LED drivers as well as laser are the same or identical (see section 1.3.1 on page 7). This time, however, a photo-multiplier was used for fluorescence detection (Excelitas Technologies, MP-1383). The software is different but allows to replicate a standard thermophoresis experiment as outlined in chapter 1. Here, the timing included 12 seconds of recording without the laser, 60 seconds of the samples depleting in response to the laser heating, followed by 60 seconds of back-diffusion.

The sample stage consists of a broad slab of 0.5 mm thick silicon waver (about 8.5 cm wide) resting on three Peltier elements powered in series. This allows the placement of many more samples next to each other then was possible with the earlier design used in chapter 1. The highest number of samples measured for this experiment was 52 capillaries in one measurement block.

The base temperature is actively regulated through a feedback loop. Capillary handling again is equivalent to what is outlined in chapter 1. The temperature distribution in the sample liquid was measured to have a peak temperature increase of ΔT_{max} =2.26 °C with a Lorentzian HWHM width of $42\mu m$.

2.3.3 Thermophoretic measurements of two partner interactions

The measurement of fluorescence intensity monitors the concentration of fluorescently labeled molecules (A in the discussion of section 2.2.1, B^* in the measurements). For the binding of two partners, this means that monomer and dimer will (usually, unless $S_T = 0$) react to local heating by changing concentration as elaborated in chapter 1. Since the binding constant K_D can be derived from known fraction bound values in a series of probes with known constant concentrations (section 2.2.1), if we measure the fluorescence signal change $\frac{f}{f_0}$ of the mixture of aggregates, we expect that value to change along the titration series from $\left(\frac{f}{f_0}\right)_{monomer}$ to $\left(\frac{f}{f_0}\right)_{dimer}$ according to:

$$\frac{f}{f_0}(\theta) = \left(\frac{f}{f_0}\right)_{monomer} + \left(\left(\frac{f}{f_0}\right)_{dimer} - \left(\frac{f}{f_0}\right)_{monomer}\right) \cdot \theta$$

As long as the titration series covers enough samples where the fraction bound is negligible ($\theta \approx 0$) and saturated ($\theta \approx 1$), K_D can be derived. If enough measured samples are given in the necessary concentration region so that the curvature (or better still curvatures) of the θ transition is known, a narrower measurement window can still yield K_D.

As a side note, binding behaviour can also be investigated by measuring a set of binding molecules at different temperatures instead of different concentration ratios. Then, the measured data is called a melting curve [47]. Since the Soret coefficient S_T in general has an intricate temperature dependence, it is not even sufficient to assume a linearly sloping baseline for the thermophoretic fluorescence changes $\left(\frac{f}{f_0}\right)_{monomer}$ and $\left(\frac{f}{f_0}\right)_{dimer}$ [71].

Lacking a analytical description, the evaluation of the K_D values for the case of more than three binding partners needs a different approach.

2.3.4 Thermophoretic measurements of interactions of three or more partners

The new approach for measuring the complete binding interaction and cooperativity presented in this work can be summarised as follows: A representative set of concentration combinations of the binding partners under investigation is measured. The measurements in question determine the thermophoretic depletion. Then, the K_D values and thermophoretic depletion responses (if not already known) are fitted to the recorded data set. As Deutman et. al put it [11], one would like to determine the magnitude of cooperative effects from a single experiment.

As with many fitting procedures [44], the difference between a given data set under investigation (usually based on measurements) and the data calculated for a model primed with a set of candidate fitting parameters is minimised by changing the parameter candidates. The goodness or quality of fit χ^2 is the measure of the mentioned difference and defined as $\sum_{samples}(value_{measured} - value_{simulated})^2$. The goal is finding an optimal set of fitting parameters. The model is solved again and again in hope for the fit procedure to converge and to return the optimal fitting parameters.

For every combination of monomer concentrations present in a given sample, the steady-state concentrations of all the possible aggregates (all the monomers, dimers, trimers, and possibly more) can be calculated based on a complete set of K_D values. Combining the derived set of concentrations with the depletion values of the different aggregates yields the depletion expected for those parameters.

In case of just two partners binding and one being labeled, $\frac{AB}{A_0}$ and $\frac{A}{A_0} = 1 - \frac{AB}{A_0}$ based on the analytic function derived earlier (section 2.2.1 on page 39) gives the steady-state concentrations of the labeled species. Exchanging A for B yields the steady-state concentrations of the unlabeled species as outlined in section 2.3.3. Therefore, we can readily extract the relevant parameters for two-partner binding by fitting.

In general, however, an analytical expression for the steady-state concentrations of the different aggregates is not available. So a solution for the coupled differential equations for

the binding kinetics has to be acquired. In the case of three monomers combining to three possible dimeres and a trimer, the equations are as follows:

$$\frac{dA}{dt} = -k_{on}^{A+B} \cdot A \cdot B - k_{on}^{A+C} \cdot A \cdot C - k_{on}^{BC+A} \cdot BC \cdot A + k_{off}^{AB} \cdot AB + k_{off}^{AC} \cdot AC + k_{off}^{BC+A} \cdot ABC$$

$$\frac{dB}{dt} = -k_{on}^{A+B} \cdot A \cdot B - k_{on}^{B+C} \cdot B \cdot C - k_{on}^{AC+B} \cdot AC \cdot B + k_{off}^{AB} \cdot AB + k_{off}^{BC} \cdot BC + k_{off}^{AC+B} \cdot ABC$$

$$\frac{dC}{dt} = -k_{on}^{A+C} \cdot A \cdot C - k_{on}^{B+C} \cdot B \cdot C - k_{on}^{AB+C} \cdot AB \cdot C + k_{off}^{AC} \cdot AC + k_{off}^{BC} \cdot BC + k_{off}^{AB+C} \cdot ABC$$

$$\begin{aligned}
\frac{dAB}{dt} &= -k_{on}^{AB+C} \cdot AB \cdot C - k_{off}^{AB} \cdot AB + k_{on}^{A+B} \cdot A \cdot B + k_{off}^{AB+C} \cdot ABC \\
\frac{dAC}{dt} &= -k_{on}^{AC+B} \cdot AC \cdot B - k_{off}^{AC} \cdot AC + k_{on}^{A+C} \cdot A \cdot C + k_{off}^{AC+B} \cdot ABC \\
\frac{dBC}{dt} &= -k_{on}^{BC+A} \cdot BC \cdot A - k_{off}^{BC} \cdot BC + k_{on}^{B+C} \cdot B \cdot C + k_{off}^{BC+A} \cdot ABC
\end{aligned}$$

$$\frac{dABC}{dt} = -(k_{off}^{AB+C} + k_{off}^{AC+B} + k_{off}^{BC+A}) \cdot ABC + k_{on}^{AB+C} \cdot AB \cdot C + k_{on}^{AC+B} \cdot AC \cdot B + k_{on}^{BC+A} \cdot BC \cdot A$$

Since these kinetic equations are used to find the steady state concentration distribution, only the ratio of k_{off} to k_{on} is relevant. After all, the value that should be recovered from the steady state condition is K_D. As long as the evaluation of the equation system yields the steady state concentration values, k_{off} can be set to K_D and k_{on} to one without losing generality. The steady-state values were recovered by minimizing the sum of the time derivatives. This approach was much more stable than using a ODE solver. During a fitting procedure kinetic rates would change unpredictably and adjusting the time steps for the worst case scenario was too calculation intensive. While renormalising of the model would have been possible, keeping the form of the equations presented here leaves the evaluation procedure more accessible to modifications later on.

The set of equations above describes the compete kinetics of the binding interactions of three partners. For the first experiments the complexity of the system was reduced by tailoring the binding partner interactions for all combinations of two monomers and all combinations of a monomer and a dimer to be as similar as possible.

In the symmetric case K_D^{A+B}, K_D^{A+C} and K_D^{B+C} are equal and can be written as $K_D^{mono \leftrightarrow dimer}$. The same way K_D^{AB+C}, K_D^{AC+B} and K_D^{BC+A} can be summed up as $K_D^{dimer \leftrightarrow trimer}$.

So the equation system for the symmetric binding of three partners with the k_{off} values replaced by the K_D values and the k_{on} values by one looks as follows:

$$\frac{dA}{dt} = -A \cdot B - A \cdot C - BC \cdot A + K_D^{mono \leftrightarrow dimer} \cdot (AB + AC) + \frac{1}{3} K_D^{dimer \leftrightarrow trimer} \cdot ABC$$

$$\frac{dB}{dt} = -A \cdot B - B \cdot C - AC \cdot B + K_D^{mono \leftrightarrow dimer} \cdot (BC + AB) + \frac{1}{3} K_D^{dimer \leftrightarrow trimer} \cdot ABC$$

$$\frac{dC}{dt} = -A \cdot C - B \cdot C - AB \cdot C + K_D^{mono \leftrightarrow dimer} \cdot (AC + BC) + \frac{1}{3} K_D^{dimer \leftrightarrow trimer} \cdot ABC$$

$$\frac{dAB}{dt} = -AB \cdot C - K_D^{mono \leftrightarrow dimer} \cdot AB + A \cdot B + \frac{1}{3} K_D^{dimer \leftrightarrow trimer} \cdot ABC$$

$$\frac{dBC}{dt} = -BC \cdot A - K_D^{mono \leftrightarrow dimer} \cdot BC + B \cdot C + \frac{1}{3} K_D^{dimer \leftrightarrow trimer} \cdot ABC$$

$$\frac{dAC}{dt} = -AC \cdot B - K_D^{mono \leftrightarrow dimer} \cdot AC + A \cdot C + \frac{1}{3} K_D^{dimer \leftrightarrow trimer} \cdot ABC$$

$$\frac{dABC}{dt} = -K_D^{dimer \leftrightarrow trimer} \cdot ABC + AB \cdot C + AC \cdot B + BC \cdot A$$

The trimers can fall apart into three combinations of a dimer and a monomer. In the symmetrical binding case each combination is equally probable, giving raise to the factor $\frac{1}{3}$.

Steady state concentrations based on these equations for the titration series shown in figure 2.9 are plotted in figure 2.5 (2).

To test the evaluation approach for a symmetric three partner interaction, the following was done: One K_D value was selected for the three interactions of monomers combining into a dimer and one additional K_D value was selected for joining of a dimer and a monomer into a trimer. In the general, asymmetric case, there are four K_D that define the binding interactions and the three Ce values of the system (see section 2.2.3 on page 41). In the case of the symmetrical binding system, all dimer-trimer K_Ds and Ce values are identical by definition. The two values were set to the value of $K_D^{mono \leftrightarrow dimer} = 500\mu M$ and $K_D^{dimer \leftrightarrow trimer}$ was set to $50\mu M$.

The positions where to probe the concentration cube, the set of all possible combinations of three concentrations, where chosen. This meant selecting a series of concentration conditions. For each sample of the series, the overall concentration of the three binding partners was given. For this, the three 16-step titration series used in the actual measurement (see section 2.4) were used. Applying the coupled differential equations to these values gave the steady state concentration for every accessible aggregate for each sample. So this yielded A, B, C, AB, AC, BC and ABC for every concentration cube triple $A_=$, B_0 and C_0 present in the concentration for the K_Ds used.

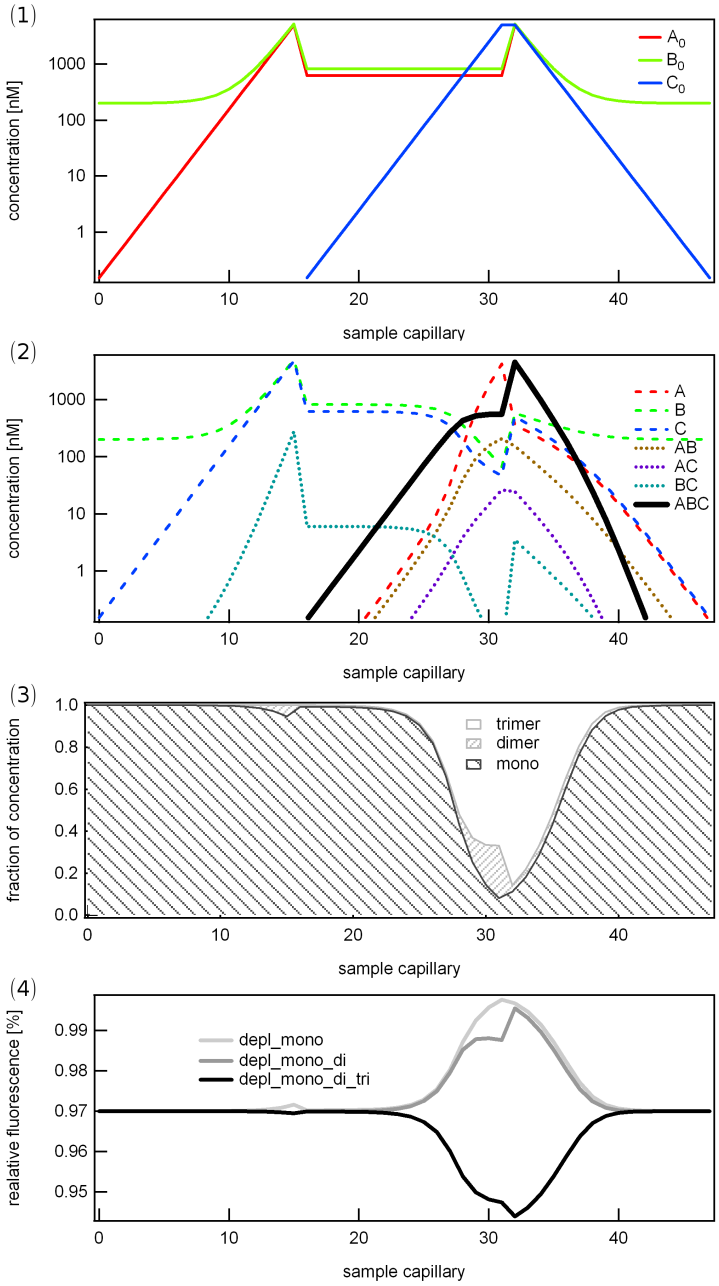

Figure 2.5: Depletion simulation scheme. (1) For every sample the total concentration of the oligonucleotiedes is defined. (2) Based on a set of binding constant K_D values, the resulting concentrations of monomers, dimers and trimers are derived. (3) From this the fraction of the labeled oligo resent as monomer, dimer and trimer is calculated. (4) The depletion values of the different binding aggregates are used to calculate the depletion expected for the measurement series based on the used parameters. In the fitting analysis the measured depletion is fitted to the results of this procedure.

An example of such a simulated data can be seen in figure 2.5 (2). By weighing every labeled aggregate with the appropriate thermophoretic depletion value, the mean depletion value was calculated. The depletion (reduced local relative concentration and fluorescence compared to unheated sample) of monomers was set to 94%, of dimers to 93% and of the trimer to 91%. In the general, asymmetric case there are four thermophoretic depletion values of interest. Only aggregates the incorporate the labeled binding partner are contributing to the depletion signals measured from fluorescence intensity changes.

Since the measured data will be subject to noise, the mean depletion data was multiplied by (1+noise-level), where noise level was chosen to be Gaussian noise with a standard deviation of 0.003.

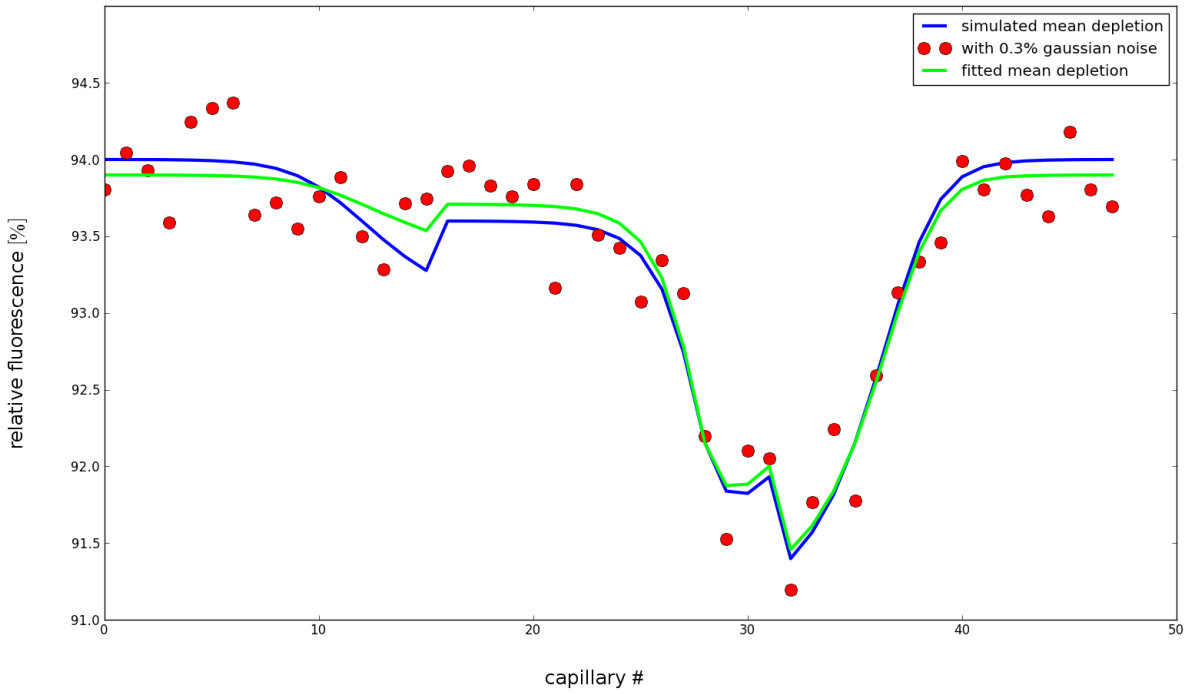

Figure 2.6: Simulated depletion values were treated with Gaussian noise and fitted with the proposed analysis procedure. The first 16 sample capillaries contain A and (B+B*) with successively doubling concentration. Sample capillaries 17-32 contain A and B at a stable concentration while C is titrated doubling the concentration from sample to sample. The samples on the right show a backwards titration curve halving the concentration with every step of all three samples.

The question at this point is whether the fitting procedure can extract the parameters used for the simulated mean depletion data. The noisy simulation data was used to test the evaluation procedure. The error used, though substantial in comparison to the signal, only represents statistical error, not systematic error. A study of the impact of systematic errors on the analysis would be a possible project for the future. As initial fit guesses $K_D^{mono \leftrightarrow dimer}$ was set to $1000nM$ and $K_D^{dimer \leftrightarrow trimer}$ was set to $1nM$. The initial depletion guesses where

95%, 92% and 90% for the monomeric, dimeric and trimeric thermophoretic depletion respectively. The depletion values for monomers and trimers can be roughly guessed from the strongest and weakest measured depletion values assuming bigger aggregates will lead to higher depletions (not always the case). The K_Ds are set on the edge of the range of values that the concentrations of the titration series can easily measure.

The fit to the noisy data can be seen as the green plot in figure 2.6. The fitted values were as follows: $K_D^{mono \leftrightarrow dimer}$: $579nM$ +/- $295nM$, $K_D^{dimer \leftrightarrow trimer}$ $34.5nM$ +/- $18.0nM$, monomer depletion: 93.90% +/- 0.06%, dimer depletion 93.39% +/- 0.185%, and trimer depletion: 91.11% +/- 0.220%. These fitted values agree well with the parameters used to simulate the data set. Even with the considerable amount of noise (see figure 2.6), cooperativity is measurable using the thermophoretic approach.

A more in depth investigation of the fitting landscape will be done later on based on data from an actual measurement.

2.3.5 Data evaluation

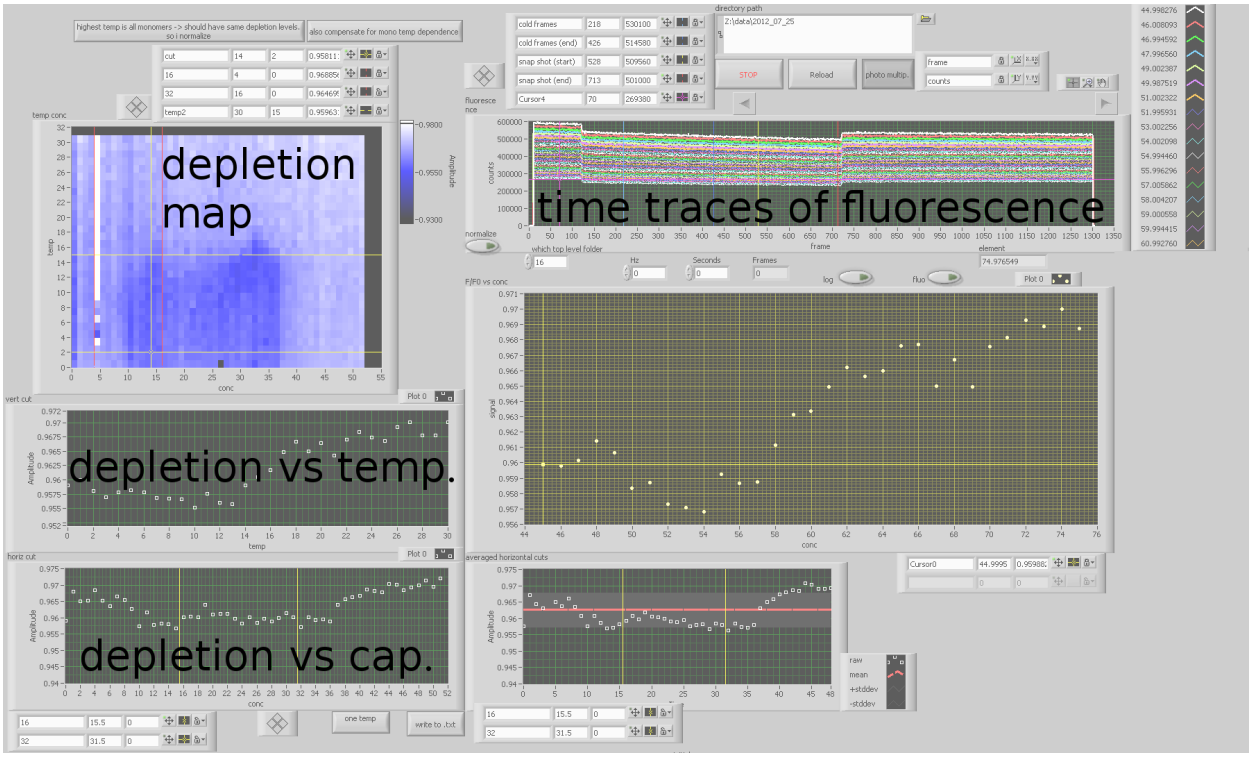

Figure 2.7: The LabView "*titration_series_analysis_movies*" (version $v13$) was used to interpret the photo-multiplier data of the depletion. It allows the selection of the time intervals for evaluating the sample depletion using the time traces. The created depletion map shows the sample fluorescence change for different temperature (vertical) and different sample preparations (horizontal).

The fluorescence data was measured as a series of count values the photo-multiplier recorded at 10 Hz. The raw data was interpreted with the LabView program "titration series analysis movies" (version $v13$) seen in figure 2.7. It reads in all time traces of the fluorescence data set. A number of aspects of the measurement can be investigated at this point.

Fluorescence time traces for each sample are interpreted to derive the depletion values. A depletion value is assessed for the response of fluorescence count by looking at the relative changes of the mean fluorescence from one time interval to another. If this value is not needed to derive S_T, the two intervals have little constraints and can be adjusted to result in low noise and high contrast amongst the depletion of the different samples. For the analysis shown here, the earlier interval ('cold frames') was chosen to range from frame 218 to frame 426, the later interval ('hot frames') from frame 528 to 713. Since the frame rate is 10 Hz and the laser is switched on 12.2 seconds after the frames start to be recorded, the relative fluorescence interpreted from here on is calculated as

$$\frac{\langle f \rangle_{9.6s-30.4s}}{\langle f \rangle_{40.6s-59.1s}} = 1 - depl.$$

Here *depl* is the mean depletion.

On the left side of the screenshot, the depletion pattern can be seen. The columns represent measurements of different binding partner concentrations as discussed in section 2.4. The columns represent the different temperatures at which the measurements were done. As discussed in section 2.1.2, the analysis will only be based on the measurements from one temperature, 59 °C in this case.

The data about the temperature dependence of the mean depletion can be used to measure melting curves thermophoretically [71]. The first 48 depletion values (the last four are repetitions the first four) for the symmetrically binding DNA construct at 59 °C was used for the analysis and can be seen in figure 2.17.

2.4 Measurements

Assuming, we could sample all the combinations of binding partner concentrations at an arbitrary resolution, these samples could be visualised as points in a cube with the axes A_0, B_0 and C_0 (in the case of three partner binding). Each point in this cube would have a steady-state depletion value attached to it. It is the premise of the presented approach that probing this depletion cube will allow the derivation of the binding interactions.

To cover the binding of the dimer, as well as the shifting from a mixture of dimer and monomer population to one with an additional trimer population and the binding of equally concentrated monomers (at high concentrations efficiently binding into trimers), a measurement design consisting of three concentration series based on titrations of one, two or three binding partners was chosen. These can be seen in the concentration cube in figure 2.8 and in the order they were measured and evaluated in figure 2.9.

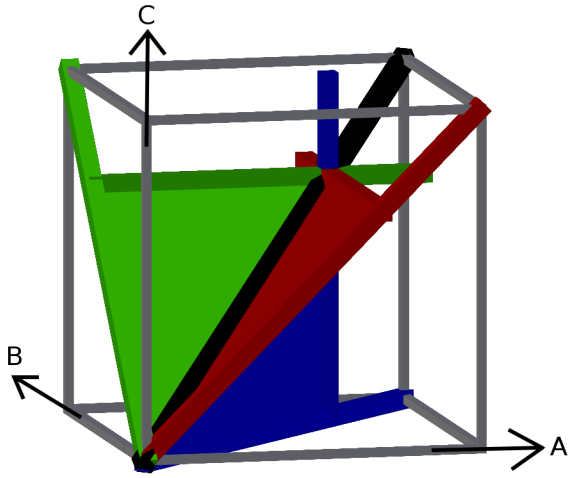

Figure 2.8: Measurement samples are located on the indicated path within the *concentration cube*. A set of three titration series each outlines one of the triangles. One "wall measurement" with one binding partner completely missing, one "cross-beam measurement" with two of the concentrations fixed while the remaining being titrated and the "space-diagonal measurement" ($A_0 = B_0 = C_0$) makes up one measurement.

Although it might be argued that the information gain about the cooperativity per sample (individual measurement based on a monomer concentration combination) could be improved if the samples are distributed in the three dimensional concentration cube unrestrained by preparation, sticking with titration series for their error resilience was a trade-off chosen for the experiments presented here.

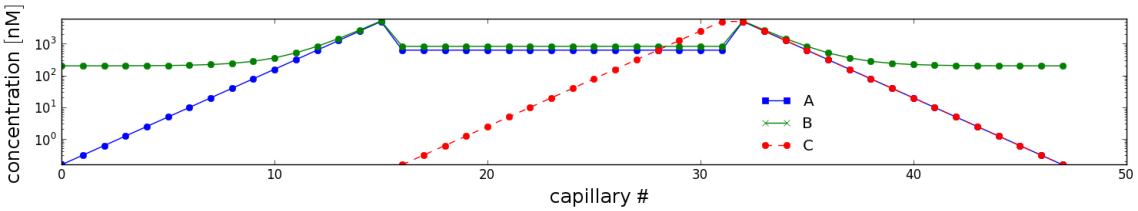

Figure 2.9: Concatenated, the three measurement paths cover different combinations of the binding partners. The fixed contribution of the labeled B* subspecies is included in the concentration of B.

Titration series can be pipetted in a fashion that keeps concentration errors at a minimum (see B.3).

Throughout all the cooperativity measurements, the concentration of the labeled monomer was kept constant. This concentration was set to $200nM$ in the presented experiments. To ensure this, the highly concentrated titration sample and the buffer for the stepwise solution each had the same concentration of labeled monomer. This way, throughout the

whole titration series, only liquids with the same concentration of the labeled monomer were mixed together.

2.4.1 Depletion measurement

The thermophoresis measurement in a solution with a certain set of concentrations of the binding partners yields the averaged depletion of the binding aggregates weighted by their steady-state concentrations. If too many different aggregates differ so little in their respective thermophoretic depletion that they can't be reliably told apart, the conditions (temperature, buffer composition) have to be adjusted until there is a signal significant enough to interpret.

A standard concentration measurement involves preparing the sample solutions. For the measurement our DNA constructs consisted of three sets of titration series going from $5\mu M$ down to $0.153nM$ in 16 concentration-halving steps. The *wall measurement* only included two monomers of the same concentration. The *space diagonal measurement* consisted of equal concentration for all three binding partners. For the *cross-beam measurement* the final partner was titrated to a static, intermediate concentration of two partners, at which — without the third partner — a good part, but not all of the monomers were bound in dimer aggregates. This static concentration was $625mM$ for the data analysed here (see figure 2.9). On the left there is the *wall measurement*, the cross-*beam measurement* is in the middle and the 16 steps on the right account for the *space diagonal measurement*.

If the sample which is available with a labeled version is B, this allows for the *wall measurement* to cover the combined titration of A and B or of B and C. Conversely, the *cross-beam measurement* was prepared with A at the fixed concentration as well as C. Meeting at the *space diagonal measurement*, these two options outline two *measurement triangles* in the concentration cube.

We measured the fluorescence signal of all capillaries starting at 45 °C up to 75 °C in increments of 1 °C. To derive the information about the binding, only measurements at a fixed temperature were used. These measurements were conducted to infer the presence of stability of the aggregates dominant in different samples and might be used in future evaluations.

Depletion measurements are presented in figure 2.10. These are of the binding partner combination A16-17, B20-20 / B+20-20 (labeled) and C17-16. The numbers indicate the binding motices towards the 3'-end and the 5'-end. The dark regions of higher depletion signify a strong dimer fraction in the left half of the depletion maps in figure 2.10. The more pronounced dark region between the middle and the third on the right are probably due to a large trimer fraction. The red lines indicate the borders between the three titration series. The concentrations for every sample can be seen in figure 2.9.

The measurements in the top and bottom row differ in salt concentration. The upper two were measured at a concentration of $200mM$ NaCl, while the lower was measured at $300mM$. The depletion maps on the left and right are the two accessible *measurement triangles* discussed above. The left measurements always contains the same concentration

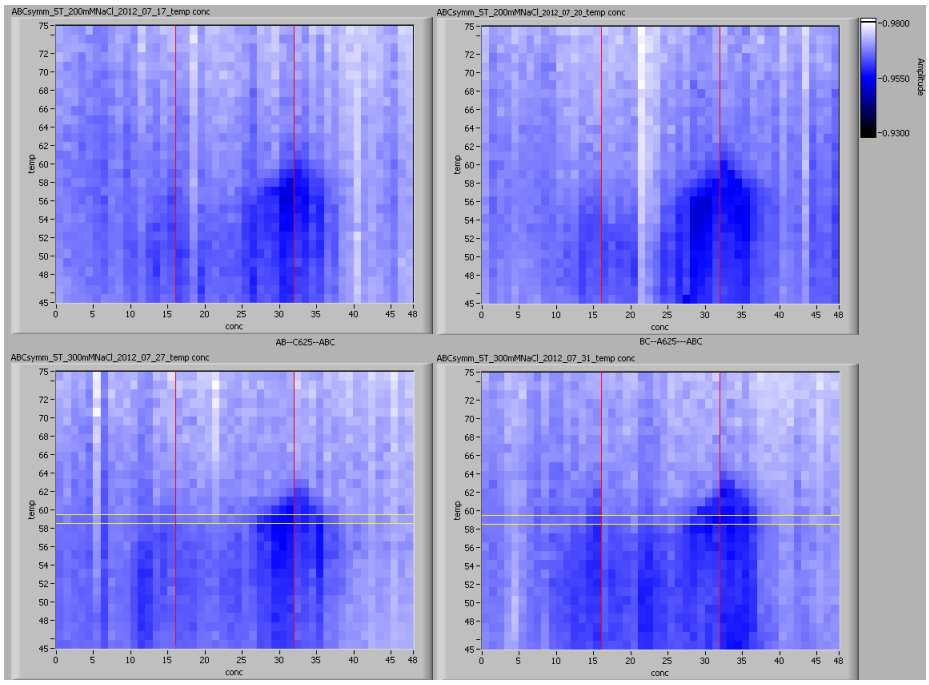

Figure 2.10: Depletion maps show the relative change of fluorescence across the measured sample preparation and temperatures. The red lines indicate the borders between titration series. The leftmost part shows increase in concentration of molecule A and B on the left side and molecules B and C in the measurements on the right side. The middle part has the aforementioned concentrations fixed at $625nM$ and the remaining binding partner is titrated in the same fashion. The remaining 16 samples cover the reduce of the concentration of all unlabeled samples alike. B^* is at a fixed concentration of $200nM$ for all samples.

of A as B (without the labeled fraction) and in the right the concentration of B and C are equal.

The temperature and concentration dependence of oligonucleotide binding can be observed in the arrow-like shape of the border of the strongest depletion region. The closer the samples are to the red line on the right, the higher is the concentration. With growing concentration the aggregates are stable up to higher concentrations.

In a series of 48 samples some show stronger or weaker depletion levels for all temperatures. Depletion signal changes with temperature are often a sign of sample evaporation. A lot or work was put into reducing such artefacts. However, measurement quality still needs improvements. Some artefact still remain, such as the fact that the first and the last capillaries do not always show the same fluorescence levels, despite presenting almost exclusively depletion of monomers.

The observable, increasing depletion for temperatures below the melting temperatures of aggregates is a result of the temperature-dependence of thermophoresis. As evident from the two salt concentrations shown here, the impact on the thermophoresis is sec-

ondary to the effect on binding of dimers. At $200nM$ and $300nM$ the ionic component of thermophoresis is dominated by the non-ionic component.

The signal of the dimers on the right edge of the left titration series are clearly weaker for $200mM$ NaCl than for $300mM$. Therefore, a temperature in this data set was selected that showed high changes in depletion strength. Here, 59 °C was selected, indicated by yellow lines in figure 2.10.

2.5 Results

To collect information about the sample interaction of the oligonucleotides (including variants of different lenght), melting curves and gel electrophoresis measurements were done.

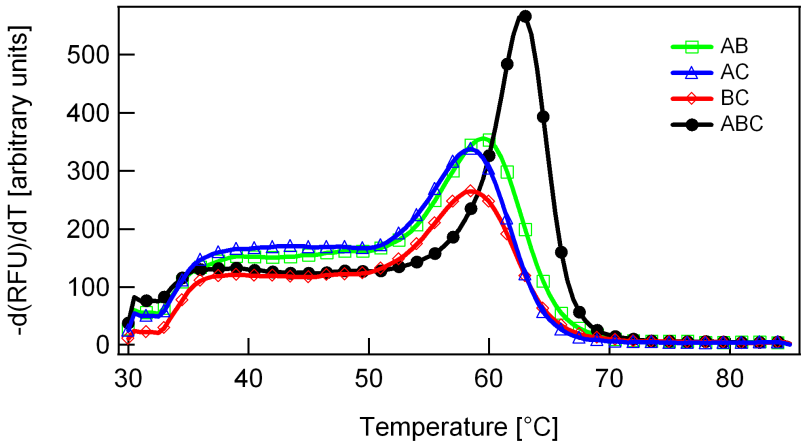

Figure 2.11: Melting curves of the used binding partners. The dimers melt at almost the same temperature. The trimer is more stable as expected. The intercalating dye used for this measurement stabilises the binding to a degree. This measurement was used to preselect a binding partner combination with roughly the same affinity for all possible dimers.

Using melting curve analysis in a RT-PCR machine (BioRad, combination of CFX96 and C1000 using the SYBR/FAM detection channel), we selected a combination of binding partners with very similar dimer melting behaviour (see figure 2.11). Additionally, the difference of melting temperatures between the dimers and the trimer was of interest. While the intercalating dye (Sybr Green I, Invitrogen) used as an indicator of fraction bound (being intercalated in a base pair scaffold strongly increases the fluorescence of the dye), is known to stabilise the binding and shift melting temperatures, the relative difference of melting temperatures—or, more aptly, the absence thereof— was of interest and could be interpreted as a rough indicator for the relative binding strengths.

To be sure that combining into a three partner aggregate was in fact an energetically favoured state, we looked at high concentration mixtures of the binding partners using gel

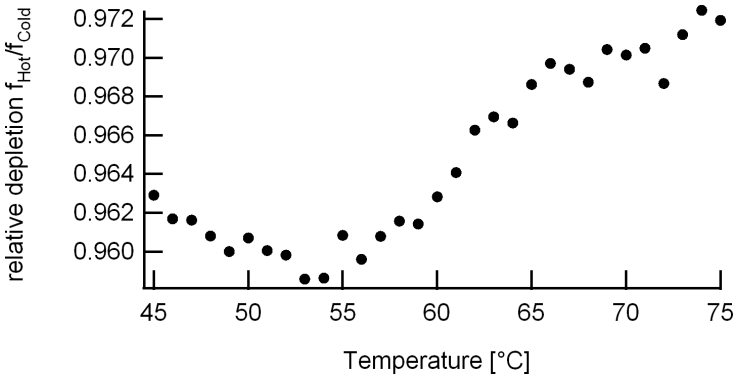

Figure 2.12: The dimer fraction of a sample containing $2.5\mu M$ A and $2.7\mu M$ B (including $0.2\mu M$ B*) dissociates into monomers as the temperature is increased. The shown thermophoretic depletion itself is temperature dependent.

electrophoresis (see figure 2.13). The different monomers are chosen for symmetry in their binding behaviour, not their length, so the dimers are not expected to progress through the gel at the same same speed. This evaluation showed us that the dimers and trimers actually bind as expected. Furthermore a faint band corresponding to what probably is a closed loop of six subunits (ABCABC in a cycle) can be seen. This contribution is small however and was not considered in the model underlying the evaluation routine (see section 2.3.4).

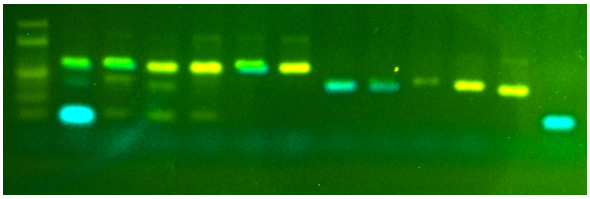

Figure 2.13: Gel of DNA aggregates. The information of the intercalating SybrGreenI channel (yellow) and the Cy5 channel for the labeled molecules B* (green) are combined. The first band shows a double stranded DNA ladder of 150, 100, 50,30(weak),20 and 10 base pairs for reference. The next six bands contain all three binding parter with variations in concentration and B variant (labeled or unlabeled): Band2: A B* (5× concentration) C, Band3: A B* C (5×), Band4: A B (5× concentration) C, Band5: A B* C (5×), Band6: A B* C, Band7: A B* C. Bands 8-12 have two binding partners: Band8: B*C, Band9: A B*, Band10: A C, Band11: B C, Band12: A B. Band12: monomer B*. Standard DNA concentration is $200nM$. Aggregates were stained 0.5× SybrGreenI.

Automatic fitting gives access to the optimal fitting parameters by probing the parameter space. The fitting routine can be interpreted as a process to find a local minimum of the fitting landscape. In this picture, the lower a point on the fitting landscape is, the smaller is the difference between the measured values and the calculated value for that point based on the fitting parameters defining that very point. If this landscape is smooth

enough, there is a good chance for a fitting procedure to find the global minimum. If the landscape is dented in a lot of places, many initial fitting parameters will result in the procedure only finding a local, and not the global minimum. In fact, the measurements at hand are not smooth enough to converge reliably. To investigate the fitting landscape and find the global minimum, the fitting procedure was primed 1000 times with randomised initial conditions. The values for the depletion values were randomly chosen between 0.8 times the smallest depletion value found in the measurement and 1.5 times the biggest one. Since $K_D = exp^{\frac{\Delta G}{k_B T}}$, and K_D values much below 0.15 nM and above $5\mu M$ cannot be measured reliably with the concentrations used here, values for $K_D^{mono \leftrightarrow dimer}$ and $K_D^{dimer \leftrightarrow trimer}$ were drawn using $exp(random(log(0.15nM)...log(5\mu M)))$.

The 1000 fits can be compared based on their χ^2 values. This value gives the goodness of the fit by summing the squares of the differences between measurement value and simulated value. The smaller χ^2, the closer the agreement between the model primed with the final fit parameters and the measurement. In a noisy data set, χ^2 will not reach zero. If it ever does, it is a clear sign that the model has more degrees of freedom than appropriate for the system at hand and parameters are reproducing the noise of the measurement in addition to the properties of the overall system. The histogram (figure 2.14) shows that a seizable fraction (25%) of the fits converged close to a lower bound for the goodness of fit χ^2.

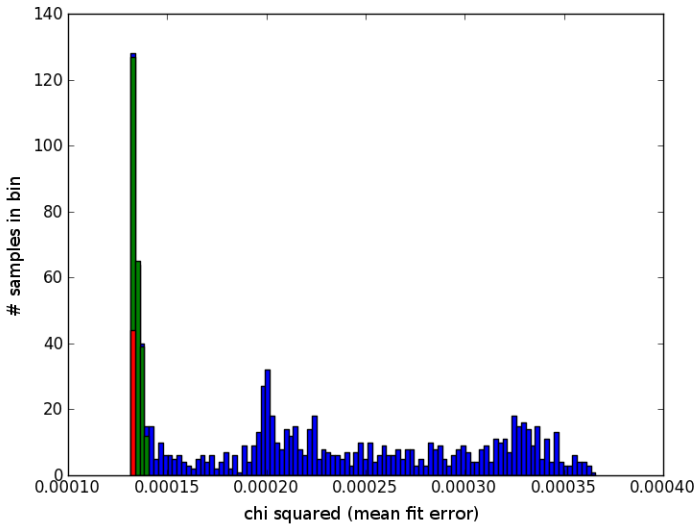

Figure 2.14: Histogram of goodness of fit χ^2 for 1000 randomly primed fits. Roughly 25 percent approach the lower bound (green fraction). The best 5 percent are colored in red. The fitting landscape is not smooth enough to ensure that all reasonable initial fitting conditions propagate to the global minimum. Selecting for the successful fits like this yields the parameters seen in figures 2.15 and 2.16.

The fitted binding constants $K_D^{mono \leftrightarrow dimer}$ and $K_D^{dimer \leftrightarrow trimer}$ as well as the depletion values for monomers $depl_m$, dimers $depl_d$ and trimers $depl_t$ can now be interpreted, as

seen in figure 2.15 and for the measurement series starting with the titration of A and B, and in figure 2.16 for the measurement series starting with the titration of B and C, see section 2.4.

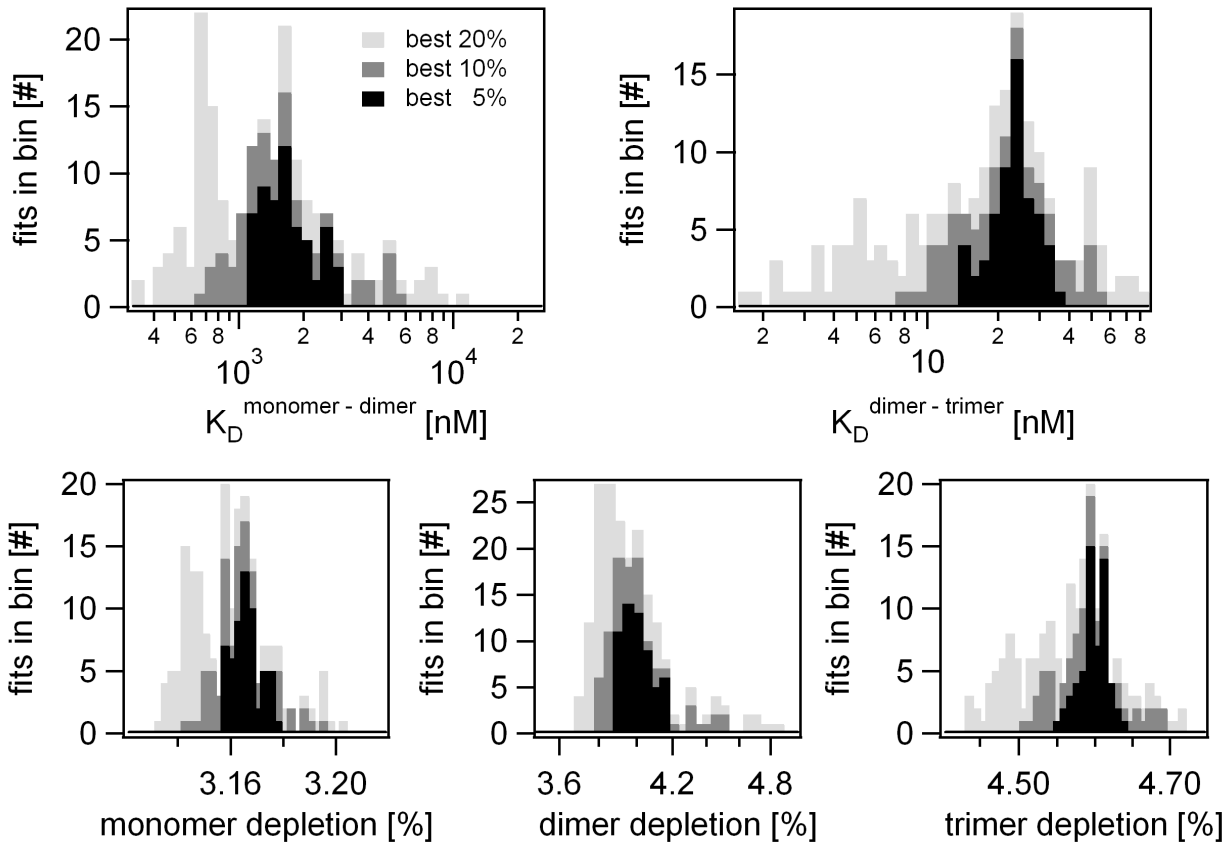

Figure 2.15: The 1000 randomly initiated fitting procedures of the measurement series covering the AB side of the concentration cube yields K_D and depetion values for cut-offs of the 5, 10 and 20% of fits with the lowest χ^2 error.

The incrementally better fractions of the fits are contained within each other for all parameters as seen in figures 2.15 and 2.16. Because of this, the fit landscape seems to have a meaningful global minimum. In figure 2.17, the best 5% of fits for the measurement series starting with the titration of B and C are shown; they show very little difference. One of the problems of these measurements is that $K_D^{mono \leftrightarrow dimer}$ is high for the used concentration ranges. With all of the best fitted $K_D^{mono \leftrightarrow dimer} > 3\mu M$ in 2.16, higher concentrations than $5\mu M$ have to be used to investigate this value and, as a result, improve the precision with which depletion $depl_d$ can be pinned down. Yet, this is not really a shortcoming of the presented procedure, but getting all the relevant concentration ranges covered with measurements could mean that more and differently distributed measurements of binding partner concentration combinations have to be collected.

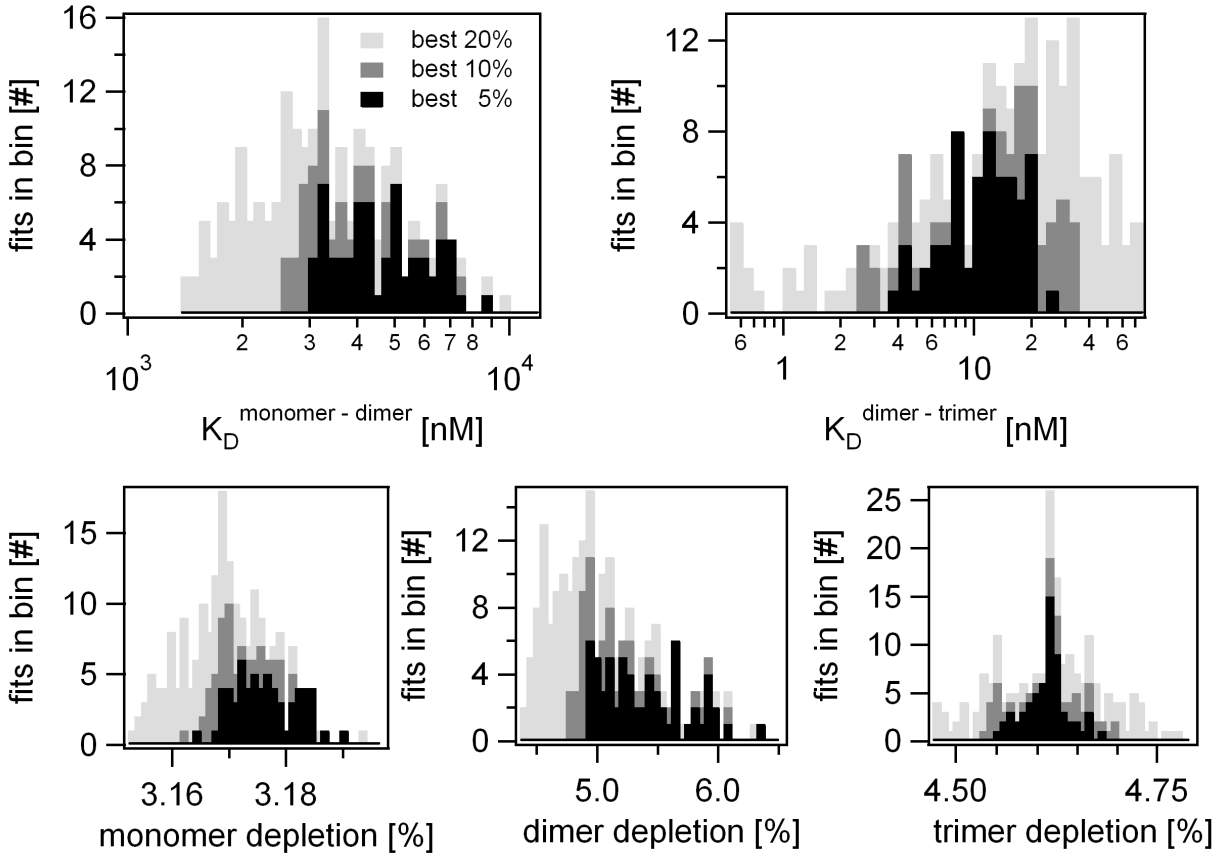

Figure 2.16: The 1000 randomly initiated fitting procedures of the measurement series covering the BC side of the concentration cube yields K_D and depetion values for cut-offs of the 5, 10 and 20% of fits with the lowest χ^2 error.

For the fit with the lowest χ^2 (0.00013138) in the set (see 2.16), the fit parameters were as follows:
$K_D^{mono \leftrightarrow dimer}$: 5535 +/- 2381 nM
$K_D^{mono \leftrightarrow dimer}$: 19.97 +/- 9.24 nM
$depl_m$: 3.18 +/- 0.038 %
$depl_d$: 5.57 +/- 0.65%
$depl_t$: 4.61 +/- 0.11%

This means that with implied symmetric binding of the three DNA parts we derive a cooperative effect $Ce = 277.2$ +/- 175.5, which corresponds to a $\Delta(\Delta G) = 2.58 \cdot 10^{-20} + / - 2.37 \cdot 10^{-20} J$

The error of a single fit remains considerable, even for the fit with the lowest χ^2 value, with the distributions of parameters for fits finding the global minimum seen in figures 2.15 and 2.16 complementary data.

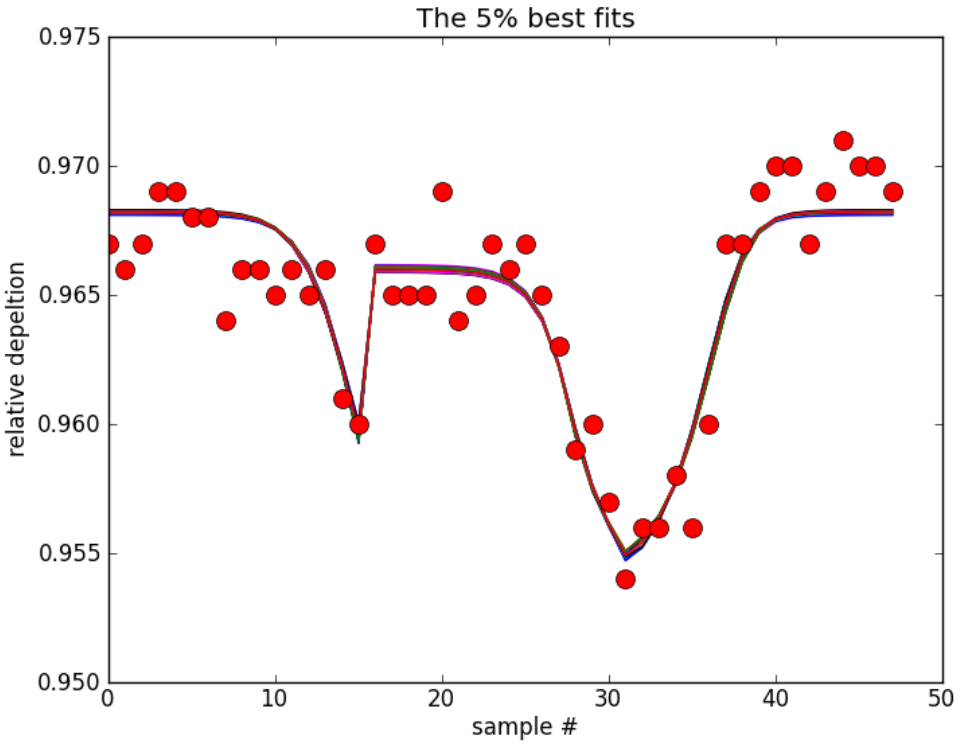

Figure 2.17: Measured depletion data evaluated assuming symmetrical binding of the measurement including the BC titration. The best 5% of randomly primed fits are shown here. While the agreement among the depletion predictions is strong, the values for the saturated

The presented measurements can be improved by tailoring the concentrations covered in the measurement better to all the binding constants involved. Clearly, the fact that the measurement does not reach a condition in which the dimer concentration is saturated, results in an uncertainty in $depl_d$ and by implication in $K_D^{mono \leftrightarrow dimer}$ and to a degree the whole fit which can be reduced.

It remains to be seen, how big the influence of systematic errors are on these results.

The resulting cooperative effect Ce values are stronger than those for binding of viologens and pyrdines to a synthetic bivalent porphyrin receptor measured in [11]. This is not surprising, since the oligonucleotide samples were specifically designed to show strong cooperativity.

2.6 Conclusion

The measurement of cooperativity based on thermophoretic depletion of just one observable binding partner is possible. The example presented in this work relies on a structure chosen

for symmetrical binding. So instead of eight free parameters of the fit analysis approach, only five where needed here. Moreover, this analysis relied only on a very limited set of possible depletion measurements. While 48 capillaries are a step up from standard thermophoresis analysis assays [72], employment of pipetting robots and thermophoretic measurements in multi-well-plates would make it possible to probe a lot more positions within the concentration cube.

In contrast to the prevailing approach to cooperativity measurements [11], this measurement specifically does not need a *receptor* to be fully occupied. It opens up the investigation of systems in which all partners bind amongst each other.

Improvements of the measurement setup, sample preparation and data pre-processing should lead to measurement of the complete binding constant and cooperative effect properties of a three partner binding system with below 100 samples. To be an actual tool for the analysis of biomolecules, the employment of high throughput thermophoresis measurements is required.

In this work a proof of principle for the measurement of cooperativity using the thermophoresis of just one labeled partner was successfully demonstrated, which has been specifically pointed out as having been missing so far [11].

2.7 Outlook

Automatic sample preparation with pipetting robots and very high throughput thermophoretic measurements is where the presented cooperativity measurement really starts to be promising for hitherto unmeasurable interactions of more complex systems. The measurement of thermophoresis directly inside multi-well plates holding hundreds or thousands of samples is under active research at the lab of Prof. Braun. Research into improving preparation and measurement procedures is in progress here as well. Pipetting robots can be very economical regarding samples. Although the 5 cm long capillaries with a rectangular cross-section measuring $50\mu m$ by $500\mu m$ only uses $1.25\mu l$ of sample, minimising consumption is of the essence, especially for analysing interactions of more than three partners using rare or hard to obtain binding partners.

The next step would be to investigate the asymmetric binding of variations of the samples shown here. Different lengths for the three binding regions would show strongly different properties. For this the analysis procedure has to fit four of the six K_D values determining the interactions and the four depletion values the labeled binding partner is part of. This will likely require to increase the amount of measured data points considerably, even if more measurement artefacts can be removed. The concentration ranges covered would have to be widened considerably to cover a broader range and improve fitting.

Investigation of a model system in which dimer and trimer interactions are tunable independently of each other are also of interest. While sterical penalties or strand displacements could be considered, the model currently envisioned would be a DNA trimer that binds in a circular fashion. Since there is no way to have a DNA circle out of three pieces due to the directionality of the backbone, a cross-linker that joins 3'-end to 3'-end or

5'-end to 5'-end would be necessary, creating a sort of *Janus-DNA*. The persistence length of DNA would reduce the efficiency of circulariasation depending on the presence and size of flexible non-binding regions. It would be possible to adjust trimer binding constants largely without influencing the dimer binding constants.

Soon, a switch to protein samples should be considered. Here this approach could be used to measure the complete binding interaction in a wide range of complex protein interactions and further the understanding of interactions in pharmaceutical research.

Appendix A

Assorted projects

A short overview is given on experiments leading up to the topics covered in the main chapters.

A.1 Limits of linear thermophoresis

The experiments presented in chapter 1 and 2 show thermophoretic effects with gradients well under $0.1K/\mu m$. They are far from the limit, where a linear response theory fails to describe thermophoresis. The premise is that for gradients so high that temperature changes significantly over the size of the particle, thermophoresis changes. It can no longer be described as a particle diffusively exploring its surroundings and being biased due to the energetics involved in diffusing into a hot or a cold region. At high temperature gradients thermophoresis trajectories change from being a 'downhill tumble' and start resembling ballistic trajectories.

The Peclet number Pe of a system indicated if hydrodynamic or diffusive effects dominate the motion of the particle

$$P_e = a\frac{v}{D} = a\frac{D_T}{D}\nabla T = aS_T\nabla T$$

Where a is the particle radius, v its drift velocity, D the diffusion coefficient, D_T the thermophoretic mobility, S_T the Soret coefficient and ∇T the temperature gradient.

Typical measurement setups have temperature gradients that are much lower than 1 for micro-scale particles. In these the motion of the particles is diffusive in nature. Only when reaching $P_e \gg 1$ will the hydrodynamic flows around the particle start to designate the particles trajectories.

The minute size of the measurement areas used in our lab make it possible to reach very high temperature gradients. Even measurement chambers on the millimetre scale using external heating can hardly reach a gradient of $10^6 K/m$.

A gradient over height of a $20\mu m$ capillary could reach high values without the necessity of special solvents. For water a gradient from 0 °C on the top of the capillary to 100 °C

on the bottom of the capillary would mean $5 \cdot 10^6 K/m$. To have the sample heated from the bottom and not in volume by absorption in water (as done in the first two chapters), experiments were done with capillaries that were covered on one side with chromium. To produce these cleaned capillaries were coated with a $200nm$ layer of chromium. On its own, the chromium layer was fragile and the laser would burn holes into them. After sealing the chromium layer with $60nm$ of SiO_2, they became very resilient. The absorption length $(1/e)$ for the laser used for these experiments (RLD-5-1455, IPG) in chromium is $36.7nm$. So basically all (99.5%) of the laser intensity is absorbed in the chromium layer. The high thermal conductivity of the chromium would spread the temperature distribution much wider than the laser beam width. The capillary would be glued to a sapphire cover slip. This allowed imaging through the sapphire while granting good thermal conductivity $(32W/mK)$. The sapphire was in thermal contact with four Peltier elements cooled to temperature just high enough, to not freeze the sample.

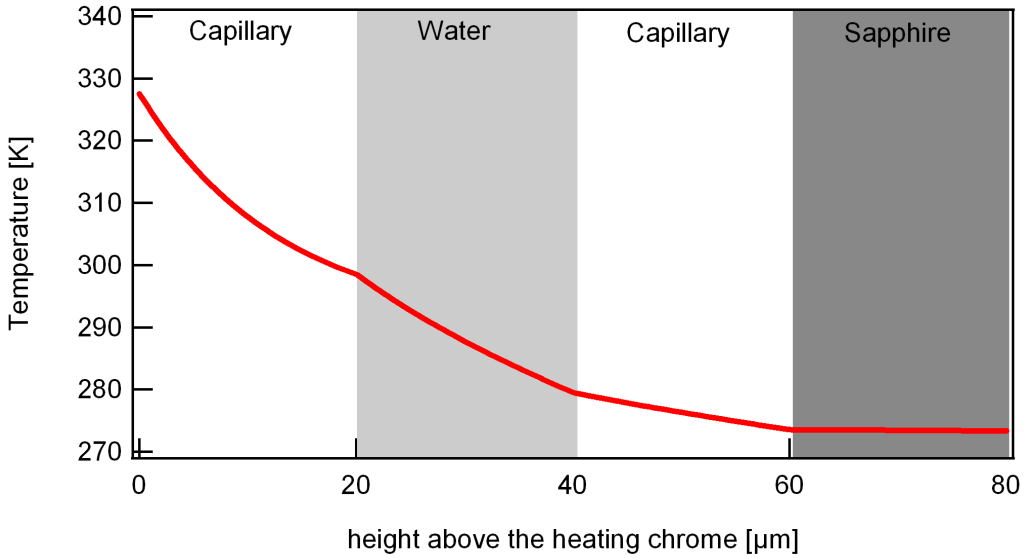

Figure A.1: Temperature decay above the laser center of a chrome coated capillary. The temperature gradient is nearly linear in the water.

The assessment of the temperature distribution in the direction of the optical path was problematic. While it was easy to determine the temperature of the liquid volume averaged over the height of the chamber with temperature-dependent fluorescent dyes, this by itself does not yield the temperature gradient. Simulations using FEMlab showed (see figure A.1) that temperature change throughout the liquid layer inside the capillary is very linear. The same goes for the walls of the borosilicate capillary. A main problem was the uncertainty, which temperature the sapphire would have where it connected to the capillary. Even worse was the fact that the quality of the thermal contact between sapphire and the uncoated side of the capillary (which was flat only in the first approximation). One idea was determining the temperature gradient by calculating the speed of

sedimentary particles thermophoretically driven to the top of the capillary. Given a known Soret coefficient, this would yield the temperature gradient. For really high temperature gradients, thermophoresis is expected to change. So this approach would not have been the solution for the gradients, this setup was supposed to make possible.

The approach outlined here did not progress to a point, where the temperature gradient could be evaluated with enough certainty to base further evaluation of the limits of the thermophoretic effect on it. Therefore a specialised setup for this topic was bulid and the investigation of high temperature gradients using chromium layer is still investigated at the group of Professor Braun.

A.2 Accumulation close to surfaces

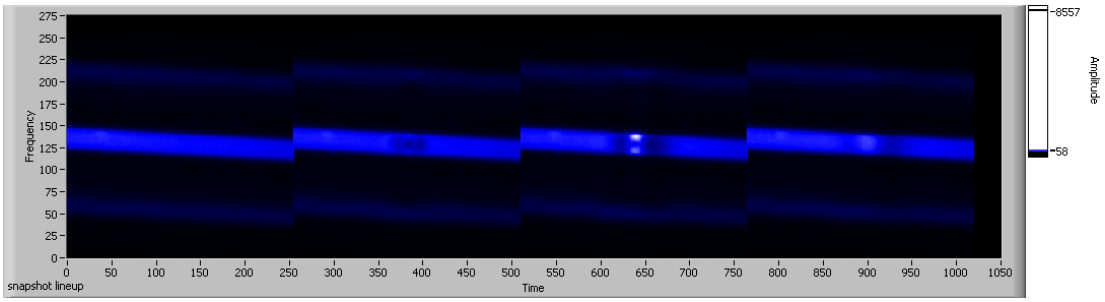

Figure A.2: Depletion and accumulation pattern observed in a $50 \times 50 \mu m$ capillary shows accumulation close to the wall. The observed pattern can be explained by the interplay of convection and thermophoresis. Seen here are snapshots before the laser was used, 9 and 58 seconds after laser heating was activated and 28 seconds after the laser was switched off.

While the micro-scale thermophoresis measurements used in our group has many advantages, a possible contribution to thermophoresis given raise from surface effects would impact this measurement method a lot due to the high surface to volume ratio. A number of researchers in the field of thermophoresis have started considering contributions from thermophoretically induced electrophoresis [41, 40]. The central idea is that the thermophoresis of ions results in charge separation towards surfaces in electrolytes. When heating the capillary in volume by infra-red laser absorption in water, the heat distribution is cylindrical in first approximation. While there would be a temperature gradient towards the glass wall of the capillary, it is minute in comparison to the radial temperature gradients responsible for the regions with strongest thermophoretic effects in the broad capillaries used in chapters 1 and 2. Since the relative fluorescence change is averaged over the height of the chamber in this geometry, deviations from effects close to the surface would not have a strong effect on the measurement, as long as the walls of the measurement chamber are far enough away from the region of strong temperature gradients. A different approach to thermoelectrophoresis assumes a different temperature for the colloid and thus

a temperature gradient around the particle that would lead to a temperature gradient surrounding the particle. This gradient could then in turn lead to accumulation or depletion of ions close to the particle surface due to different solvation energies for different ions, resulting in an electrical field. While this is a phenomenon possibly of interest for example for directly heated gold particles, the samples in our experiments are not likely to have a different temperature than its surroundings.

In contrast to a number of recent theoretical [41, 40, 73] and experimental works [64], electrical fields induced by the temperature gradient appear not to be relevant in the measurements discussed in chapter 1. For example, in the pH range of constant DNA charge (pH 5 - 9) the measured Soret coefficient is constant and shows no dependence on OH- concentration (supplementary material). The buffer TRIS keeps the pH value between 8.4 (5 °C) and 6.5 (75 °C) [18, 63] and the oligonucleotide charge should not change between the two relevant pKa values of nucleotides above 4.3 or below 8.7 [9]. The pKa value of the 6-Hex label is ∼3 [24]. As seen, outside this pH range, the thermophoretic depletion drops considerbly, expected from the dropped nucleotide charge as the pH passes the pKa values. Both the buffering of TRIS and the capillary glass walls are expected to keep thermally accumulated OH- ions from locally offsetting the pH. The electrophoretic mobility of nucleotides is well known [60, 59, 61] with a predominantly length independent characteristic and growing only slightly for reduced salt concentrations. These dependences does not allow to account for the measured Soret coefficients quantitatively.

Experiments were conducted to see if polystyrene beads (FluoSpheres F8888, Molecular Probes) or labeled oligonucleotides would accumulate close to the walls of a rectangular $50\mu m \times 50\mu m$. For these experiments a number of particle sizes and buffer conditions were used.

While some showed accumulation of particles close to the wall of the capillary, this could always be explained as a combination of convective and thermophoretic effects and were reproducible with FEMlab simulations. No conditions were found where the convection and thermophoresis on their own without thermophoretically driven electrophoresis could not explain the behaviour shown in experiments.

A.3 Thermophoresis shows negligible dependence on pH

Measurements were conducted to exclude significant thermoelectrophoresis effects in our measurements. Soret coefficient S_T measured for buffered and unbuffered solutions at various pH values are presented in table A.1. Between pH 4 and 11 the changed buffer pH changes the Soret coefficient less than 10%, well within the error margins of the measurement and not enough to consider the thermophoresis of OH^- ions to be a major contributor to an electrically driven thermophoresis. Measurements were performed at 25 °C and under the presence of 10mM KCl.

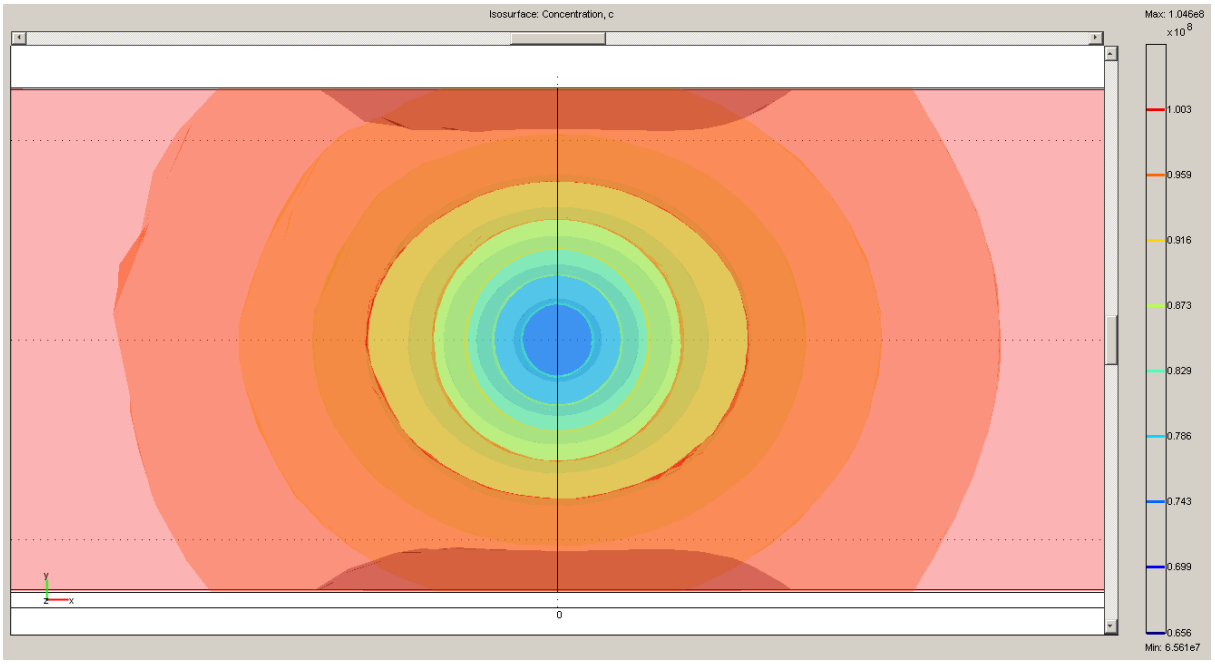

Figure A.3: Femlab simulation of a $50 \times 50 \mu m$ capillary shows accumulation close to the wall..

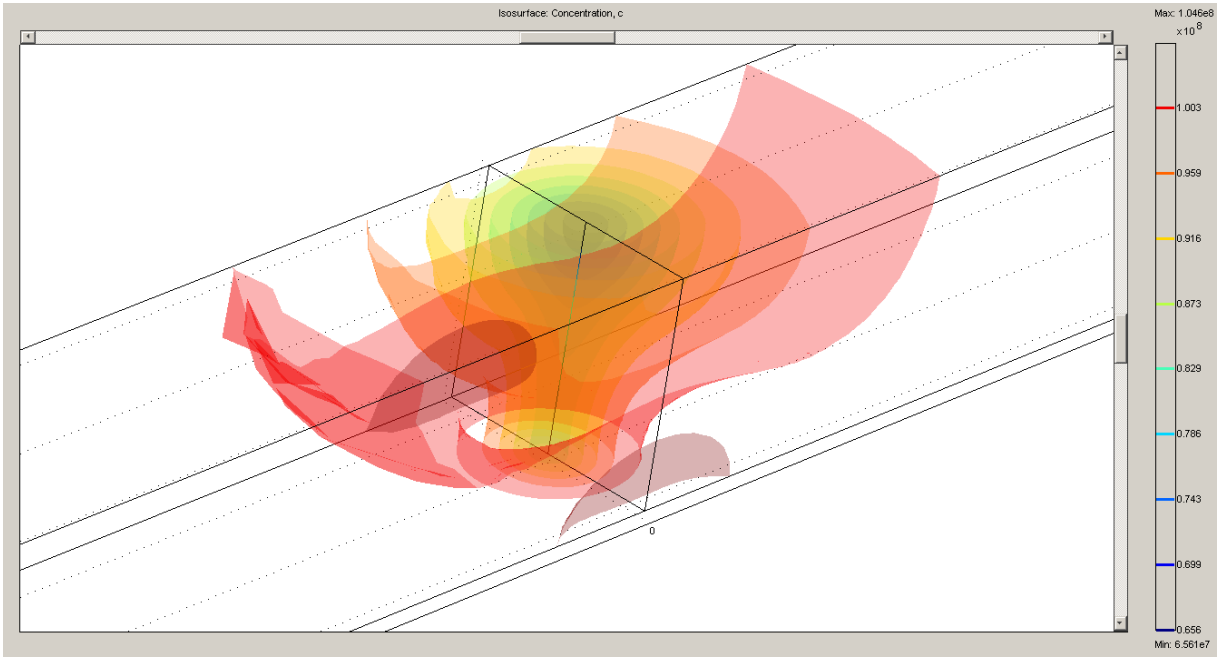

Figure A.4: Femlab simulation of a $50 \times 50 \mu m$ capillary shows accumulation close to the wall. From this angle it becomes obvious that the accumulation is in the bottom corner of the capillary.

Soret Coefficient S_T [1/K]	pH	Buffer
-0.0270	13	no buffer
-0.0070	12	no buffer
0.0530	11	no buffer
0.0530	10	no buffer
0.0661	4	no buffer
0.0470	3	no buffer
-0.0081	13	1mM TRIS
-0.0051	12	1mM TRIS
0.0810	11	1mM TRIS
0.0781	10	1mM TRIS
0.0811	7	1mM TRIS
0.0851	4	1mM TRIS
0.0431	3	1mM TRIS

Table A.1: S_T of DNA samples is stable in the region of physiological pH values in buffered as well as unbuffered solution.

Appendix B

Experimental details

In this part additional details regarding the experiments not covered in the the main chapters are recorded.

B.1 Measurement setup

For the measurement in chapter 1 the LED was driven at $30mA$ and the infra-red laser (Fibotec, $\lambda = 1480nm$) with a control current of $0.7V$, resulting in a typical emission power $28mW$.

The Peltier elements controling the temperature the experiments in both chapters were able to heat and cool the sample stage. A relay allowed to switch polarity of the current through the Peltier element. A temperature sensor was glued to the sample side of the Peltier element. In the measurements for chapter 1 no PID control was used. Instead a lookup table provided the current settings for different temperatures. Although this reduced flexibility, the temperature control worked very predictably. The realised temperature values were recorded every second and could be reviewed during and after the measurement. Fluctuations of the water bath keeping the side of the Peltier element facing away from the samples at a stable temperature were never encountered. But such fluctuations could be counteracted with a temperature control employing a PID control, so it was used in the measurements for chapter 2.

The silicon waver used as the sample stage provided a very flat surface with good heat conduction and negligible fluorescence background. Prior to every measurement the waver was cleaned with a isopropanol dampened lint-free wipe.

To automate the measurement in several capillaries, the samples were moved through the field of view of the camera (or photomultiplier) by the translation stage. A fluorescence profile covering all sample capillaries can then be used to determine the approximate stage position to image the center of the capillaries using a simple threshold approach.

To measure the dark count of the CCD camera, an exposure with the same settings as the actual measurement with a blocked light path was collected. For the Andor Luca

the dark count values were stable and homogeneous. So it sufficed to reduce the counts of every pixel by the calculated dark count value.

Below the filter set a IR blocking filter can be introduced into the beam path. In applications with high laser intensities and a configuration where the laser heats the sample from the bottom, the filter protects the CCD chip from radiation damage. In the microscope setup used for these measurements the laser illuminates from the top so that only reflected light can reach the camera and the initial laser power is not very high.

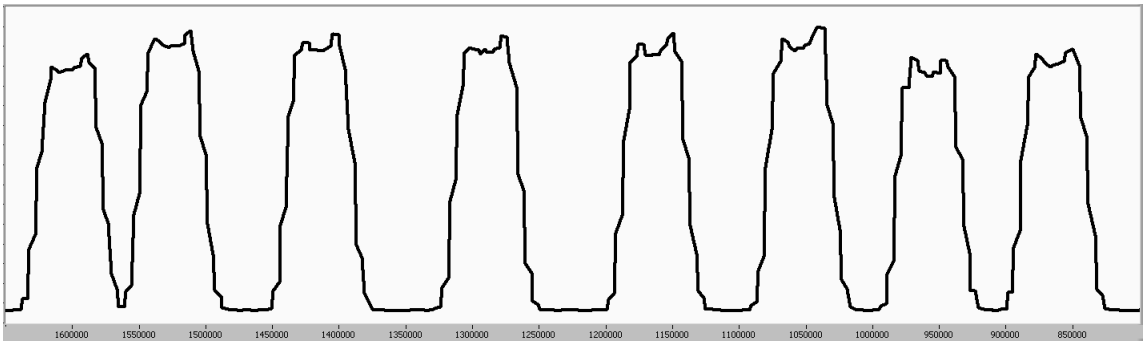

Figure B.1: Scan of the sample stage reveals the position of the capillaries. Units are stage driver specific ticks.

B.2 Capillaries

While sealants of different colors help to differentiate capillaries, some clays seemed to have a higher propensity of failing to seal the sample in the capillary. I would recommend to use one type of sealant for all capillaries to keep experimental conditions as constant as possible. Filling the capillaries is usually as simple as submerging one end in the sample liquid due to capillary action. Sometimes an obstruction keeps the capillary from filling. Watching the capillary against a bright, high-contrast background (laminated ceiling lamps will do nicely), it is possible to see the sample rising. Once the capillary is full, it is often difficult to distinguish the empty ones from the full ones.

One way to position the capillaries is to placed them on the silicon waver surface of the sample stage and then push them towards the other capillaries using the edges of the waver as guides for thumb and index finger (always using gloves of course). That way the capillary can be put on the waver far away from the already present capillaries to avoid touching them accidentally.

Condensation on the waver can lead to the capillary getting stuck and then jerkily detach again. Often this leads to repeating the placement of several capillaries. To avoid having to repeat the placement of several capillaries, a sample stage temperature of 35 °C is advisable.

B.3 Sample preparation

For the titration series in chapter 2 used for the sample preparation, the concentration was divided by half in every step. Other concentration rations are possible and should remain error resilient in principle, as long as the volumes in question can be pipetted reliably. To start, fill the Eppendorf tubes for the titration series with the buffer solution, lets say $20\mu l$. Next add the same volume of the titrated substance at twice the highest desired concentration to the first tube. Mix the combined fluid that now has the highest desired concentration. Transfer exactly the same volume as used before from the first to the second tube. Repeat the mixing and transfer steps for all Eppendorf tubes. Since it is not necessary, to change the volume the pipette is set to, a number of sources of errors common to pipetting procedures do not apply here. The number of preparation steps and complexity of the sample preparation at large should always be kept as low a possible to avoid unnecessary sources of errors.

Before filling the capillaries with the solutions, the Eppendorf tubes were first centrifuged. This way all the droplets on the walls and the lid were added to the bulk volume. Evaporation and condensation of volatile components can otherwise offset the concentration conditions in a solution. Next, the tube was thoroughly vortexed. A vortexer is a lab instrument to mix samples. One presses the bottom of the tube into a indented plate. This triggers the machine to move the plate in a fast circular motion. A circular flow is induced in the liquid in the sample tube. The liquid vortex—hence the name—negates sedimentation and all but the strongest separation of components. After this step, the sample is once again collected with a centrifuge.

B.4 Melting curve

Measurements of the melting curve in figure 2.11 were done in the same buffer used for the thermophoresis experiments at a concentration of $600nM$ per binding partner. SybrGreenI was added in $0.92\times$ standard concentration. Data shown in figure 2.11 was measured in 0.5 °C increments with a delay time of 5 seconds per temperature step from 30 °C to 75 °C

B.5 Gel electrophoresis

The gel was a 4% high resolution gel (2.5g agarose in 70ml TB-buffer). Gel electrophoresis parameters were 90V, 130mA and a limit of 50W with a run time of 75 minutes. The ladder used was a Fermentas O'Range Ruler at $5\mu l$ stained with μl SybrGreen I ($10\times$). Gels were cooled in an ice bath so denaturation was excluded. 1 μl loading buffer was added to the sample for every band.

Gel images were taken in the lab build gel dock with the SybrGreen and Cy5 filter respectively.

Bibliography

[1] G.K. Ackers and J.M. Holt. Asymmetric cooperativity in a symmetric tetramer: human hemoglobin. *Journal of Biological Chemistry*, 281(17):11441–11443, 2006.

[2] G.K. Ackers, J.M. Holt, Y. Huang, Y. Grinkova, A.L. Klinger, and I. Denisov. Confirmation of a unique intra-dimer cooperativity in the human hemoglobin $\alpha 1\beta 1$half-oxygenated intermediate supports the symmetry rule model of allosteric regulation. *Proteins: Structure, Function, and Bioinformatics*, 41(S4):23–43, 2000.

[3] P. Baaske, F.M. Weinert, S. Duhr, K.H. Lemke, M.J. Russell, and D. Braun. Extreme accumulation of nucleotides in simulated hydrothermal pore systems. *Proceedings of the National Academy of Sciences*, 104(22):9346, 2007.

[4] P. Baaske, C.J. Wienken, P. Reineck, S. Duhr, and D. Braun. Optical thermophoresis for quantifying the buffer dependence of aptamer binding. *Angewandte Chemie International Edition*, 49(12):2238–2241, 2010.

[5] A. Beer. Bestimmung der Absorption des rothen Lichts in farbigen Flüssigkeiten. *Ann. Phys. Chem*, 86(2):78–90, 1852.

[6] D. Braun and A. Libchaber. Trapping of dna by thermophoretic depletion and convection. *Physical review letters*, 89(18):188103, 2002.

[7] Itay Budin, Raphael J. Bruckner, and Jack W. Szostak. Formation of protocell-like vesicles in a thermal diffusion column. *Journal of the American Chemical Society*, 131(28):9628–9629, 2009. PMID: 19601679.

[8] B. Carazza and M. Casaktelli. Deduction of the lorentzian shape from maximum-entropy principle. *Lettere Al Nuovo Cimento (1971–1985)*, 20(18):666–668, 1977.

[9] S. Chatterjee, W. Pathmasiri, O. Plashkevych, D. Honcharenko, O.P. Varghese, M. Maiti, and J. Chattopadhyaya. The chemical nature of the 2'-substituent in the pentose-sugar dictates the pseudoaromatic character of the nucleobase (pka) in dna/rna. *Org. Biomol. Chem.*, 4(9):1675–1686, 2006.

[10] K. Corin, P. Baaske, D.B. Ravel, J. Song, E. Brown, X. Wang, S. Geissler, C.J. Wienken, M. Jerabek-Willemsen, S. Duhr, et al. A robust and rapid method of

producing soluble, stable, and functional g-protein coupled receptors. *PLoS One*, 6(10):e23036, 2011.

[11] A.B.C. Deutman, C. Monnereau, M. Moalin, R.G.E. Coumans, N. Veling, M. Coenen, J.M.M. Smits, R. De Gelder, J.A.A.W. Elemans, G. Ercolani, et al. Squaring cooperative binding circles. *Proceedings of the National Academy of Sciences*, 106(26):10471–10476, 2009.

[12] J.K.G. Dhont and WJ Briels. Single-particle thermal diffusion of charged colloids: Double-layer theory in a temperature gradient. *The European Physical Journal E: Soft Matter and Biological Physics*, 25(1):61–76, 2008.

[13] J.K.G. Dhont, S. Wiegand, S. Duhr, and D. Braun. Thermodiffusion of charged colloids: single-particle diffusion. *Langmuir*, 23(4):1674–1683, 2007.

[14] G. Dominguez, G. Wilkins, and M.H. Thiemens. The soret effect and isotopic fractionation in high-temperature silicate melts. *Nature*, 473(7345):70–73, 2011.

[15] S. Duhr and D. Braun. Thermophoretic depletion follows boltzmann distribution. *Physical review letters*, 96(16):168301, 2006.

[16] S. Duhr and D. Braun. Why molecules move along a temperature gradient. *Proceedings of the National Academy of Sciences*, 103(52):19678–19682, 2006.

[17] A. Einstein. Über die von der molekularkinetischen Theorie der Wärme geforderte Bewegung von in ruhenden Flüssigkeiten suspendierten Teilchen. *Annalen der Physik*, 322(8):549–560, 1905.

[18] AA El-Harakany, FM Abdel Halim, and AO Barakat. Dissociation constants and related thermodynamic quantities of the protonated acid form of tris-(hydroxymethyl)-aminomethane in mixtures of 2-methoxyethanol and water at different temperatures. *Journal of electroanalytical chemistry and interfacial electrochemistry*, 162(1-2):285–305, 1984.

[19] K. Ellwood, W. Huang, R. Johnson, and M. Carey. Multiple layers of cooperativity regulate enhanceosome-responsive rna polymerase ii transcription complex assembly. *Molecular and cellular biology*, 19(4):2613–2623, 1999.

[20] N. Geisel and U. Gerland. Physical limits on cooperative protein-dna binding and the kinetics of combinatorial transcription regulation. *Biophysical Journal*, 101(7):1569–1579, 2011.

[21] M. Gochin, R. Savage, S. Hinckley, L. Cai, et al. A fluorescence assay for rapid detection of ligand binding affinity to hiv-1 gp41. *Biological chemistry*, 387(4):477, 2006.

[22] C.M. Guldberg and P. Waage. Concerning chemical affinity. *Erdmann's Journal fr Practische Chemie*, 127:69–114, 1879.

[23] S. Hartmann, W. Köhler, and K.I. Morozov. The isotope soret effect in molecular liquids: a quantum effect at room temperatures. *Soft Matter*, 8(5):1355–1360, 2012.

[24] R.P. Haugland, M.T.Z. Spence, and I.D. Johnson. *The Handbook: A Guide to Fluorescent Probes and Labeling Technologies*. Molecular Probes, 2005.

[25] J.M. Holt and G.K. Ackers. Asymmetric distribution of cooperativity in the binding cascade of normal human hemoglobin. 2. stepwise cooperative free energy. *Biochemistry*, 44(36):11939–11949, 2005.

[26] F. Huang, P. Chakraborty, CC Lundstrom, C. Holmden, JJG Glessner, SW Kieffer, and CE Lesher. Isotope fractionation in silicate melts by thermal diffusion. *Nature*, 464(7287):396–400, 2010.

[27] C.A. Hunter and H.L. Anderson. What is cooperativity? *Angewandte Chemie International Edition*, 48(41):7488–7499, 2009.

[28] S. Iacopini, R. Rusconi, and R. Piazza. The "macromolecular tourist": Universal temperature dependence of thermal diffusion in aqueous colloidal suspensions. *The European Physical Journal E: Soft Matter and Biological Physics*, 19(1):59–67, 2006.

[29] H.R. Jiang, H. Wada, N. Yoshinaga, and M. Sano. Manipulation of colloids by a nonequilibrium depletion force in a temperature gradient. *Physical review letters*, 102(20):208301, 2009.

[30] Y. Kishikawa, H. Shinohara, K. Maeda, Y. Nakamura, S. Wiegand, and R. Kita. Temperature dependence of thermal diffusion for aqueous solutions of monosaccharide, oligosaccharide, and polysaccharide. *Physical Chemistry Chemical Physics*, 14:10147–10153, 2012.

[31] H. Korsching and K. Wirtz. Zur Trennung von Flüssigkeitsgemischen im Clusiusschen Trennrohr (Trennung der Zinkisotope). *Naturwissenschaften*, 27(20):367–368, 1939.

[32] L. Kou, D. Labrie, and P. Chylek. Refractive indices of water and ice in the 0.65-to 2.5-μm spectral range. *Applied Optics*, 32(19):3531–3540, 1993.

[33] N. Kozer and G. Schreiber. Effect of crowding on protein–protein association rates: fundamental differences between low and high mass crowding agents. *Journal of molecular biology*, 336(3):763–774, 2004.

[34] H. Krammer, F.M. Möller, and D. Braun. Thermal, autonomous replicator made from transfer rna. *Physical Review Letters*, 108(23):238104, 2012.

[35] J.H. Lambert, J.H. Lambert, J.H. Lambert, P. Philosopher, J.H. Lambert, and P. Philosophe. *Photometria sive de mensura et gradibus luminis, colorum et umbrae*. 1760.

[36] X. Li and J. Liang. Geometric cooperativity and anticooperativity of three-body interactions in native proteins. *Proteins: Structure, Function, and Bioinformatics*, 60(1):46–65, 2005.

[37] David P. Lide, editor. *CRC Handbook of Chemistry and Physics*. CRC PRESS, 81 edition, 2000.

[38] S. Lippok, S.A.I. Seidel, S. Duhr, K. Uhland, H.P. Holthoff, D. Jenne, and D. Braun. Direct detection of antibody concentration and affinity in human serum using microscale thermophoresis. *Analytical chemistry*, 84(8):3523–3530, 2012.

[39] C. Ludwig. Sitzungsber. akad. wiss. wien, math. *Naturwiss. Kl*, 20:539, 1856.

[40] A. Majee and A. Würger. Collective thermoelectrophoresis of charged colloids. *Physical Review E*, 83(6):061403, 2011.

[41] A. Majee and A. Würger. Charging of heated colloidal particles using the electrolyte seebeck effect. *Physical Review Letters*, 108(11):118301, 2012.

[42] G.S. Manning. Electrostatic free energy of the dna double helix in counterion condensation theory. *Biophysical chemistry*, 101:461–473, 2002.

[43] GS Manning. Counterion condensation theory of attraction between like charges in the absence of multivalent counterions. *The European Physical Journal E: Soft Matter and Biological Physics*, 34(12):1–18, 2011.

[44] D.W. Marquardt. An algorithm for least-squares estimation of nonlinear parameters. *Journal of the society for Industrial and Applied Mathematics*, 11(2):431–441, 1963.

[45] C.B. Mast and D. Braun. Thermal trap for dna replication. *Physical review letters*, 104(18):188102, 2010.

[46] T. Meissner and F.J. Wentz. The complex dielectric constant of pure and sea water from microwave satellite observations. *Geoscience and Remote Sensing, IEEE Transactions on*, 42(9):1836–1849, 2004.

[47] J.L. Mergny and L. Lacroix. Analysis of thermal melting curves. *Oligonucleotides*, 13(6):515–537, 2003.

[48] S. Metz, K. Haberzettl, S. Frühwirth, K. Teich, C. Hasewinkel, and G. Klug. Interaction of two photoreceptors in the regulation of bacterial photosynthesis genes. *Nucleic Acids Research*, 13:5901–5909, 2012 (40).

[49] R.W. O'Brien and L.R. White. Electrophoretic mobility of a spherical colloidal particle. *J. Chem. Soc., Faraday Trans. 2*, 74(0):1607–1626, 1978.

[50] C. Piguet. Enthalpy–entropy correlations as chemical guides to unravel self-assembly processes. *Dalton Trans.*, 40(32):8059–8071, 2011.

[51] T.D. Pollard. A guide to simple and informative binding assays. *Molecular Biology of the Cell*, 21(23):4061–4067, 2010.

[52] S.A. Putnam, D.G. Cahill, and G.C.L. Wong. Temperature dependence of thermodiffusion in aqueous suspensions of charged nanoparticles. *Langmuir*, 23(18):9221–9228, 2007.

[53] R. Radhakrishnan and T. Schlick. Orchestration of cooperative events in dna synthesis and repair mechanism unraveled by transition path sampling of dna polymerase β's closing. *Proceedings of the National Academy of Sciences of the United States of America*, 101(16):5970, 2004.

[54] P. Reineck, C.J. Wienken, and D. Braun. Thermophoresis of single stranded dna. *Electrophoresis*, 31(2):279–286, 2010.

[55] S.N. Semenov and M.E. Schimpf. Mass transport thermodynamics in nonisothermal molecular liquid mixtures. *Physics-Uspekhi*, 52(10):1045–1054, 2009.

[56] S.B. Smith and A.J. Bendich. Electrophoretic charge density and persistence length of dna as measured by fluorescence microscopy. *Biopolymers*, 29(8-9):1167–1173, 1990.

[57] C. Soret. Sur l'état d'équilibre que prend, du point de vue de sa concentration, une dissolution saline primitivement homogène, dont deux parties sont portées à des températures différentes. *Archives de Genève*, 3e période, tome II:48, 1879.

[58] D. Stadelmaier and W. Köhler. Thermal diffusion of dilute polymer solutions: The role of chain flexibility and the effective segment size. *Macromolecules*, 42(22):9147–9152, 2009.

[59] E. Stellwagen and N.C. Stellwagen. Determining the electrophoretic mobility and translational diffusion coefficients of dna molecules in free solution. *Electrophoresis*, 23(16):2794–2803, 2002.

[60] E. Stellwagen and N.C. Stellwagen. Probing the electrostatic shielding of dna with capillary electrophoresis. *Biophysical journal*, 84(3):1855–1866, 2003.

[61] N.C. Stellwagen, C. Gelfi, and P.G. Righetti. The free solution mobility of dna. *Biopolymers*, 42(6):687–703, 1997.

[62] Z. Tan, M. Wortman, K.L. Dillehay, W.L. Seibel, C.R. Evelyn, S.J. Smith, L.H. Malkas, Y. Zheng, S. Lu, and Z. Dong. Small-molecule targeting of proliferating cell nuclear antigen chromatin association inhibits tumor cell growth. *Molecular Pharmacology*, 81(6):811–819, 2012.

[63] C.A. Vega, R.A. Butler, B. Perez, and C. Torres. Thermodynamics of the dissociation of protonated tris (hydroxymethyl) aminomethane in 25 and 50 wt% 2-propanol from 5 to 45. degree. c. *Journal of Chemical and Engineering Data*, 30(4):376–379, 1985.

[64] D. Vigolo, S. Buzzaccaro, and R. Piazza. Thermophoresis and thermoelectricity in surfactant solutions. *Langmuir*, 26(11):7792–7801, 2010.

[65] M. von Smoluchowski. Zur kinetischen Theorie der brownschen Molekularbewegung und der Suspensionen. *Annalen der Physik*, 326(14):756–780, 1906.

[66] Q.M. Wang, M.A. Hockman, K. Staschke, R.B. Johnson, K.A. Case, J. Lu, S. Parsons, F. Zhang, R. Rathnachalam, K. Kirkegaard, et al. Oligomerization and cooperative rna synthesis activity of hepatitis c virus rna-dependent rna polymerase. *Journal of virology*, 76(8):3865–3872, 2002.

[67] X. Wang, K. Corin, P. Baaske, C.J. Wienken, M. Jerabek-Willemsen, S. Duhr, D. Braun, and S. Zhang. Peptide surfactants for cell-free production of functional g protein-coupled receptors. *Proceedings of the National Academy of Sciences*, 108(22):9049, 2011.

[68] Z. Wang, H. Kriegs, and S. Wiegand. Thermal diffusion of nucleotides. *The Journal of Physical Chemistry B*, 116:7463–7469, 2012.

[69] F.M. Weinert and D. Braun. An optical conveyor for molecules. *Nano letters*, 9(12):4264–4267, 2009.

[70] A. Whitty. Cooperativity and biological complexity. *Nature chemical biology*, 4(8):435–439, 2008.

[71] C.J. Wienken, P. Baaske, S. Duhr, and D. Braun. Thermophoretic melting curves quantify the conformation and stability of rna and dna. *Nucleic Acids Research*, 39(8):e52–e52, 2011.

[72] C.J. Wienken, P. Baaske, U. Rothbauer, D. Braun, and S. Duhr. Protein-binding assays in biological liquids using microscale thermophoresis. *Nature Commun.*, 1:100, 2010.

[73] A. Würger. Transport in charged colloids driven by thermoelectricity. *Physical review letters*, 101(10):108302, 2008.

[74] A. Würger. Temperature dependence of the soret motion in colloids. *Langmuir*, 25(12):6696–6701, 2009.

[75] S.B. Zimmerman. Macromolecular crowding effects on macromolecular interactions: some implications for genome structure and function. *Biochimica et biophysica acta, N. Gene structure and expression*, 1216(2):175–185, 1993.

[76] M. Zuker. Mfold web server for nucleic acid folding and hybridization prediction. *Nucleic acids research*, 31(13):3406–3415, 2003.

Danksagung

Dieter hat mir die Möglichkeit gegeben, in seinem Labor Diplom- und Doktorarbeit zu machen. In dieser Zeit hat er mir die Aspekte des wissenschaftlichen Arbeitens nahegebracht, auf das einen kein Studium vorbereiten kann. Die Selbstverständlichkeit mit der in seiner Gruppe Änderungen am Messaufbau, Auswertesystemen, Analysesoftware und Proben schnell selbst durchgeführt werden, hat mir die Gelegenheit gegeben mehr zu frähsen, programmieren, bedampfen, justieren, designen, als ich mir hätte vorstellen können. Außerdem hat mich die Zeit im Labor endgültig zum Kaffee-Trinker gemacht.
Vielen Dank Dieter!

Zudem möchte ich auch all denen danken, die durch ihre Unterstützung diese Arbeit möglich gemacht haben.

Christof Mast für Diskussionen aller Art bei einem Kaffee. Zudem möchte ich Christof für die zur Graphik auf Seite 3 danken.
Hubert Krammer für ein stehts offenes Ohr und einer immer vernünftigen Sicht auf die Dinge.
Benjamin Andrae und Alex Buchner für Treffen zum koreanischen Mittagessen und Korrekturen.
Franziska Kriegel für die viele, viele Hilfe im Labor.
Ulrich Lichnovsky für immer wieder neue und anregende Diskussionen.
Moritz Kreysing für Diskussionen von Fischaugen bis Prozessorüberhitzung. Und Korrekturen für diese Arbeit.
Simon Lanzmich für das Korrekturlesen dieser Arbeit und viele kleine Diskussionen.
Philipp Serr für deutlich beschleunigte Datenauswertung.
Dem ganzen Labor Braun für die schöne Zeit: Shoichi, Maren, Susanne, Manuel, Georg
Sowie den ehemaligen Christof Wienken, Natan Osterman, Philipp Reineck und Svenja Lippok.
Tom und Angelika für Unterstützung im Chemielabor.
Meinen Eltern.
Naomi und Maja-Lucia, dass sie meine unvergleichlichen Töchter sind.
Meiner Frau Johanna, für Unterstützung, Verständnis, Geduld und unsere beiden Mäuse.

Und auch speziell all denen, die ich hier vergessen habe.
Danke.

Lebenslauf

Mario Herzog

Address	Versaillerstr. 17 81677 München Germany
e-mail	mario.herzog@gmail.com
Born	July, 9th 1981 in Starnberg, Germany
Nationality	German

2009 - today	PhD student, Ludwig-Maximilians-Universität München
2008 - 2009	Diploma student, Ludwig-Maximilians-Universität München, Germany Topic: "Virtual Thermal Gradient"
2005 - 2009	Student, physics, Ludwig-Maximilians-Universität München, Germany
2004 - 2005	Student, physics, Eidgenössische Technische Hochschule Zürich, Switzerland
2002 - 2004	Student, physics, Technische Universität München, Germany
2001	Abitur, Wilhelmsgymnasium München, Germany

submitted to Physical Review Letters

Size-Transition in Thermophoresis of DNA and RNA

Mario Herzog and Dieter Braun

Systems Biophysics, Physics Department, Center for Nanoscience,
Ludwig Maximilians Universität München, Amalienstrasse 54, 80799 München, Germany

Abstract. *What makes dissolved molecules move in a temperature gradient? To understand the microscopic basis of thermophoresis, we probed the limits of the previously tested plate capacitor model. We find a saturation of thermophoresis when the Debye length exceeds the molecule radius. Such behavior was previously predicted in the spherical limit of the previous plate capacitor model. No significant influence from a recently discussed thermoelectrical basis of thermophoresis could be detected under the probed physiological conditions. Together with non-ionic contributions, the finding allows a microscopic description of oligonucleotide thermophoresis over a wide range of Debye lengths (0.4-14nm), temperatures (5-75°C) and sizes (5-50 bases).*

Introduction. Finding a well-defined model system to probe the molecular basics of thermophoresis [1][2] is a complex problem. Polymers in non-aqueous solutions show a clear scaling behavior [3] and the mass dependence of the thermophoresis in silica melts [4] can be approached with quantum mechanical treatments [5][6]. In aqueous solutions, the study of biomolecules is advantageous due to their high purity and precise length definition. In addition, covalently linked fluorescence markers allow direct imaging measurements at low concentrations while maintaining microscale measurement chambers to suppress effects of thermal convection.

Biomolecule thermophoresis proved highly useful to measure the binding affinity of proteins [7], including the relevant cases of antibody binding in serum [8], sensing with GPCR receptors [9][10], aptamer binding [11] and small-molecule binding for pharmaceutical applications [7][12][13]. However, the measurements of binding affinity could be significantly enhanced by a detailed molecular understanding of thermophoresis. Moreover, the understanding of thermophoresis is also essential for molecular evolution where thermophoresis is posited to accumulate biomolecules in thermal traps [14][15][16]. Together with the thermal cycling provided by the convection in high chambers, accumulation and replication can be combined [17], possibly implementing Darwinian evolution by thermal gradients.

Thermophoresis remains a field under active investigation with diverse approaches [6][18][19][20][21][22]. The experiments presented here were in part motivated by recent arguments regarding a thermo-electrically driven mode of thermophoresis [23][24], tested by the weakening of thermophoresis at high pH values [25]. While theories of non-aqueous thermophoresis struggle to define the dominant molecular interactions that give rise to thermophoresis, ionic thermophoresis in water was predicted for polystyrene beads and long double stranded DNA over three orders of magnitude in size [26]. But these experiments probed the capacitor model [26][27][28] only in the plate capacitor regime of Debye lengths smaller than the radius of the particles. Here we test the transition regime towards a spherical capacitor model for larger Debye lengths and smaller particle diameters. We probed single and double stranded DNA and RNA of different lengths under various salt and temperature conditions. As shown below, the data is well described by the spherical capacitor model proposed by Dhont [28].

Materials and Methods. Measurements were performed on an upright fluorescence microscope (Zeiss Scope.A1) with coaxial optical heating [7] using an air objective (Partec 40x/0.80 NA), a CCD camera (Andor Luca DL-658M-TIL) and heating from an infrared laser (Fibotec, λ=1480nm, typical emission power 28 mW). Synthetic DNA and RNA (Biomers, Ulm, Germany) were labeled at the 5-prime end with the fluorescent dye HEX (6-carboxy-2',4,4',5',7,7'-hexachlorofluorescein) and deluted to a concentration of 1 µM. The Debye length λ_{DH} was titrated using KCl and monovalent 1 mM TRIS (2-Amino-2-hydroxymethyl-propane-1,3-diol) at pH 7.8 and 25°C. To access the Debye length λ_{DH}=13.8nm, buffering was reduced to 0.5 mM TRIS. Single stranded DNA (ssDNA) was measured for lengths of 5, 10, 22 and 50 bases, single stranded RNA (ssRNA) for lengths of 5, 10 and 22 bases, double stranded DNA (dsDNA) for 22 and 50 base pairs and double stranded RNA (dsRNA) for 22 base pairs.

Borosilicate capillaries with a rectangular cross section of 50 x 500 µm were used as measurement chambers (VitroCom Vitrotubes #5005-050). Intermittent local optical heating was measured in x-y-dimensions using the temperature dependent quantum efficiency of the fluorescence dye BCECF (acid form, Invitrogen B-1151) at a concentration of 50 µM, buffered at pH 7.8 using 10mM TRIS. Air immersion objectives and moderate depletion (<50%) ensured that temperature and concentration profiles were linearly averaged along the optical axis in z-direction. Fitting the temperature profiles with a Lorentzian $T(r) = T_0 + \Delta T\, w^2/(r^2+w^2)$ revealed a width w=70±3 µm with a temperature increase set to ΔT=1.4 – 2.3 K. The oligonucleotide concentration response in space and time was recorded at 5 Hz by fluorescence imaging and interpreted using a finite element simulation [27][14] (see supplementary online material). The analysis independently determined the Soret coefficient S_T

governing thermophoretic depletion and the diffusion coefficient D for each measurement point. Including pipetting errors and camera noise, the errors from the measurement were on average 10%. The standard deviation of the fit is provided as error bars. Finite element simulations confirmed that the chamber height of 50 µm kept errors from residual thermal convection below 0.6µm/s in the observation plane and ensured above error limits.

The hydrodynamic radii were calculated from the diffusion coefficient $D(\lambda_{DH},T)$ with the Einstein-Stokes formula [29][30] for single stranded DNA of length 5, 10, 22 and 50 bases to 1.5±0.9, 1.7±0.4, 2.1±0.6 and 4.6±0.8 nm, respectively. The radius was largely irrespective of the Debye length (see supplementary material) and was therefore averaged over the Debye length.

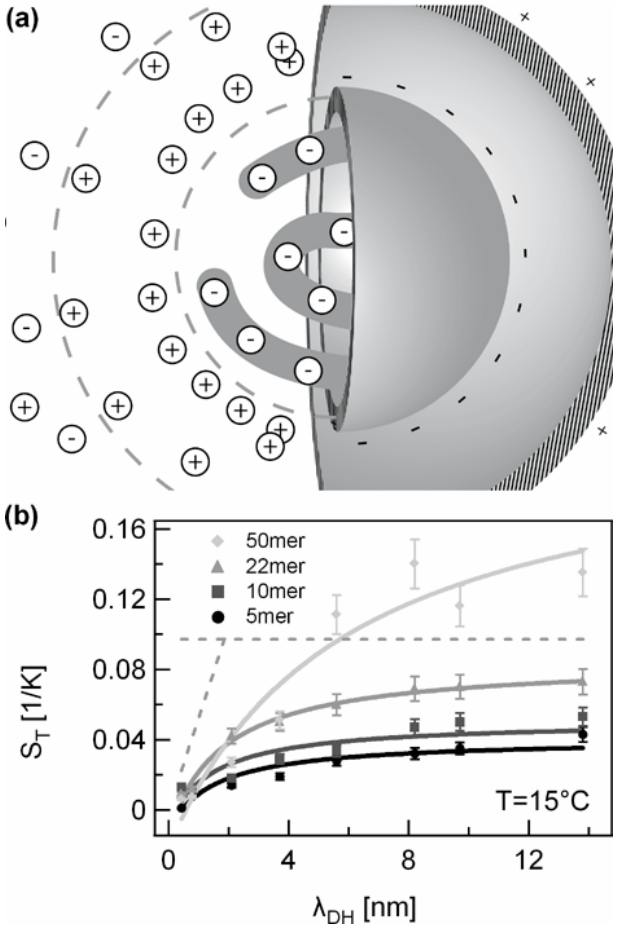

Figure 1. Spherical capacitor model predicts thermophoresis of DNA and RNA.
(a) DNA and RNA are approximated as charged polymer in a spherical geometry. The ionic contributions to thermophoresis are calculated from long range electrostatic shielding. (b) Measurements on single stranded DNA with lengths of 5, 10, 22 and 50 bases confirm the predicted size regimes. For Debye lengths λ_{DH} smaller than the hydrodynamic radius R, a planar capacitor model can be assumed [26][27] and the Soret coefficient rises linearly with λ_{DH}. For the opposite limit $R < \lambda_{DH}$, the Soret coefficients saturate towards a constant value. Both limits are shown for the 22mer as broken lines. As seen, the transition between both regimes shifts to increasing λ_{DH} for larger molecules.

Theory. Following the argument by Dhont [28], the Debye screening of the electrostatic interaction between a charged particle and an ionic solvent is modeled as a spherical capacitor. The two spheres shown in Figure 1 correspond to the charged particle surface and the shielding ion distribution around it. The characteristic length between the two surfaces is the Debye length $\lambda_{DH} = \sqrt{\varepsilon_r \cdot \varepsilon_0 \cdot k_B \cdot T / \left(N_A \cdot e^2 \cdot \sum_i c_i z_i^2 \right)}$. N_A denotes the Avogadro constant, e the elementary charge, c_i the concentration and z_i the changes of the i-th ion type, k_B the Boltzmann constant, T the temperature, ε_r the relative permittivity of the solvent, ε_0 the vacuum permittivity. The Debye length increases with decreasing salt concentration.

In an abbreviation of Dhont's argument [28], let us consider the work involved in charging a shielding capacitor $W = Q^2 / (2 \cdot C)$. The capacity of a spherical capacitor is given by $C = 4\pi\varepsilon_r\varepsilon_0 \cdot \left[R^{-1} - (R+d)^{-1} \right]^{-1}$ where R is the radius of the inner sphere. The detailed analysis confirms that the distance d between the spheres equals the Debye length λ_{DH}. By comparing the thermophoretic depletion in steady state $c = c_0 exp\left[-S_T (T - T_0) \right]$ with a Boltzmann distribution [28][31], the Soret coefficient is given by $S_T = (k_B T)^{-1} \cdot dW / dT$. As result, the Soret coefficient for ionic shielding is given by:

$$S_T = \frac{1}{T} + \frac{\left(Q_{perbase} \cdot bases \cdot e \right)^2}{16 \cdot \pi \cdot k_B \cdot T^2 \cdot \varepsilon_r \cdot \varepsilon_0 \cdot \lambda_{DH}} \cdot \frac{1}{(1 + R/\lambda_{DH})^2} \cdot \left(1 - \frac{\partial ln\rho(T)}{\partial lnT} - \frac{\partial ln\varepsilon_r(T)}{\partial lnT} \cdot \left(1 + 2 \cdot \frac{\lambda_{DH}}{R} \right) \right) + S_T^{NI} \quad (1)$$

We have added a non-ionic contribution S_T^{NI} to the equation and denoted with ρ the density of the solvent and $Q_{per\ base}$ the charge of the colloid in units of the elementary charge e per base for single stranded and per base pair for double stranded oligonucleotides. Since the radius R of the molecule is determined through the diffusion coefficient D and the Debye length is given by the salt concentration, only the variables $Q_{per\ base}$ and S_T^{NI} are unknown.

Above thermodynamical approach can only hold when the experiment is kept close to thermodynamic equilibrium. The depleted concentration never drops below 50% of the bulk concentration, meaning that the activation barrier to diffuse back into the heated region is $0.7 \cdot k_B T$, well reachable by thermodynamic fluctuations in the time of the experiment. Similar equilibrium approaches proved successful to derive Soret coefficients [18][26][28][31].

For the limit of high salt concentrations, the ionic contribution becomes zero and the remaining non-ionic contribution S_T^{NI} can be extrapolated from the measurements for $\lambda_{DH} \rightarrow 0$. We fit the temperature dependence of the intercept S_T^{NI} with the empirical dependence

$$S_T^{NI} = S_T^{\infty} \cdot \left[1 - exp\left(\frac{T^* - T}{T_0} \right) \right] \qquad (2)$$

proposed by Piazza [32] and tested for a number of molecules in aqueous solutions [33][21][34]. Here, S_T^{∞} is the limit reached for arbitrarily high temperatures, T* the temperature at which S_T^{NI} changes sign and T_0 determines how fast S_T^{∞} is approached with growing temperature. As we will see, combining equations (1) and (2) describes thermophoresis of short single and double stranded DNA and RNA over a wide range of temperatures and salt concentrations.

Results. The size transition of thermophoresis at $\lambda_{DH} \approx R$ was probed with different sizes of DNA (Figure 1b) and RNA (supplementary material). To understand the size transition hidden in equation (1), let us consider both cases $\lambda_{DH}/R \rightarrow 0$ and $\lambda_{DH}/R \rightarrow \infty$. For vanishing Debye length the capacitor behaves like a parallel plane capacitor and the Soret coefficient increases linearly with the Debye length λ_{DH} [26] according to $\lim_{\lambda_{DH} \rightarrow 0} S_T = \frac{1}{T} + \frac{\left(Q_{perbase} \cdot bases \cdot e^-\right)^2}{16 \cdot \pi \cdot k_B \cdot T^2 \cdot \varepsilon_r \cdot \varepsilon_0 \cdot R^2} \cdot \left(1 - \frac{\partial ln\rho(T)}{\partial lnT} - \frac{\partial ln\varepsilon_r(T)}{\partial lnT} \right) \cdot \lambda_{DH}$. If λ_{DH} increases beyond the radius of the colloid, we obtain a charged sphere and find constant Soret coefficient $\lim_{\lambda_{DH} \rightarrow \infty} S_T = \frac{1}{T} + \frac{\left(Q_{perbase} \cdot bases \cdot e^-\right)^2}{16 \cdot \pi \cdot k_B \cdot T^2 \cdot \varepsilon_r \cdot \varepsilon_0 \cdot R} \cdot \frac{-2 \cdot \partial ln\varepsilon_r(T)}{\partial lnT}$. In Figure 1b, both limits are indicated for 22mers of ssDNA as dotted lines. As seen, the intersection of both extreme cases moves to smaller λ_{DH} values for smaller DNA molecules. The behavior is fitted in detail by the non-approximated equation (1) where only the charge per base $Q_{per\ base}$ and the constant offset S_T^{NI} were fitted. Previous measurements probed only a limited range of Debye lengths and the size transition was not revealed [27].

In Figure 2a, the extrapolated non-ionic offset S_T^{NI} for the limit λ_{DH}=0 is plotted against temperature for a range of different single stranded DNA samples. The offset fits well with the empirical formula (2), demonstrating the possibility to clearly separate ionic and non-ionic contributions. While the fitted amplitudes S_T^{∞} showed a trend with respect to DNA and RNA length (Figure 3b), the values of T_0 and T* scattered with average values of T_0=14±5°C and T*=23±12°C (supplementary material). The value of T* agrees with the previously determined T*=18°C for long double stranded DNA [26].

In Figure 2b, two-dimensional plots of the Soret coefficient S_T are shown versus Debye length and temperature (thin lines) together with the theoretical fit (thick lines). The previously shown Figure 1b is a horizontal cut through the data while the Figure 2a is a vertically cut extrapolated towards λ_{DH}=0. As

seen, all the experimental data are well accounted for by equation (1) over the whole parameter range for single stranded DNA and RNA with various lengths.

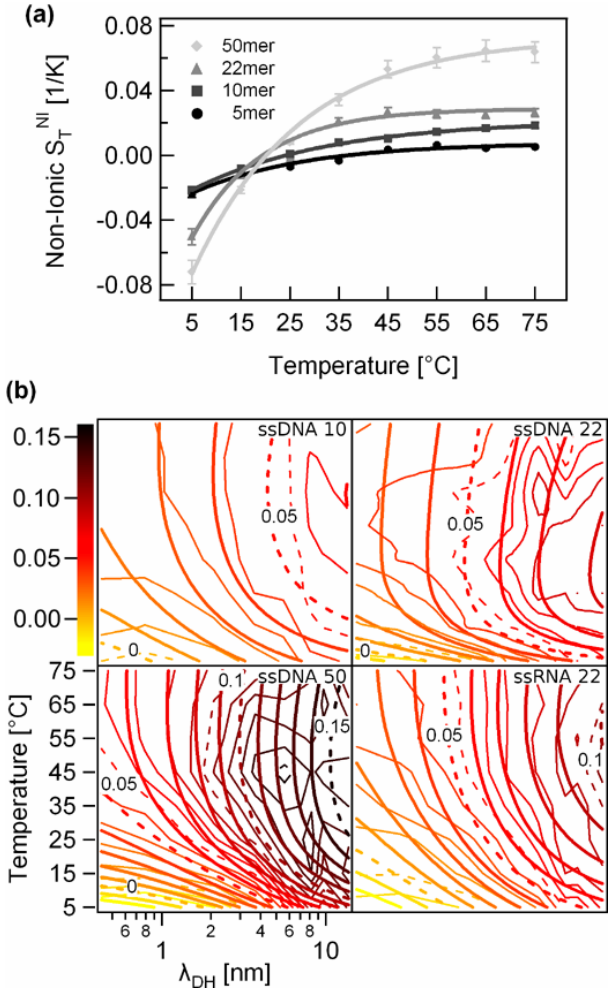

Figure 2. Prediction over temperature and salt for single stranded DNA and RNA.
(a) Apart from ionic thermophoresis, a non-ionic contribution S_T^{NI} can be subtracted by extrapolating the measurements to vanishing Debye lengths. The temperature dependence of S_T^{NI} fits well with the empirical equation (2) proposed by Piazza [32]. (b) The combination of ionic and non-ionic predictions of the Soret coefficient by equation (1) yield a robust description (broad lines) of the two-dimensional measurement set (thin lines) over temperature and Debye length. Only S_T^{NI} and the charge per base are fitted variables.

Discussion. The effective charge per base $Q_{\text{per base}}$ is the only fitting parameter of the ionic thermophoresis model (eq. 1). As seen in Figure 3a, we find a significant increase for shorter oligonucleotides, well understandable from the limited ability to attract bound shielding charges for smaller polymers and a fixed charge contribution from the end charge of the 5' fluorescent dye HEX. Both effects are known from independent measurements of DNA's effective charge using electrophoresis [35][36][37][38].

To fit the measurements, no dependence of charge on temperature was required (Figure 2b), confirming the universality of equation (1). No difference is found for RNA and DNA, reflecting the identical charge of their phosphate backbone and negligible contributions from the different sugar moieties. Double stranded DNA and RNA show nearly identical $Q_{\text{per base}}$ values, despite the fact that one base-pair is counted as a single base, indicating an effective local shielding of the backbones or effects of the significantly enhanced persistent length. The charge per base pair drops to 0.3 e for double stranded DNA, converging well to the previously published value of 0.12 e- for long DNA in the range of 50-50000 base pairs [26] .

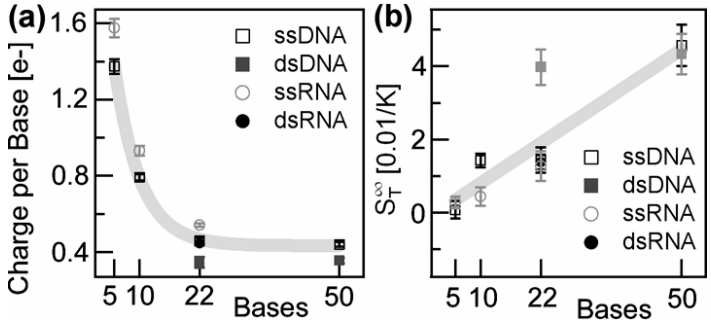

Figure 3. Length scaling of charge and non-ionic contribution.
(a) The effective charge per base ($Q_{per\ Base}$) is the only fitting parameter of ionic thermophoresis. It drops with increasing length. (b) The magnitude of the empirical non-ionic contribution scales linearly with the polymer length as expected from short range hydrophobic effects.

As seen in Figure 3b, the amplitude of non-ionic thermophoresis S_T^∞ increases linearly with the length of the oligonucleotide. Such linear trend would be expected for short range hydrophobic interactions with oriented water along the length of the polymer. An offset of the linearity is almost negligible, suggesting a minor contribution from the polymer ends as expected. It should be however noted that a plot of S_T^∞ versus the surface of the molecule yields a similar linear correlation (supplementary material).

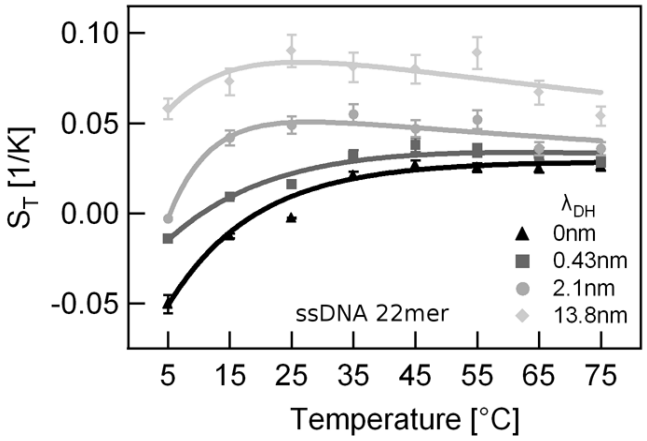

Figure 4. Nontrivial temperature dependence. *The magnitude of thermophoresis drops with temperature for ionic thermophoresis (eq. 1) but increases with temperature from the non-ionic contribution (eq. 2). The result is a maximum of thermophoretic depletion for intermediate temperatures at low salt concentrations.*

The ionic contribution to thermophoresis decreases as temperature increases (equation 1), whereas the non-ionic contribution rises with increasing temperature (equation 2). In combination, S_T rises for low temperatures and then drops again as S_T^{NI} gains influence. Seen in Figure 4, this nontrivial prediction of a maximum is found experimentally. As the Debye length is reduced, the curves converge to the monotonically increasing S_T^{NI}. This behavior was found for all measured oligonucleotides (Figure 2b, vertical cross sections).

In contrast to a number of recent theoretical [23][24][39] and experimental works [25], electrical fields induced by the temperature gradient appear not to be relevant in our measurements. For example, in the pH range of constant DNA charge (pH 5 - 9) the measured Soret coefficient is constant and shows no dependence on OH^- concentration (supplementary material). The buffer TRIS keeps the pH value between 8.4 (5 °C) and 6.5 (75 °C) [40][41] and the oligonucleotide charge should not change significantly since no pK_a values for nucleotides are located between 4.3 and 8.7 [42]. The pK_a value of the 6-Hex label is ~3 [43]. As seen, outside this pH range, the thermophoretic depletion drops considerbly, expected from the changed nucleotide charge as the pH passes the pK_a values. Both the buffering of TRIS and the capillary glass walls are expected to keep thermally accumulated OH^- ions from locally offsetting the pH. The electrophoretic mobility of nucleotides is well known [44-46] with a predominantly length independent characteristic and growing only slightly for reduced salt concentrations. These dependencies do not account for the measured Soret coefficients quantitatively.

Conclusion. We measured the thermophoresis of short DNA and RNA strands in aquous solutions. The setting allowed us to probe ionic thermophoresis across a previously untested transition where the hydrodynamic radius R is smaller than the Debye length λ_{DH}. Beyond the previously explored linear raise of the Soret coefficient S_T for $\lambda_{DH}<R$, we find a saturating Soret coefficient for $\lambda_{DH}>R$. The position of the transition depends on the hydrodynamic radius. This behavior confirms in detail the prediction for thermophoresis by Dhont et.al [28] using a capacitor model of thermophoresis. The experiments corroborate, that the ionic contribution of aqueous thermophoresis is adequately described by a microscopic theory over a wide range of parameters.

Acknowledgments. We thank Philipp Reineck, Christoph Wienken and Christian Speck for initial measurements and Philipp Baaske for help with the measurement setup. Christof Mast, Shoichi Toyabe and Moritz Kreysing gave valuable comments on the manuscript at various stages. Financial support from the NanoSystems Initiative Munich, the LMU Initiative Functional Nanosystems and the ERC Starting Grant is gratefully acknowledged.

References.

[1] Ludwig, C., Naturwiss. Kl **20**, 539 (1856).

[2] Soret, C., Archives de Genève **3e période, tome II**, 48 (1879).

[3] Stadelmaier, D. and Köhler, W., Macromolecules **42**, 9147-9152 (2009).

[4] Huang, F.; Chakraborty, P.; Lundstrom, C.; Holmden, C.; Glessner, J.; Kieffer, S. and Lesher, C., Nature **464**, 396-400 (2010).

[5] Dominguez, G.; Wilkins, G. and Thiemens, M., Nature **473**, 70-73 (2011).

[6] Hartmann, S.; Köhler, W. and Morozov, K., Soft Matter **8**, 1355-1360 (2012).

[7] Wienken, C.; Baaske, P.; Rothbauer, U.; Braun, D. and Duhr, S., Nature Commun. **1**, 100 (2010).

[8] Lippok, S.; Seidel, S.; Duhr, S.; Uhland, K.; Holthoff, H.; Jenne, D. and Braun, D., Analytical chemistry **84**, 3523-3530 (2012).

[9] Wang, X.; Corin, K.; Baaske, P.; Wienken, C.; Jerabek-Willemsen, M.; Duhr, S.; Braun, D. and Zhang, S., Proceedings of the National Academy of Sciences **108**, 9049 (2011).

[10] Corin, K.; Baaske, P.; Ravel, D.; Song, J.; Brown, E.; Wang, X.; Geissler, S.; Wienken, C.; Jerabek-Willemsen, M.; Duhr, S. and others, PLoS One **6**, e23036 (2011).

[11] Baaske, P.; Wienken, C.; Reineck, P.; Duhr, S. and Braun, D., Angewandte Chemie International Edition **49**, 2238-2241 (2010).

[12] Tan, Z.; Wortman, M.; Dillehay, K.; Seibel, W.; Evelyn, C.; Smith, S.; Malkas, L.; Zheng, Y.; Lu, S. and Dong, Z., Molecular Pharmacology **81**, 811-819 (2012).

[13] Metz, S.; Haberzettl, K.; Frühwirth, S.; Teich, K.; Hasewinkel, C. and Klug, G., Nucleic Acids Research **13**, 5901–5909 (2012 (40)).

[14] Baaske, P.; Weinert, F.; Duhr, S.; Lemke, K.; Russell, M. and Braun, D., Proceedings of the National Academy of Sciences **104**, 9346 (2007).

[15] Budin, I.; Bruckner, R. J. and Szostak, J. W., Journal of the American Chemical Society **131**, 9628-9629 (2009).

[16] Weinert, F. and Braun, D., Nano letters **9**, 4264-4267 (2009).

[17] Mast, C. and Braun, D., Physical review letters **104**, 188102 (2010).

[18] Dhont, J. and Briels, W., The European Physical Journal E: Soft Matter and Biological Physics **25**, 61-76 (2008).

[19] Semenov, S. and Schimpf, M., Physics-Uspekhi **52**, 1045-1054 (2009).

[20] Jiang, H.; Wada, H.; Yoshinaga, N. and Sano, M., Physical review letters **102**, 208301 (2009).

[21] Putnam, S.; Cahill, D. and Wong, G., Langmuir **23**, 9221-9228 (2007).

[22] Würger, A., Langmuir **25**, 6696-6701 (2009).

[23] Majee, A. and Würger, A., Physical Review Letters **108**, 118301 (2012).

[24] Majee, A. and Würger, A., Physical Review E **83**, 061403 (2011).

[25] Vigolo, D.; Buzzaccaro, S. and Piazza, R., Langmuir **26**, 7792-7801 (2010).

[26] Duhr, S. and Braun, D., Proceedings of the National Academy of Sciences **103**, 19678-19682 (2006).

[27] Reineck, P.; Wienken, C. and Braun, D., Electrophoresis **31**, 279-286 (2010).

[28] Dhont, J.; Wiegand, S.; Duhr, S. and Braun, D., Langmuir **23**, 1674-1683 (2007).

[29] Einstein, A., Annalen der Physik **322**, 549-560 (1905).

[30] von Smoluchowski, M., Annalen der Physik **326**, 756-780 (1906).

[31] Duhr, S. and Braun, D., Physical review letters **96**, 168301 (2006).

[32] Iacopini, S.; Rusconi, R. and Piazza, R., The European Physical Journal E: Soft Matter and Biological Physics **19**, 59-67 (2006).

[33] Kishikawa, Y.; Shinohara, H.; Maeda, K.; Nakamura, Y.; Wiegand, S. and Kita, R., Physical Chemistry Chemical Physics **14**, 10147–10153 (2012).

[34] Wang, Z.; Kriegs, H. and Wiegand, S., The Journal of Physical Chemistry B **116**, 7463–7469 (2012).

[35] Manning, G., Biophysical chemistry **101**, 461-473 (2002).

[36] Manning, G., The European Physical Journal E: Soft Matter and Biological Physics **34**, 1-18 (2011).

[37] O'Brien, R. and White, L., J. Chem. Soc., Faraday Trans. 2 **74**, 1607-1626 (1978).

[38] Smith, S. and Bendich, A., Biopolymers **29**, 1167-1173 (1990).

[39] Würger, A., Physical review letters **101**, 108302 (2008).

[40] Vega, C.; Butler, R.; Perez, B. and Torres, C., Journal of Chemical and Engineering Data **30**, 376-379 (1985).

[41] El-Harakany, A.; Abdel Halim, F. and Barakat, A., Journal of electroanalytical chemistry and interfacial electrochemistry **162**, 285-305 (1984).

[42] Chatterjee, S.; Pathmasiri, W.; Plashkevych, O.; Honcharenko, D.; Varghese, O.; Maiti, M. and Chattopadhyaya, J., Org. Biomol. Chem. **4**, 1675-1686 (2006).

[43] Haugland, R.P. and Spence, M.T.Z. and Johnson, I.D., The Handbook: *A Guide to Fluorescent Probes and Labeling Technologies*, 10th Edition. (Molecular Probes, 2005), p. 953

[44] Stellwagen, N.; Gelfi, C. and Righetti, P., Biopolymers **42**, 687-703 (1997).

[45] Stellwagen, E. and Stellwagen, N., Electrophoresis **23**, 2794-2803 (2002).

[46] Stellwagen, E. and Stellwagen, N., Biophysical journal **84**, 1855-1866 (2003).

[47] Wienken, C.; Baaske, P.; Duhr, S. and Braun, D., Nucleic Acids Research **39**, e52-e52 (2011).

Supporting Online Information

S1 Fluorescence Evaluation derives S_T and D

A LabView program was used to fit the fluorescence prediction of a radial symmetrical 1D FEMlab simulation (attached) to the optically detected fluorescence. The detection as well as simulation is determined for the whole field of view of the camera (radially averaged). Five seconds of the equilibrated sample, then 120 seconds of the sample responding to the laser heating followed by 120 seconds of back-diffusion after switching off the laser were compared to the simulation in 5 Hz steps. Adjusting parameters until theory prediction and observed fluorescence match throughout the whole filed of view and time of the measurement yields S_T and D values.

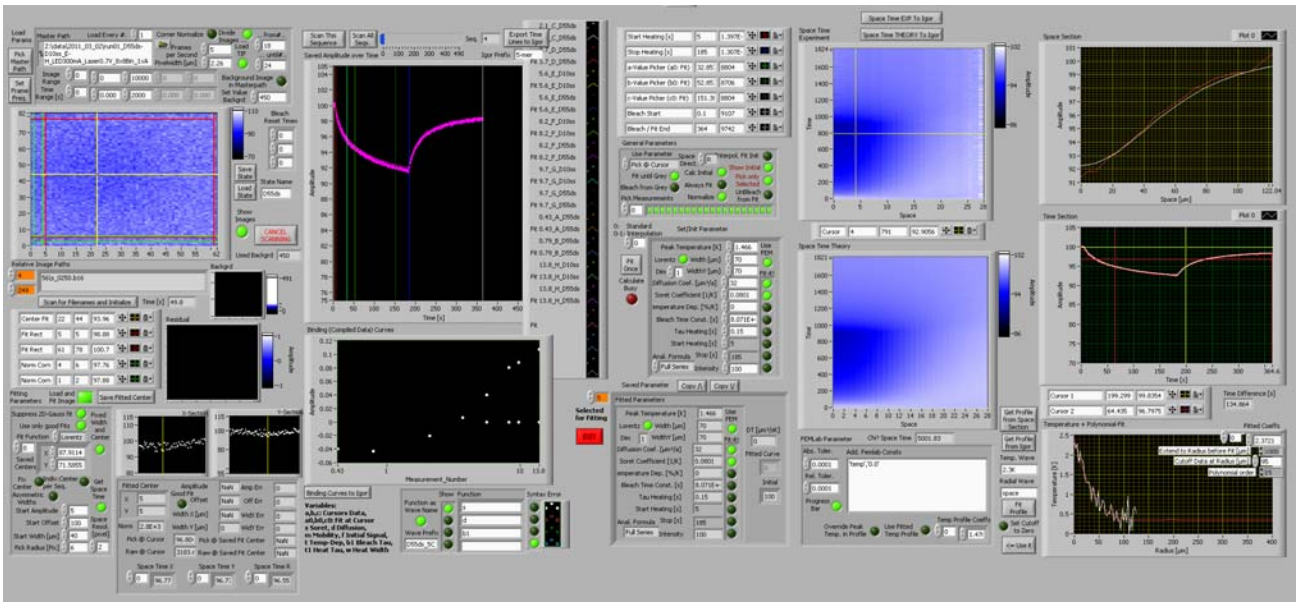

S2 Hydrodynamic Radius versus Debye length

The independently derived diffusion coefficient values D do not show a strong dependence on the salt concentration and thus the shielding length λ_{DH}. We deduce D from the fluorescence change of the area around the laser spot and over a local heating and back-diffusion cycle. Temperature dependent fluorescence shows a fast change with a time constant of 150ms the moment the laser is switched on and off. The remaining curvature of the fluorescence change is modeled by the diffusion of the molecules. The temperature response of the dye dominates the fluorescence when S_T gets very close to zero. This is the case for low temperatures and short λ_{DH} lengths where the fitted diffusion coefficients and thus the determined hydrodynamic radius R show considerable noise. The absence of clear trends in the measurements of the hydrodynamic radius R with respect to the Debye length prompted us to average the radius values over the Debye length.

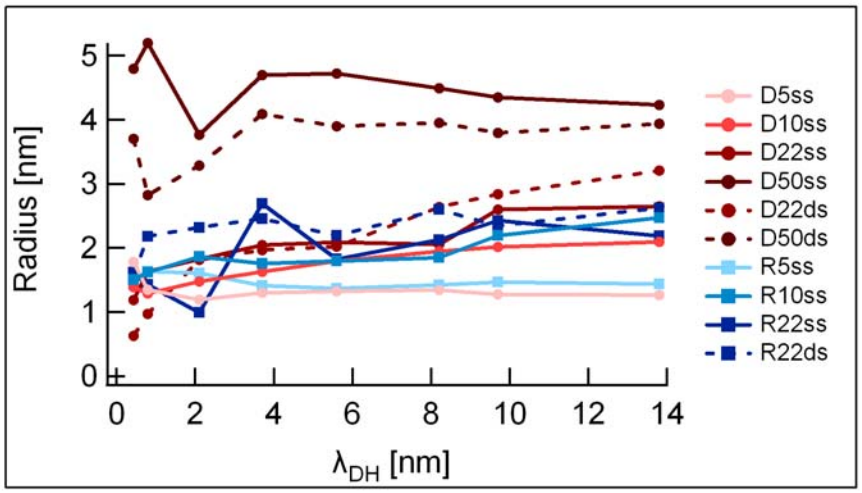

S3 Fitted T_0 and T*

In contrast to the amplitude value S_T^{∞} , which scales roughly linearly with the size of the particle, no clear interpretation could be found for the parameters T_0 and T^* which we document in the table below:

Sample	T_0 [°C]	T_0 sigma	T* [°C]	T* sigma
D5ss	17.9	4.3	43.3	12.6
D10ss	18.7	2.7	21.2	2.4
D22ss	7.5	2.0	13.3	2.6
D50ss	14.1	2.7	15.0	1.9
R5ss	8.1	4.0	15.7	6.3
R10ss	12.5	3.1	28.2	7.5
R22ss	23.3	3.7	43.7	5.2
D22ds	11.6	2.8	9.1	1.7
D50ds	11.8	2.4	13.0	1.9
R22ds	15.1	1.8	23.0	2.2

S4 Thermophoresis of single stranded RNA

Soret coefficients for single stranded RNA. Identical to the finding for ssDNA in Fig.1b, we encounter the same size transition for ssRNA. The transition between a linear increase of S_T for Debye lengths below the particle size is found which is flattening towards an upper bound for larger Debye lengths. The transition shifts to larger Debye lengths with increased radius of the molecules.

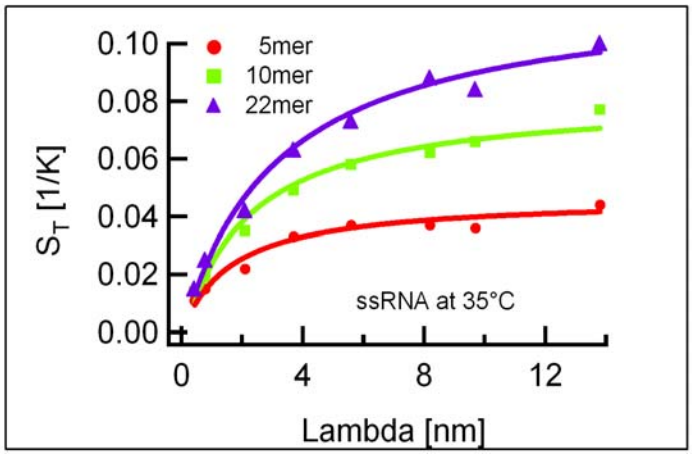

S5 Extrapolated Soret coefficient for uncharged particles for the limit of high temperatures

The non-ionic amplitude S_T^{∞} is plotted against the surface of the molecules, determined from the hydrodynamic radius R. Compared to Figure 3b, a similar linear relationship is found. With the data at hand, it is therefore not possible to distinguish between short ranged hydrophobic effects or other ion-independent contributions which scale with the spherical long ranged area of the molecule.

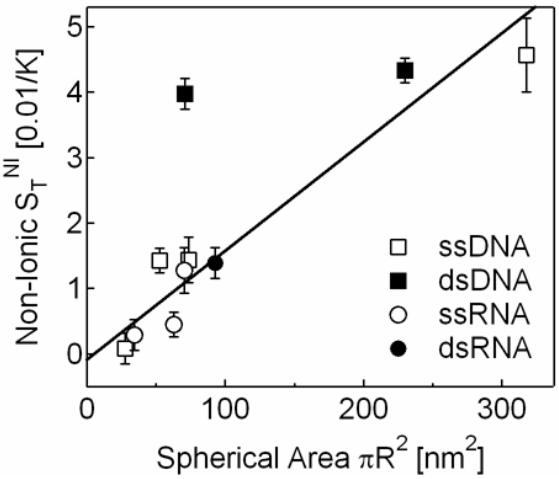

S6 Comparing S_T of single and double stranded oligonucleotides

The thermophoresis of single and double stranded DNA and RNA with a length of 22 bases is very similar at physiological salt concentrations (λ_{DH} =0.8nm). Single stranded molecules have a higher Soret coefficient than its double stranded version at lower salt concentration:

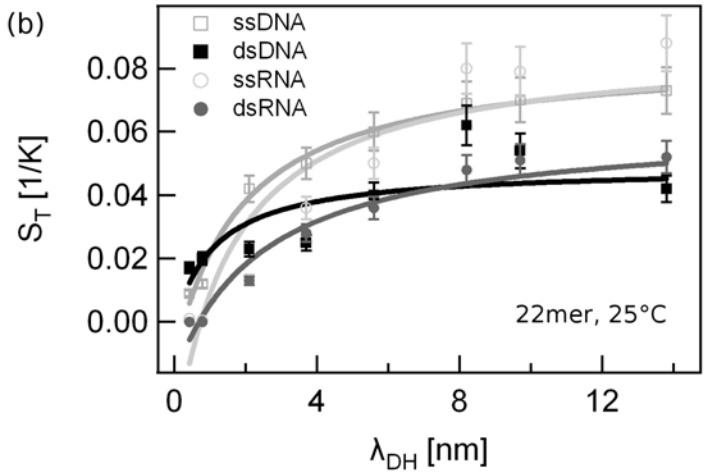

For double stranded samples we expect the separation of the two strands at high temperatures. Furthermore at lower salt concentrations and thus higher λ_{DH} the compromised charge shielding of the oligonucleotide backbones lowers the melting temperature. As a result, for temperatures higher than the shown 25°C oligonucleotides samples with complementary binding partners approach the single stranded values, an effect which was already used to determine DNA melting transitions with thermophoresis [47].

S7 pH dependence

Soret coefficient S_T measured for buffered and unbuffered solutions at various pH values. Between pH 4 and 11 the changed buffer pH changes the Soret coefficient less than 10%, well within the error margins of the measurement and not enough to consider the thermophoresis of OH^- ions to be a major contributor to an electrically driven thermophoresis. Measurements were performed at 25 °C without added KCl.

Soret Coefficient [1/K]	pH	Buffer
-0.0270	13	no buffer
-0.0070	12	no buffer
0.0530	11	no buffer
0.0530	10	no buffer
0.0661	4	no buffer
0.0470	3	no buffer
-0.0081	13	1mM TRIS
-0.0051	12	1mM TRIS
0.0810	11	1mM TRIS
0.0781	10	1mM TRIS
0.0811	7	1mM TRIS
0.0851	4	1mM TRIS
0.0431	3	1mM TRIS

S8 Sample Sequences

DNA
5-mer: 5'- Hex–TA GTT–3'
10-mer: 5' - Hex–TA GTT CTA AT–3'
22-mer: 5' - Hex–AT TGA GAT ACA CAT TAG AAC TA–3'
50-mer: 5' - Hex–ATAATCTGTAGTACTGCAGAAAACTTGTGGGTTACTGTTTACTATGGGGT–3'

RNA
5-mer: 5' - Hex–UA GUU–3'
10-mer: 5' - Hex–UA GUU CUA AU–3'
22-mer: 5' - Hex–AU UGA GAU ACA CAU UAG AAC UA–3'
50-mer: 5' – Hex–
AUAAUCUGUAGUACUGCAGAAAACUUGUGGGUUACUGUUUACUAUGGGGU–3'

Double stranded probes contained an equal amount of complementary sequence.